INVESTIGATION OF LASER INDUCED PLASMA IN VARIOUS CONFIGURATIONS

By

ALAMGIR MONDAL

PHYS06201304011

Institute for Plasma Research, Gandhinagar

A thesis submitted to the
Board of Studies in Physical Sciences

In partial fulfillment of the requirements
For the Degree of

DOCTOR OF PHILOSOPHY

of

HOMI BHABHA NATIONAL INSTITUTE

September, 2019

Homi Bhabha National Institute[1]

Recommendations of the Viva Voce Committee

As members of the Viva Voce Committee, we certify that we have read the dissertation prepared by **Mr. Alamgir Mondal** entitled **"Investigation of laser induced plasma in various configurations"** and recommend that it may be accepted as fulfilling the thesis requirement for the award of Degree of Doctor of Philosophy.

Chairman – Prof. Amita Das	Amita Das	Date:06/09/2019
Guide / Convener – Dr. Hem Chandra Joshi	H.C.J	Date:06/09/2019
Examiner - Prof. Atul Srivastava	Atul Srivastava	Date:06/09/2019
Member 1- Dr. Vinay Kumar		Date:06/09/2019
Member 2- Dr. Surya Kumar Pathak		Date:06/09/2019
Member 3- Dr. Ramasubramanian Narayanan	N Raman	Date:06/09/2019
Technology Advisor- Dr. Rajesh Kumar Singh		Date:06/09/2019

Final approval and acceptance of this thesis is contingent upon the candidate's submission of the final copies of the thesis to HBNI.

I hereby certify that I have read this thesis prepared under my direction and recommend that it may be accepted as fulfilling the thesis requirement.

Date: 06/09/2019

Place: IPR, Gandhinagar

H.C.J

Dr. Hem Chandra Joshi

(Guide)

[1] This page is to be included only for final submission after successful completion of viva voce.

STATEMENT BY AUTHOR

This dissertation has been submitted in partial fulfillment of requirements for an advanced degree at Homi Bhabha National Institute (HBNI) and is deposited in the Library to be made available to borrowers under rules of the HBNI.

Brief quotations from this dissertation are allowable without special permission, provided that accurate acknowledgement of source is made. Requests for permission for extended quotation from or reproduction of this manuscript in whole or in part may be granted by the Competent Authority of HBNI when in his or her judgement the proposed use of the material is in the interests of scholarship. In all other instances, however, permission must be obtained from the author.

ALAMGIR MONDAL

DECLARATION

I, hereby declare that the investigation presented in the thesis has been carried out by me. The work is original and the work has not been submitted earlier as a whole or in part for a degree/diploma at this or any other Institution or University.

ALAMGIR MONDAL

List of Publications arising from the thesis

List of Publications

Publications in Peer Reviewed Journals:

1. **Effect of ablation geometry on the dynamics, composition, and geometrical shape of thin film plasma**, Alamgir Mondal, R. K. Singh and Ajai Kumar, *Physics of Plasmas* (25), 013517 (2018), https://doi.org/10.1063/1.4991469

2. **Spectroscopic investigation of stagnation region in laterally colliding plasmas: Dependence of ablating target material and plasma plume separation**, Alamgir Mondal, Bhupesh Kumar, R. K. Singh, H. C. Joshi, and Ajai Kumar, *Physics of Plasmas* (26), 022102 (2019), https://doi.org/10.1063/1.5075629

3. **Neutral and ion composition of laser produced lithium plasma plume in front and back ablation of thin film**, Alamgir Mondal, R. K. Singh, H. C. Joshi, *Journal of Analytical Atomic Spectrometry* (34), 1822-1828 (2019), https://doi.org/10.1039/C9JA00158A

4. **Interaction of laser produced plasma in the presence of external magnetic field**, Alamgir Mondal, R. K. Singh, H. C. Joshi, (To be submitted for publication in refereed journal)

Conferences and Schools:

International Participation

1. Effect of ablation geometry on the formation of stagnation layer in laterally colliding plasmas. (Poster), Alamgir Mondal, R. K. Singh and Ajai Kumar, **"10^{th} Asia Plasma & Fusion Association Conference"**, Institute for Plasma Research, Gandhinagar, Gujarat, India, 2015.

2. Ablation geometry dependence on the dynamics of laser induced thin film plasma. (Poster), Alamgir Mondal, R. K. Singh and Ajai Kumar,

"26^{th} **International Toki Conference and 11^{th} Asia Plasma and Fusion Association**", National Institute for Fusion research, Gifu, Japan, 2017.

3. Characterization of laterally colliding plasma plumes formed by the multi-species target. (Poster), Alamgir Mondal, R. K. Singh and Ajai Kumar, "45^{th} **EPS Conference on Plasma Physics**", Prague, Czech Republic, 2018.

4. "**Joint ICTP-IAEA School on Atomic and Molecular Spectroscopy in Plasmas - 2019**", Trieste, Italy.

National Participation

1. Dynamics of shock wave and cavitation bubble produced by laser ablation of Cu in water. (Poster), Alamgir Mondal, R. K. Singh and Ajai Kumar, "29^{th} National Symposium on Plasma Science and Technology", Mahatma Gandhi University, Kerala, India, 2014.

2. Characterization of plasma plume produced by thin film laser ablation. (Poster), Alamgir Mondal, R. K. Singh and Ajai Kumar, "30^{th} National Symposium on Plasma Science and Technology", Saha Institute of Nuclear Physics, West Bengal, India, 2015.

3. Effect of ablation geometry on laser induced plasma of thin film. (Poster), Alamgir Mondal, R. K. Singh and Ajai Kumar, "32^{nd} National Symposium on Plasma Science and Technology ", Institute for Plasma Research, Gandhinagar, Gujarat, India, 2017.

4. A comparative study of front and back ablation of thin film. (Poster), Alamgir Mondal, R. K. Singh and Ajai Kumar, "National Conference on Plasma and Non-linear Dynamics ", JIS University, Kolkata, West Bengal, India, 2017.

ALAMGIR MONDAL

DEDICATIONS

This thesis is dedicated to my parents

ACKNOWLEDGEMENTS

First and foremost, I would like to express my sincere gratitude to my thesis supervisor Dr. Hem Chandra Joshi for his constant guidance, teaching and support during the course of my thesis work. I am thankful to him for his patience and timely advice throughout the tenure of my research work. Whenever, I needed his guidance he has been available with the much needed warmth and support.

I will always be grateful to Dr. Rajesh Kumar Singh for his guidance, since the time I had joined the group. Without his help, it was not possible for me to complete this journey. I am also thankful to Prof. Ajai Kumar for his guidance during the initial years of my Ph.D.

I am obliged to Prof. Amita Das (Chairperson), Dr. Vinay Kumar, Dr. Surya Kumar Pathak and Dr. Ramasubramanian Narayanan for consenting to be my doctoral committee members and valuable scientific inputs they have given over all these years. I always feel privileged to have them in my doctoral committee.

I am thankful to all the members of our research group; Narayan Da, Kaushik Da, Arvind Da, Siva Sir, Jinto Sir, Vishnu Sir, Kiran Sir, Neha, Pabitra Mishra who have always been there to help.

I specially thank to all academic committee members; Prof. S. Mukherjee, Prof. Sudip Sengupta, Prof. R. Ganesh, Dr. Joydeep Ghosh, Dr. D. Sharma, Dr. V. P. Anitha, Dr. Mani Subramanian, Dr. G. Ravi, Dr. M. Kundu, Dr. M. Bandyopadhyay for teaching me during 1^{st} year course work, and Prof. P. K. Kaw, Prof. A. Sen, Prof. S. K. Mattoo and Prof. Y. C. Saxena for their special classes. I am also thankful to all the members from workshop, IPR library, IPR administration for their help and support.

I would like to thank my batch mates; **Prabhakar, Atul, Sagar, Sandeep, Chetan, Jervis, Pallavi, Hershita, Meenakshee and Deepak** for their friendship and making my stay at IPR a memorable journey. I will always remember the joyful moments spent with them during all these years. I extend my sincere thanks to all **my seniors** (Ujjwal, Kshitish, D Sangwan, Sayak, Soumen, Manjit, Sanat, Sushil, Aditya, Ashwin, V Dharodi, Veda Bhai, Vara, Roopendra, Chandrashekar, Bhibhu, Neeraj, Mangilal, Deepa, Akanksha, Vidhi, Harish, Meghraj, Sameer, Arghya, Surbahi, Bhumika, Narayan, Ratan, Modhu, Amit, Debraj, Umesh, Sonu) **and juniors** (Shivam, Avnish, Rupak, Arun, Subrata Jana, Srimanta, Garima, Priti, Mayank, Piyush, Vivek, Sanjeev, Satadal, Soumen, Devshree, Ayushi, Satya, Prince, Jagannath, Sumon, Shishir and all others) who have helped me in many ways. Everyday's *"Chai Pe Charcha"* at hostel mess with them was always fun and refreshing for me.

Finally, I would like to convey my heart-felt gratitude and respect to my parents for their unconditional support and allowing me to follow my heart. Specially, I would like to thank my beloved wife, Sultana for her love and support in every aspect of my life. Also the most precious and beautiful smile of my little son (Jehan) has been a continuous source of inspiration for me. I would extend my thanks to my sisters (Angura and Nasima) for their compassion and support. This work would not have been possible, without my family member's constant support and encouragement.

ALAMGIR MONDAL

Contents

SYNOPSIS

In general, a target irradiated by a high power focused laser heats and ablates the target materials from the incident area followed by expanding plasma plume, commonly known as Laser Produced Plasma (LPP) or Laser Induced Plasma (LIP). [1] The study of laser produced plasma has been a key area of interest for the scientific community due to its manifold fundamental aspects as well as applications in various fields. Laser produced plasma has been studied extensively in the past and the study goes on continued with the advancement of new cutting edge technologies with development in lasers having higher energy and shorter pulse widths. [2] Extensive theoretical and experimental study on laser plasma has been done using lasers of different characteristics (i.e. nano-second, pico-second and femto-second) depending on the area of interest and applications. Effect of experimental parameters, e.g. ambient environment, magnetic field, electric field etc. on laser produced plasma has also been widely explored. [3–5] Study of transient plasma plume has many important applications in various disciplines such as laser processing of solid materials, laser induced breakdown spectroscopy (LIBS), fabrications of semiconductors, material sciences, thin film deposition, fast particle generations and plasma diagnostics. [6–10] Further, Ablation geometries such as front ablation, back ablation, ablation of structured target and ablation with angular laser beam play an important role in the dynamics and characteristics of such plasmas in terms of ion/neutral density, electron temperature, electron density etc. [11, 12] Ablation geomerties i.e. front ablation (FA) and back ablation (BA) also exhibit many interesting differences in shape, size, elctron temperature/density and atomic processes of plasma plume. In case of front ablation (FA) plasma is produced in a conventional laser ablation method whereas in back ablation (BA) laser beam interact with thin film suported on the thick transperent substrate and induced plasma plume popogates along the direction of laser beam. [13] The differences in the properties of plasma plume in two ablation geometries arise due to the differences in the ablation mechanism in these two cases. These studies are useful in controling the plasma parameters and their dynamical and structural behaviour in context of various applications like thin film depostion/removal, generation of energetic particles, study of opacity and reflectance, diagnostics etc. [10, 11, 14, 15]

When two plasma plumes are produced in a close proximity and expand in same direction, they produce an interaction region, also known as stagnation region in between the two primary plasma plumes. [16–19] The interaction region has different characteristics from the primary (or seed) plasma in terms of expansion velocity, electron temperature/density and constituent composition. Intearaction region is formed because of the transportation of energetic particles from the seed into interaction region. It has been observed that the interaction region expands with higher expansion velocity compared to seed plume and has higher ionic density in certain conditions. Collisionality parameter (ξ = D/λ_{ii}) defines the nature of interaction region where D is the seperation between two plasma and λ_{ii} stands for ion-ion mean free path. [20] The value of ξ defines whether the interaction zone is produced because of interpenetration of two plasmas (i.e. $\xi < 1$) or because of collisional stagnation (i.e. $\xi > 1$). [20] Also the value of ξ defines whether the formation of interaction region happens through soft or hard stagnation.

Further, study of laser produced plasma expanding in an external magnetic field has immense importance in physics and from appliactions point of view. In case of laser produced plasma, important phenomenon like magnetic confinement, diamagnetic cavitation, stiration etc have been widely reported in presence of static as well as varying magnetic field. [21–23] Though very little work has been done related to lateral interaction of plasma plumes in an external magnetic field.

In this thesis work, we have performed several experiments to study laser produced plasma in different ablation geometries that is front and back ablation. Various atomic processes and composition analysis of the expanding plasma has also been done by spectral analysis using Atomic Data and Analysis Structure (ADAS). [24] Further, Experimental investigations have been performed to understand the effect of various atomic masses of the target sample on the characteristics of colliding plasma and induced interaction regions. To further enhance our understanding on this subject we have also studied the properties of heterogeneous colliding plasma plumes and the subsequent formation of interaction zones. In context of manipulation of plasma parameters, the present investigations are further extended to study of colliding plasmas in presence of an external magnetic field (0 - 6000 Gauss). The above set of experiments produce many interesting phenomenon which, we believe, are important in physics point of view and can be useful in many applications also. We expect these results will contribute significantly to enhance the understanding of laser produced plasmas in different scenarios and its applicability in different practical applications.

In this thesis, the work arranged in the chapters listed below,

Chapter 1:

In this chapter, a brief summary of previous work done in the field of laser induced plasma has been described. It also presents a concise introduction, an overview of basic understanding and mechanism of Laser Produced Plasma (LPP), applications and properties of it in different conditions etc.

Chapter 2:

The experiments are performed in ambient pressure ranging from 2×10^{-6} mbar to 1 mbar in a stainless steel chamber with multiple ports having access for diagnostics (imaging, spectroscopy), incoming laser beam, target holder and vacuum systems etc. In this chapter, we have described the design and setting of the experimental set-up in detail.

Chapter 3:

In this chapter, we have described the effect of ablation geometry on the dynamics, composition and geometrical shape of LiF-C thin film. It is shown that ablation geometry plays a very important role in the dynamics and characteristics of laser produced plasma plume. To demonstrate this we have produced plasma by using Nd:YAG laser focused onto a LiF-C thin film in two different geometry i.e. Front Ablation (FA) and Back Ablation (BA). The film is deposited on a transparent quartz substrate. Ablation geometry dependence on plume dynamics, geometrical aspect and composition of the expanding plasma plume is discussed in this study. Fast imaging and spectroscopic techniques have been used as diagnostics tools in this study. The results show that plasma plume dynamics also depends on ambient environment, laser energy and spot size. The study clearly demonstrates that energetic and spherical plasma produced in front ablation is significantly different in comparison to the relatively slow and cylindrical plasma plume observed in case of back ablation. The effect of ambient environment, laser energy and spot size on the dynamics of plasma plume formed by front and back ablations is also highlighted. This study can be useful to control plasma parameters in different applications e.g. generation of energetic particles, surface analysis, laser induced breakdown spectroscopy etc. This work has been published in Physics of Plasmas

25, 013517 (2018), AIP (https://doi.org/10.1063/1.4991469).

Chapter 4:

A description on compositional analysis (ions/neutral ratios) of laser produced plasma plume in front and back ablation geometries is given in this chapter. The impact of ablation geometry on the composition of plasma plume produced by laser ablation is emphasized in this study. The neutral and ionic contributions in Front Ablation (FA) and Back Ablation (BA) of LiF-C thin film in vacuum (2×10^{-6} mbar) as well as 2×10^{-1} mbar ambient argon has been done. To estimate neutral abundance we have taken two approaches in consideration that is Atomic Data and Analysis Structure (ADAS) as well as integrated line intensity ratio of Li I 670.8 nm and Li I 610.3 nm lines under local thermal equilibrium (LTE) conditions. This study clearly demonstrates the higher contribution of neutral particles in BA plume compared to FA in vacuum. It also shows that in case of higher pressure (i.e. 2×10^{-1} mbar) at initial times neutrals are lower in FA plume compared to BA geometry and this ratio increases with time and after 700 ns it is higher than one. The present attempt will be interesting from the view point of understanding the evolution of plasma composition in various geometries/configurations of laser ablation which has important implications in various applications e.g. neutral beam generation, thin film deposition etc. These results have been submitted for internal review and will be submitted in peer reviewed journal after internal assessment.

Chapter 5:

In this chapter, investigation of stagnation region in laterally colliding plasmas and their dependence on the properties of the ablating target material and plasma plumes separation has been described. Based on fast imaging and spectroscopy, we have demonstrated that atomic mass of the target can play a role in the formation, expansion and characteristics of the interaction region in laterally colliding plasmas. The mass of the ablated species affects the characteristics of interaction region in terms of their initiation time, expansion velocity, shape, size, strength and spectral feature of stagnation region. In this study carbon, aluminium and nickel have been chosen as targets having different atomic masses. The effect of spatial separation of two interacting plume is also briefly discussed in this chapter.

It has been observed that interaction region is more intense, confined, sharp and highly directional in case of relatively higher atomic mass target (i.e. nickel) in comparison to the lighter one. Further, for smaller spatial separation, the axial velocities in the stagnation region are higher than in the velocity of seed plume, while for largest considered separation it is lower than that. The difference in plasma parameters in both the seed and interaction regions have been explained from the spectral analysis of aluminium line emission Al II 466.3 nm, which shows an increase in ionic emission in case of interaction region compared to seed. This study reveals that the enhancement in three-body recombination should be responsible for the increase in ionic emission (Al^{2+}) in the interaction region.
A revised version of the manuscript based on this study is to be submitted to Physics of Plasmas.

Chapter 6:

Dynamics and characteristics of plasma plume expanding in a varying external magnetic field are discussed in this chapter. Effect of external magnetic field on the seed plume and their interaction has been investigated. Time resolved fast imaging of the plasma shows some interesting features of single as well as colliding plasma plume. Spectroscopic data also reveal the effect of external magnetic field on ionic and neutral lines.

Chapter 7:

In this chapter, summary of the thesis work done during Ph.D. tenure is given and have briefly pointed out the importance and applications of this work. An overview of future research scope and the problems which can be attempted in continuation of this work are also projected here.

List of Figures

âŤIJ

1
Introduction

This thesis presents experimental investigations of laser produced plasma considering various aspects such as ablation geometry, ambient pressure, colliding plasma, external magnetic field etc. This chapter introduces different types of laser produced plasma followed by detailed literature survey of earlier works done by the research community. A short description on the motivation and objective of this thesis work has also been presented. The study of dynamical behaviour and characteristic parameters of **laser produced plasma in varying conditions** as mentioned above are discussed in this chapter.

1.1 Laser Produced Plasma (LPP)

After the discovery of laser in 1960, it attracted a great deal of interest for the scientific community in the past decades in the field of laser produced plasma. With further advancement of technology and sophisticated lasers with higher energy and shorter pulses many applications of laser produced plasma emerged. These lasers with cutting edge technology are capable to facilitate study of many fundamental physics problems in laboratory as well as have several applications. Several studies have been done on laser produced plasma in experiment, theory and simulation. Lasers can have very high energy in nano, femto and atto-second time duration and travel with negligible divergence. Such type of laser properties are helpful for many studies having important applications. In this case laser beam, focused on a target, can deliver very high energy which is sufficient to raise the temperature at the irradiated area well above its critical temperature. [1] This phenomenon is

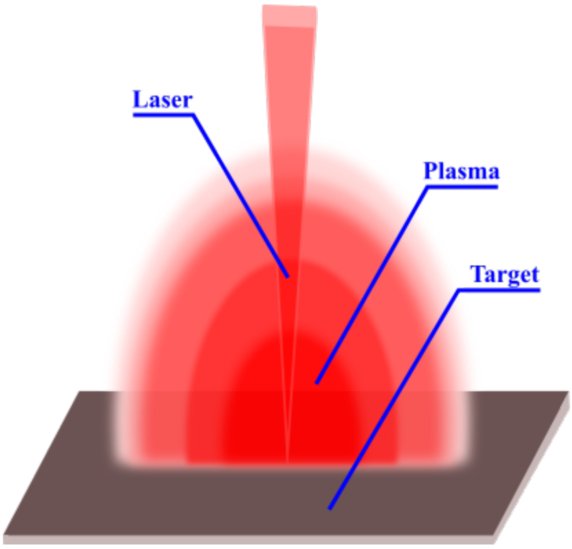

Figure 1.1: Schematic diagram of expanding laser produced plasma plume.

followed by evaporation of the material and produces an expanding plasma plume which is called Laser Produced Plasma (LPP). Plasma produced by laser ablation expands with plume like shape and hence, it is also called laser produced plasma plume.

A schematic diagram of an expanding plasma plume produced by laser ablation is shown in Fig. 1.1. The plasma plume produced in this method is transient in nature and has lifetime of a few micro-seconds. The plasma properties depend on several parameters such as laser energy, spot size, wavelength, pulse duration, ambient environment etc. All types of target materials like solid, liquid and gas can be used for producing plasma in this method. Study of LPP has many important applications in various disciplines such as laser processing of solid materials, laser induced breakdown spectroscopy (LIBS), fabrications of semiconductors, material sciences, thin film deposition, fast particle generations and plasma diagnostics, inertial confinement fusion (ICF), X-ray lasers, extreme ultra-violet (EUV) lithography, and has been widely explored under different conditions by several authors. [3–10] Study of plasma-plasma interaction, also called as colliding plasma, under different conditions is also possible by this method.

1.1.1 Ablation process

Starting from the laser incident on the target surface to the expansion, laser produced plasma can be divided in three steps: **(i) interaction of laser with the bulk target, (ii) interaction of the laser with the evaporated material and (iii) expansion of the produced plasma in the background.**

At the first stage, focused laser is incident on the target surface and a fraction of it is reflected back and rest is absorbed by the target. The percentage of reflection and absorption depends on the properties of the target and incident laser beam. Due to the absorption of laser radiation, surface temperature of the target increases very rapidly. The temperature increases so high that it reaches its critical value of the target in less than hundred picoseconds. This leads to phase transformation and vaporizes the material at the irradiated area. In the second stage, vaporized target material is ejected from the target and forms a thin layer of ionized gas cloud. All these phenomena occur within a few hundred picoseconds. When the duration of laser pulse is in nano-second ragime, the evaporated gas cloud continues to absorb laser energy till the termination of laser pulse. [1] At this stage laser energy gets absorbed through inverse Bremsstrahlung process by free electrons present inside the gas cloud. This gas cloud is called plasma as it gets ionized via collision between stray electrons and neutrals in vapour. The absorption coefficient (α_p) is expressed by eqn. 1.1. [25]

$$\alpha_p = 3.69 \times 10^8 \left(\frac{Z^3 n_i^2}{T^{0.5} \nu^3} \right) [1 - exp\,(-h\nu/kT)] \tag{1.1}$$

In this equation Z, n_i, T, ν, h and k are the average charge, ion density, plasma temperature, laser frequency, Planck and Boltzmann constants, respectively. The equation shows that α is proportional to n_i^2. Therefore, laser is absorbed only very close to the target surface where density is high. This equation is valid only for the assumption that plasma frequency is less than the frequency of the incident laser. Otherwise, laser will be reflected back from the plasma at critical density i.e. if plasma frequency is greater than laser frequency. After the termination of the laser pulse, the plasma plume expands in the background ambient (vacuum, background gas, pressures, magnetic field etc.) in third step.

Laser produced plasma is highly sensitive to background gas and pressure, ambient magnetic field which will be discussed in the following sections.

1.1.2 Plasma in vacuum

In vacuum, expansion of laser-produced plasma is free and adiabatic. This adiabatic expansion process can be described by Euler's hydrodynamic equations which are described by, [26, 27]

$$\frac{\partial \rho}{\partial t} = -\frac{\partial(\rho v)}{\partial x} \tag{1.2}$$

$$\frac{\partial(\rho v)}{\partial t} = -\frac{\partial}{\partial x}[p + \rho v^2] \tag{1.3}$$

$$\frac{\partial}{\partial t}[\rho(E_d + \frac{v^2}{2})] = -\frac{\partial}{\partial x}[\rho v(E_d + \frac{P}{\rho} + \frac{v^2}{2})] + \alpha_{IB} I_{laser} + \epsilon_{rad} \tag{1.4}$$

Here, ρ is the mass density, v is the flow velocity, p is the local pressure, E_d is the internal energy density, I_{laser} is the laser irradiance, α_{IB} stands for the absorption coefficient due to inverse Bremsstrahlung and ϵ_{rad} is the amount of energy emitted by the vapour per unit volume and time in the Bremsstrahlung process. The velocity of the plasma plume can be expressed by, [28]

$$v = \sqrt{\frac{(4\gamma + 10)E}{3M}} \tag{1.5}$$

In this equation, E, M and γ represent energy of plume, mass of evaporated material and ratio of specific heats respectively. This equation suggests a linear expansion of plasma in the vacuum. Though it is not possible to achieve ideal vacuum conditions practically. In experimental studies ambient pressures $\leq 10^{-6}$ mbar can be considered as vacuum. Our calculations are based on this assumption in the subsequent chapters of this thesis. At very low pressure the particle density of the ambient is low and mean free path is high. Therefore, interaction between plasma and ambient gas particles is negligible.

1.1.3 Effect of ambient (pressure and gas)

Presence of any ambient gas or high pressure affects adiabatic and free expansion dynamics and plasma parameters which we have discussed for vacuum conditions. With the introduction of ambient gas or increased pressure, plasma plume experiences a resistive force or drag force against its expansion. This slows down the plasma plume and plasma parameters also get changed. Generally, expansion of plasma plume at high pressure follows two models depending on certain parameters. In the first scenario, when the mass of swept volume of ambient gas is higher as compared to laser ablated plasma, it follows **shock-wave model** described by eqn. 1.6. [29]

$$z = \left(\frac{E_0}{\rho_b}\right)^{0.2} t^n \tag{1.6}$$

Where, E_0 is proportional to the laser energy density and ρ_b is the density of the background gas.

In the other case, plasma plume follows **drag force model** given in eqn. 1.7. [30]

$$z = z_f[1 - exp(-\beta t)] \tag{1.7}$$

Here, β is the slowing coefficient and z_f is the stopping distance of the plasma plume. Stopping distance is maximum path travelled by the plasma plume.

From equations 1.6 and 1.7 we can understand the effect of the mass of the ambient gas. By changing ambient gas from lower to higher atomic mass, the plasma expansion can change from drag to shock like behaviour. In the presence of comparatively lower ambient gas pressure, plasma plume gets split into two components (fast and slow). Higher energetic plasma species which travel without colliding with ambient gas particles form the fast component. On the other hand, a fraction of plasma particles come across colliding with ambient and loose a fraction of their kinetic energy. These species move slowly as compared to fast component and form slower component which will be discussed in chapter 3.

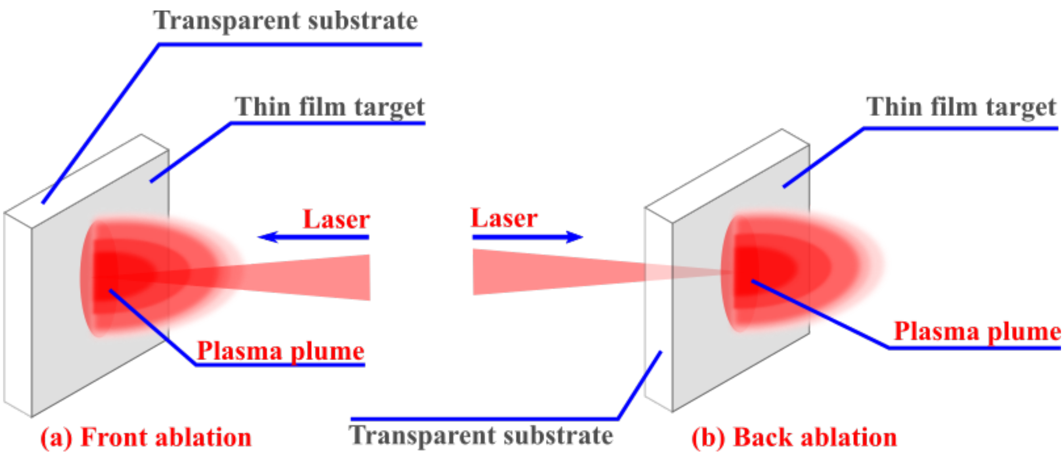

Figure 1.2: Schematic diagram of laser produced plasma of thin film deposited on a transparent substrate in (a) Front Ablation (FA) and (b) Back Ablation (BA) geometries.

1.1.4 Dependence on ablation geometry

Ablation geometries i.e. target orientation towards the incident laser, plays crucial role in determining the expansion dynamics, shape, size and plasma parameters. Ablation geometry can be of different types, for example, ablation by laser incident at an angle, structured target etc. Depending on ablation of the thin film target, it can also be classified in two categories i.e. Front Ablation (FA) and Back Ablation (BA). In front ablation of thin film, plasma is produced in a conventional procedure and it can be seen in Fig. 1.2. This figure shows a schematic diagram of laser produced plasma plumes produced for two different types of ablation geometries. The main difference as shown in this figure comes from the special type of target material which is a thin film of the desired material deposited on a transparent substrate. Mostly, quartz plate is used for depositing thin film at one side and opposite side is kept unaltered. We can see in FA case of Fig. 1.2 that plasma plume expands in opposite direction of the incident laser beam, which is similar to the ablation of solid target. However, the underlying physics and plasma properties are very different from plasma produced by solid target ablation. [11, 12]

In another case i.e. in back ablation (BA) of Fig. 1.2, laser is incident at the film-substrate interface from the back side of the target and produces plasma plume. In back ablation case, incident laser heats the illuminated area and starts melting at the film-substrate interface, which propagates across film thickness. In the mean time, before melting of the total film thickness vapour pressure build up becomes large enough to propel the material in the form of an expanding plasma plume. As the vapour pressure builds inside, it blows-off the irradiated portion of the film and is termed as laser blow-off plasma (LBO). [13] LBO or BA has many applications in thin film depostion/removal, generation of energetic particles, study of opacity and reflectance, diagnostics etc. [10, 11, 14, 15]

1.1.5 Plasma in external magnetic field

We have discussed that plasma expansion dynamics and plasma parameters get affected by changing ambient. Plasma in the presence of external magnetic field is important from the view point of its applications and interesting physics. Plasma parameters can be controlled by the optimization of parameters of laser, pressure and external magnetic field. In case of laser produced plasma, important phenomena like magnetic confinement, diamagnetic cavitation, stiration etc. are observed in the presence of static as well as varying magnetic field. [21–23] Parameters which decide this are Larmor radius, plasma beta (β), bubble radius (R_b) and magnetic field diffusion time (t_d). These parameters are briefly described in the following sections.

1.1.5.1 Larmor radius or gyro radius

Larmor radius is defined as the radius of circular path followed by a charged particle's motion in a magnetic field. This is expressed by the relation given in eqn. 1.8. [31]

$$r = \frac{mV_\perp}{|q|B} \tag{1.8}$$

Where m, $V_\perp$, q and B represent mass of the gyrating particle, velocity of the charged particle perpendicular to magnetic field, charge of the particle and applied magnetic field, respectively.

Plasma dynamics in presence of an external magnetic field depends on the Larmor radius or gyro radius. Where the Larmor radii of both electron and ions are larger than plasma dimension, it is called unmagnetized plasma. Generally, Larmor radius of electron is much smaller and that of ion is larger than plume dimension in case of laser produced plasma. Therefore, ions are considered free and electrons are considered magnetized in such studies.

1.1.5.2 Plasma beta (β)

Plasma beta (β) is basically ratio of plasma pressure to magnetic pressure and depending on the parameters it can be classified into three types in case of laser produced plasma in a magnetic ambient. First one is thermal beta defined in eqn. 1.9. [31,32]

$$\beta_{th} = \frac{n_e T_e}{B^2/2\mu_o} \tag{1.9}$$

Where, n_e, T_e, B and μ_o stand electron density, electron temperature (eV), applied magnetic field and permeability of free space.

After the production of plasma plume, thermal energy gets converted into directed energy and it plays important role. The effect of directed energy is measured by directed beta (β_d) i.e. ratio of kinetic pressure of plasma to magnetic pressure, which is expressed by eqn. 1.10.

$$\beta_d = \frac{Plasma \quad kinetic \quad pressure}{Magnetic \quad pressure} = \frac{m n_e v^2/2}{B^2/2\mu_o} \tag{1.10}$$

Here, m is the mass of plasma species and v is mass flow velocity. Total beta (β_{tot}) is expressed as the sum of these two beta expressed in above equations.

$$\beta_{tot} = \beta_{th} + \beta_d = \frac{n_e T_e + m n_e v^2/2}{B^2/2\mu_o} \tag{1.11}$$

1.1.5.3 Bubble radius

In the presence of magnetic field, diamagnetic cavity or bubble is formed by the laser produced plasma which acts in opposite direction to the external field B. The maximum radius of this magnetic bubble is called as bubble radius (R_b) and expressed by eqn. 1.12. [33,34]

$$R_b = \left(\frac{3\mu_o E_{lpp}}{\pi B^2}\right)^{1/3} \tag{1.12}$$

where, E_{lpp} is the kinetic energy of the plasma and it is generally considered as half of the laser energy deposited on the target. Other parameters bear their standard meaning.

1.1.5.4 Magnetic diffusion time

Initially, external magnetic field can't penetrate into laser produced plasma plume due to the induced field of magnetic bubble in opposite direction of external B. With expansion of the plasma plume, strength of magnetic bubble decreases and becomes equal to external B. At further delay it becomes smaller and the external field diffuses into plasma plume. The required time delay for external B to start diffusing into the plasma plume is called as diffusion time (t_d) and it is expressed by eqn. 1.13. [32]

$$t_d = \frac{4\pi\sigma R_b^2}{c^2} \tag{1.13}$$

Here, c is velocity of light and σ is plasma conductivity. Plasma conductivity is expressed by eqn. 1.14. [35]

$$\sigma = \frac{50\pi^{1/2}\epsilon_o^2(k_\beta T_e)^{3/2}}{m_e^{1/2}e^2 Z ln\Lambda} \tag{1.14}$$

where, T_e is electron temperature in kelvin and $ln\Lambda$ is Coulomb logarithm which can be taken around 10 for laser produced plasma.

1.1.6 Colliding plasma

When two plasma plumes are produced in close proximity with a spatial separation, they interact with each other and produce interaction zone in between them. The primary plasma plumes which interact are generally called as seed plasma, and the region of induced plasma is called interaction zone. This scenario is shown in the schematic diagram of two colliding plasma in Fig. 1.3. In this figure, we can see that two seed plasmas are produced by two focused laser beams at the same time. These two plasma plumes induce another one i.e. interaction zone in between them. [16,18,19] Study of interaction zone in a colliding plasma is of great interest because of its promising characteristics. Expansion velocity, electron temperature/density and constituent composition are strikingly different from single plume. Interaction

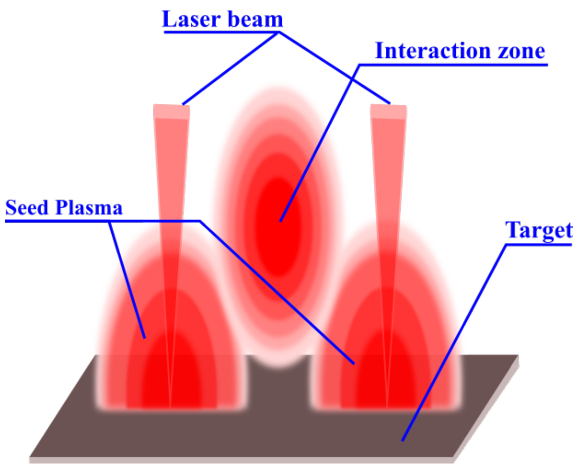

Figure 1.3: Schematic diagram of colliding plasma and interaction zone

region is formed by the transportation of energetic particles from the seed. In some conditions, interaction zone stagnates and therefore, it is also called as stagnation region. The interaction of two plasma plumes and formation of stagnation region depend on collisionality parameter which is defined by relation described below.

$$\xi = D/\lambda_{ii} \tag{1.15}$$

In this equation ζ represents the collisionality parameter, D denotes the separation between two plasma plumes, λ_{ii} is ion-ion mean free path which is defined by the relation, [20]

$$\lambda_{ii} = \frac{m_i^2 v_{12}^4}{4\pi e^4 Z^4 n_i ln\Lambda_{12}} \tag{1.16}$$

Here, m_i is ion mass, v_{12} is relative velocity of two seed plume towards each other, e is electronic charge, n_i is ion density, Z is ionization level and $ln\Lambda$ is Coulomb logarithm for the plasma plumes. In standard definition value of ζ less than 1 stands for interpenetration of the two plasma plumes into each other. In that case, ion-ion mean free path is less than separation between two seen plasmas and they from interaction zone by penetrating into each other. In the opposite case of $\zeta > 1$ signifies collisional stagnation of the interaction zone. Properties of colliding plasma and interaction zone depend on laser parameters, geometry and ambient conditions.

Generally, it is found that the expansion velocity of interaction zone is higher as compared to the seed plume and it is useful for producing both charged and neutral particles.

1.2 Review of earlier works relevant to thesis

In the past decades, studies on different type of laser produced plasma have been done by several authors and reported in a large number of published articles. Studies are done with different laser parameters i.e. nano, femto-second pulse duration, wavelengths and energy range. [1,3,4,36,37] Laser produced plasma has been studied for different type applications and basic plasma studies. From the application point of view, it is important for material science, chemical physics, pulsed laser deposition of thin film, reflectance study, LIBS etc. [38,39,39–41]

Few of the important works done on laser produced plasma in recent times are mentioned in the following lines. Wood et. al. reported plasma plume propagation and splitting during pulsed laser deposition at low pressure in their pioneering work given in Ref. [36]. Amoruso et. al. reported characterization of laser produced plasma under different conditions like ambient pressure and differernt targets out of which few are mentioned in Ref. [1,42,43]. Geohegan et. al. reported the dynamics of plasma plume in the presence of an ambient gas pressure [44] and they have contributed many other studies also as mentioned in Ref. [3,45,46]. A great deal of work is done by many authors on the effect of different ambient gas and pressure on the dynamics and characteristics of laser produced plasma. [7,25,47–49]. Harilal et. al. reported internal structure, plasma dynamics, plume splitting and sharpening in the presence of ambient gas, and an evaluation of equilibrium conditions and temperature-dependent speciation in a laser-produced air plasma. [48–50]

Laser produced plasma has important applications in both thin deposition and ablation of thin film under different scenario. Pulsed Laser Deposition or in short PLD technique for thin film growth was first reported by Smith et. al. in Ref. [41]. Later Singh et. al. reported theoretical model for deposition of thin films using pulsed laser evaporation technique. [7, 25]. Lowndes et. al. reported the role of energetic species in the formation of ultrahard phases and in the doping of semiconductors by using pulsed laser deposition. [46] Wang et. al. studied thin film deposition of laser ablated rare earth Ni_2B_2C plasma plumes by optical spectroscopy. [39] George et. al. studied laser produced LiF-C thin film under different ambient pressures and reported ellipsoidal shape of the plasma plume in vacuum. [51] They also reported enhancement in plume intensity, and change in shape, size and confinement due to introduction of different types of ambient gas and pressures. [52, 53]

Laser produced plasma of a thin film in back ablation (BA) shows promising characteristics which has application in material science, microfabrication, enenrgetic particle beam generation, tokamak edge plasma diagnostics etc. [10, 11, 54] Back ablation of thin film which is also called as forward transfer mechanism is reported by Bohandy et. al. [12, 55] Kumar et. al. reported experimental studies of colliding plasma produced by LiF-C thin film. [56–58] The study shows that interaction zone of thin film produced plasma plume has more neutrals as compared to solid target ablation case.

Laser produced plasma facilitates the study of plasma-plasma interaction or colliding plasma with different conditions, such as angle, head-on collision etc. The interaction zone produced in a colliding plasma is of particular interest in this study. Several works have been done on colliding plasma and a few of them are cited here. Rumsby et al. in their pioneering work reported colliding plasma using two collinear laser beams for various spatial separations in the high intensity range. [59] Generation of plasma species of high kinetic energy and short excited state lifetime in colliding plasmas has been reported by Camps et. al. [6] An electrostatic study of dual colliding versus single plasma plume using a Faraday cup and drift tube has been performed by P. Yeates et. al. [60] Dynamics of cross beam polarization for graphite target was studied by Sánchez Aké et. al. and found that collisional processes reduce the kinetic energy of the second plume. [61] Effects of space charge separation in a colliding plasma has been discussed by P. Hough et. al. [62] Li et. al. reported the stagnation layer of colliding plasma plumes for different target materials and attributed small value of collisionality parameter of high Z material to ion mass. [63] Al Shobul et al. investigated colliding laser produced plasma (using orthogonal beams) for some low Z as well as high Z materials and found that high Z plasma inter penetrate where as low Z plasma stagnate. [17] Target geometry as well as composition have been found to affect the stagnation region considerably. [64] Pulsed laser cross beam laser induced plasma was studied in case of two graphite targets and was found that collisional effects are responsible for the observed behaviour. [65] The formation and expansion of interaction zone in colliding plasmas is highly dependent on the geometrical shape and divergence of the interacting plumes and energy of the ablating laser.

Laser produced plasma, whether single or colliding, in presence of an external magnetic field shows very promising features in terms of fundamental and application prospects. Tuckfield et. al observed plasma bounce in presence of external magneitc field of 1200 Gauss. [66] Ripin et. al. observed linear and nonlinear features of a strong plasma and magnetic field interchange which is attributed to Rayleigh-Taylor instability in the limit of large ion Larmor radius. [67] Mostovych et. al observed collimation and instability of laser produced plasma jets in strong transverse magnetic fields. [68] Peyser et. al. reported electron-ion velocity shear driven hybrid instability in laser produced plasma expansions in Ref. [69]. Neogi et. al. studied laser produced carbon plasma expanding in vacuum, low pressure ambient gas and nonuniform magnetic field. [70, 71] Rai et. al. reported laser produced plasma from solid and liquid targets and observed 1.5 - 2 fold increse in line emission. [72] Harilal et. al. reported changes in plume structure and dynamics, enhanced emission and ionization, Joule heating and adiabatic compression in the presence of the magnetic field in Ref. [32]. In another work they showed ion debris mitigation from tin plasma using ambient gas and magnetic field separately in a combined work in Ref. [73]. Joshi et. al. observed an initial increase in ion/neutral emission of lithium plasma in presence of a varying magnetic field. [74] Kumar et. al. reported the effect of transverse magnetic field on the dynamics of plasma plume and spectral emission of laser-blow-off plasma of a thin film in the presence of ambient gas. [75–78] Behera et. al. reported in Ref. [21] slab like structures, moving with different velocities, which are observed in presence of both the magnetic field and ambient gas. In another work they have studied structure and dynamics of the plume in diamagnetic and non-diamagnetic limits by using two directional (X and Y) fast imaging of plasma plume in variable magnetic field. [5] Iftikhar et. al. observed the effect of transverse magnetic field on laser-induced breakdown spectroscopy (LIBS) and surface modifications of germanium at various fluences, argon pressure. [79] Singh et. al. dtudied the effect of varying magnetic field on laser-produced copper plasma and the deposited particles on the target surface. [80] Dawood et. al. also studied magnetic field effect on plasma parameters and surface modification of laser-irradiated copper-alloy and compared to field free case. [81]

A limited number of important studies, related to this thesis work, on laser-produced plasma in different domain are cited here. However, other studies can also be found reporting on different scenarios. The primary aim of this literature survey is to provide a brief review of previous studies done on laser-produced plasma in various conditions.

In this thesis work, we have investigated how the characteristic parameters of single as well as colliding plasma plumes can be controlled by external conditions. To perform this, we used thin film target and solid targets (C, Al, Ni) with different atomic masses. We studied the effect of ambient pressure, ablation geometries (FA and BA), colliding plasma and external magnetic field effect for this purpose. The results show that plasma characteristic parameters can be controlled effectively by changing these external conditions.

1.3 Layout of the thesis

This thesis presents systematic experimental investigation of laser produced plasma in varying conditions. This thesis is divided in total seven chapters in a sequential order as described below.

Chapter 1: In this chapter, a brief summary of previous work done in the field of laser induced plasma has been described. It also presents a concise introduction, an overview of basic understanding and mechanism of Laser Produced Plasma (LPP), applications and properties of it in different conditions etc.

Chapter 2: The experimental schemes, vacuum systems, laser systems and diagnostic tools which are used to perform all the experiments, are described in this thesis chapter and explained step by step. Schematic diagrams are also provided accordingly.

Chapter 3: In this chapter, the effect of front and back ablation geometries on the dynamics, composition and geometrical aspect of LiF-C thin film has been discussed.

Chapter 4: Composition analysis (ions/neutral ratios) of laser produced LiF-C thin film plasma in front and back ablation geometries in vacuum (i.e. 2×10^{-6}

mbar) and 2×10^{-1} mbar ambient are discussed in this chapter. Atomic Data and Analysis Structure (ADAS) as well as integrated line intensity ratio of Li I 670.8 nm and Li I 610.3 nm lines under local thermal equilibrium (LTE) conditions are used for this analysis.

Chapter 5: Investigation of stagnation region in laterally colliding plasmas and its dependence on the atomic mass of the ablated species, separation between seed plasmas in vacuum is presented in this chapter. Carbon, aluminium and nickel are chosen for this study.

Chapter 6: In this chapter, dynamical behaviour and characteristic parameters of laser produced plasma plume in the presence of varying external magnetic field are discussed. Comparison has been done between plasma produced in the presence as well as absence of magnetic field.

Chapter 7: In this chapter, summary of the work done during Ph.D. tenure is given and also has briefly pointed out the importance and applications of this work. An overview of future scope of the work and the problems which can be attempted in continuation of this work are also projected here.

2

Experimental Details and Methodology

In this chapter, detailed description of the experimental setup, equipments (e.g. experimental chamber, laser source, optical and vacuum systems etc.) and different diagnostics methods (fast imaging, emission spectroscopy etc.) used in these experiments is given. Experimental setup is designed for the study of laser produced plasma under varying conditions e.g. different ambient, laser energy and geometry (front and back ablation) and colliding plasma. In the present study, laser induced plasma plume in various condition has been performed with the help of different kind of equipments and diagnostics. Laser produced plasma plume has very short lifetime which requires very fast diagnostic techniques such as fast imaging and optical emission spectroscopy.

2.1 Components used in the experiment

The components used in these experimental studies of laser produced plasma in various conditions are (i) **vacuum chamber and evacuation systems**, (ii) **target holding system**, (iii) **laser systems**, (iv) **optics (i.e. mirror, wave-plate, bi-prism, focusing lens etc.)** and (v) **plasma diagnostic systems (ICCD camera and spectrograph)**. Each of these components are described in detail in the following sections.

2.1.1 Vacuum chamber and evacuation systems

A cylindrical chamber made of high grade non-magnetic stainless steel has been used to perform the experiments in low pressure. The system can be seen in figure 2.1. The dimension of the chamber is 45 cm in height, 25 cm inner diameter and 1 cm thickness. A base pressure of 2×10^{-7} mbar can be achieved in this chamber. It has total 10 ports which makes the operating area of the system accessible for the target holding system, incoming laser, vacuum pumps, ICCD camera and optical emission spectroscopy. Six out of total 10 ports are fitted with CF 100 flanges and remaining four are fitted with CF 25 flanges. These windows give access inside the chamber from all three i.e. X, Y and Z directions. The ports used for incoming laser, imaging and spectroscopy are closed with flanges fitted with 99.99 % transparent quartz glass. A rotary pump (Pfeiffer Vacuum, DUO 10M), a Turbo Molecular Pump (TMP) (Pfeiffer Vacuum, TC600) and a booster pump (Pfeiffer Vacuum, OnTool Booster 150, DN50 ISO-KF) have been used for evacuating the system to a base pressure 2×10^{-7} mbar. The maximum pumping speed of the rotary pump is 12 m^3/hour, booster pump is 130 m^3/hour and TMP has 230 litre/hour.

For performing the experiments at different argon pressures (i.e. 1 mbar, 2×10^{-1} mbar, 2×10^{-2} mbar etc.) gas has been introduced through a manually controlled fine needle valve from an external gas cylinder. A combination of Pirani (range 1 to $\sim 10^{-3}$ mabr) and Penning gauges (range $\sim 10^{-2}$ to $\sim 10^{-9}$ mbar) (Pfeiffer Vacuum, compact full range) has been used.

2.1.2 Target and holding system

Target and its holding system play very crucial role in the experiments discussed in this thesis. Two type of targets i.e. thin film and solid plates have been used in this study. Lithium Fluoride Carbon (LiF-C) thin film with dimension 60×60 mm^2 has been used to study the plasma in two different geometries i.e. front ablation and back ablation (discussed in chapter 1 and 3). Solid target plates with dimension 60×20 mm^2 of carbon, aluminium and nickel have been used to study atomic dependency on colliding plasma and interaction region. Special measures, in terms of purity ($\sim$99.9%) and surface flatness have been taken into consideration

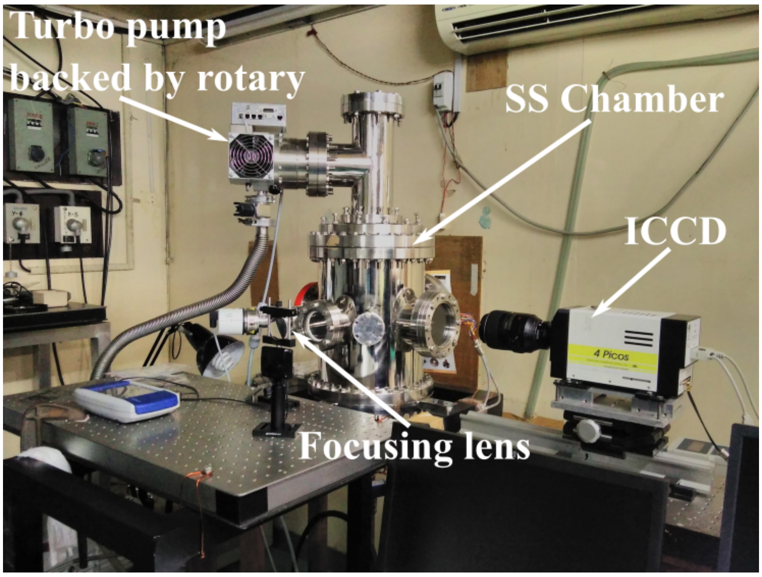

Figure 2.1: Photograph of vacuum system and ICCD camera used in these experiments

in usage of solid targets. The targets were thoroughly washed and completely dried using DI water to avoid contamination before placing inside the vacuum chamber. In case of the experiments with thin film, film is removed from the area where the laser beam is focused. And in case of solid target, distortion in terms of flatness of the target surface, arises after single laser shot. Therefore, target is required to be repositioned after each shot. For doing this, we have used two micro-controller based linear translators attached to each other which can move in X and Y-directions on the plane perpendicular to the incoming laser direction (i.e. Z direction). Target is placed on a translator system and its position can be controlled from outside of the chamber for a fresh position after each shot. No damage to the film substrate was noticed using the present laser fluence.

2.1.3 Laser systems

An Nd:YAG laser (wavelength 1064 nm and full width at half maxima is 8 ns, Quantel BrilliantB) has been used in these experiments for ablating target material to produce plasma. It can deliver maximum energy up to 850 mJ in single pulse mode at repeatation rate of 10 Hz. It has default beam diameter of 8 mm and the

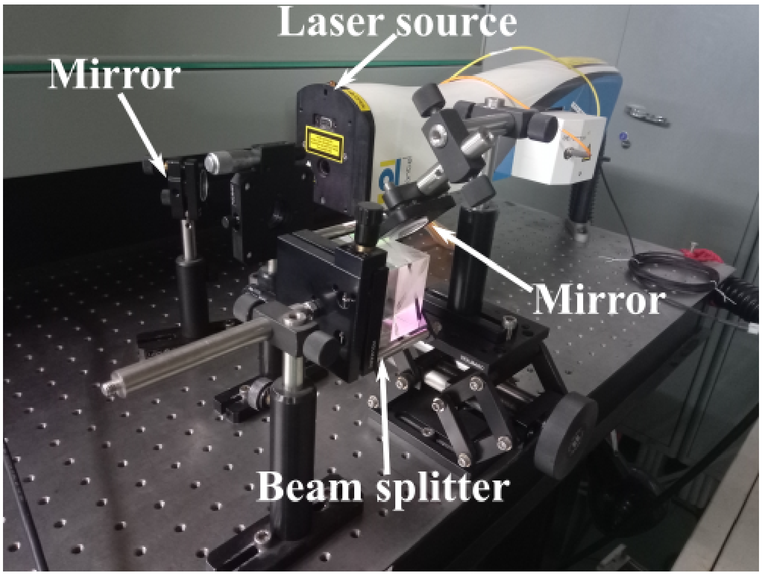

Figure 2.2: Photograph of Nd:YAG laser source used in these experiments

output energy has been monitored by changing the delay between Q-switch and flash lamp output. Normally this laser is focused on the target surface by a 30 cm plano-convex lens, using which also spot size can be monitored, placed outside the vacuum chamber and in front of one of the CF 100 windows fitted with transparent quartz glass. All the experiments described in this thesis work has been done in single shot mode. The energy of this laser beam has Gaussian profile. The energy of the laser beam (either single or split) was measured by using an energy meter (GentecE, Maestro, QE25LP-S-MB-QED).

2.1.4 Optics

Optical components such as mirror, half wave-plate, cube beam splitter and lens are required for aligning the laser beam into the vacuum chamber and to focus on the target surface at desired focal spot size which is 0.5 mm and 1 mm in our case. The arrangement of different components is shown as schematic diagram in figure 2.3 and in real photograph shown in figure 2.2 and 2.1. The first mirror M1 bends the laser beam at 90° angle and then on a cube beam splitter through a half-wave plate placed between the mirror M1 and cube beam splitter. The first mirror M1 is used to avoid the reflected light leaking into the cavity, which is harmful for the

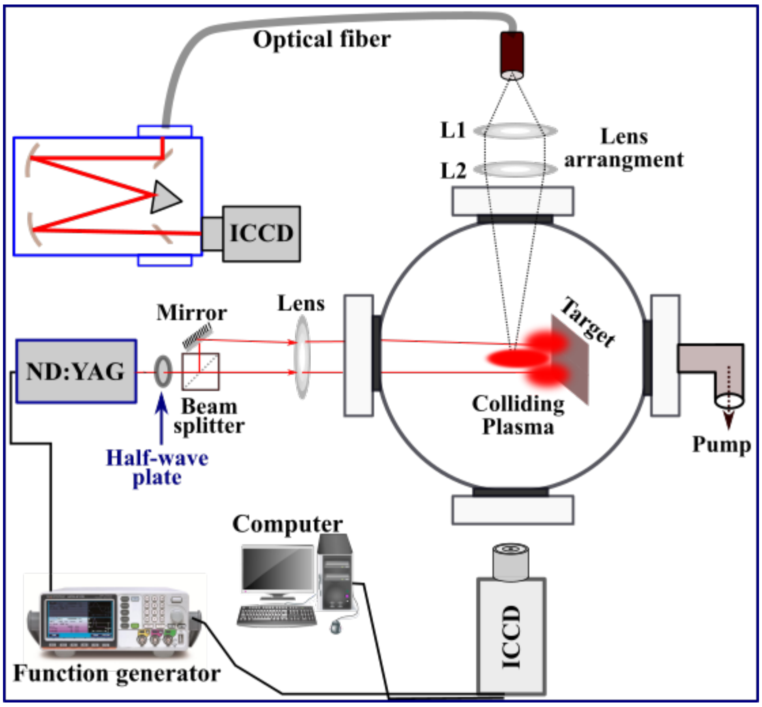

Figure 2.3: Schematic diagram of experimental setup

laser source. The beam splitter splits the single laser beam into two perpendicular to each other depending on the polarization of the incident light. Cube beam splitter is set such that the horizontally polarized part transmits easily without any change and the vertically polarized components gets reflected at the interface at 90° angle. The reflected part of the beam is bent by the mirror M2 placed just above the cube beam splitter (as shown in the figure 2.3). These two beams are aligned such that both are incident on the plano-convex lens L and focused at desired focal spot size on the target surface.

2.2 Plasma diagnostic systems

Laser induced plasma phenomenon is transient in nature having maximum emissive life-time persistent around 5-10 μs. Therefore very fast response (in pico or nano seconds) is required to probe the evolution dynamics of shape, size, expansion and parameters of the plasma. Therefore, we have used Intensified Charge Coupled Device (ICCD camera) for fast imaging of the plasma and Optical Emission

Spectroscopy (OES) method to estimate plasma parameters such as electron temperature, density and ion/neutral line emission profile with time. These diagnostics are useful to extract data for both temporally and spatially resolved analysis.

2.2.1 Intensified Charged Coupled Device (ICCD)

Intensified Charged Coupled Device or high speed ICCD camera (4 Picos Stanford Computer Optics, Inc.) is used in these experiments to capture the temporal and spatial expansion of plasma plume. It has time resolution of ∼200 ps and visible spectral range 350 - 750 nm and time jitter of < 1 ns. Time integrated 2 dimensional images provide information about the plasma plume shape, size, geometry, expansion velocity etc. The integration time of the camera is set as 5 ns to record the plasma plume expansion up to 400 ns. Beyond 400 ns integration time it is set as 10 ns as the emissivity decreases very low after the mentioned time delay. The camera is calibrated by taking image of a grid of known dimensions (2×2 mm^2) and printed on a white paper. The mesh grid image is shown in Fig. 2.4. From this image we have calibrated pixels of ICCD in terms of actual length. At least 5 images are taken to average the uncertainties in the data acquisition. It is observed that images are almost identical in most of the cases with uncertainties $< 5\%$. The background noise is subtracted by using Matlab software. For better representation the grey scale images are converted into Matlab pseudo-color (jet). Camera is calibrated and placed in the same plane but at a perpendicular window of the vacuum chamber as shown in Fig.2.1 and 2.3.

2.2.2 Spectrograph

In case of laser produced plasma several types of atomic processes e.g. excitation, ionization, recombination occurs, which exhibit characteristic atomic line emission. Optical Emission Spectroscopy (OES) is a fast, non-invasive and suitable technique to probe these characteristic emissions. OES also has advantage over other methods in terms of probing the plasma plume without creating any external interference by diagnostics. It is a simple way to estimate the plasma electron temperature and density along with the characteristic line emission. Therefore, it is widely used among the researchers.

Figure 2.4: Grid of 2×2 mm^2 squares, which is used for ICCD camera calibration. The deep black cross mark is used for positioning the camera.

A 0.5 meter spectrometer (Acton Advanced SP2500A, Princeton Instruments) coupled with an ICCD camera is used in these experiments (as shown in Fig.2.3). 1200/mm grating is used in this spectrometer which can record line emission ranging from 350 nm to 750 nm with 0.08 nm spectral resolution. Two plano-convex lenses are placed in such a way that the plasma produced inside the vacuum chamber is imaged on the tip of the fiber which is connected to the spectrograph, as 1:1 image. This is possible if the plasma is produced at the focal point of first lens L1 and tip of the optical fiber is placed at the focal point of the second lens L2. The optical fiber has 5 μm slit width and is fed into the spectrograph.

2.3 Diagnostic Techniques

In section 2.1 different components which have been used to acquire data from the laser produced plasma for further analysis, are described. Several atomic processes are involved in production of laser produced plasma. Transition of atoms from higher energy state to lower state emit radiation whose energy and shape are well defined. The shape of the emission line normally depends on the lifetime of upper level, external perturbation and velocity distribution of the plasma species. Therefore, the factors affecting the line emission profile must be taken into consideration for extracting plasma parameters properly. In case of laser produced plasma optical thickness or the opacity of the plasma is considered low and therefore can be neglected in our study.

2.3.1 Line Broadening

Emission in laser produced plasma basically consists of continuum radiation, bound to free or free-free radiation and bound state to bound state line emission. This emission depends on different parameters such as laser energy, material properties and ambient. Depending on these parameters the actual profile of emitted lines are broadened. There are mainly three types of line broadening mechanisms: natural broadening, pressure broadening and Doppler broadening. These are important to be considered for estimating plasma parameters.

(i) **Natural Broadening:** This type of broadening appears because of Heisenberg's uncertainty principle of lifetime and energy of a energy level under consideration for a particular transition. A transition having energy E and lifetime t will have uncertainty $\Delta E \approx \hbar/\Delta t$. This type of broadening is referred as natural broadening and has Lorentzian profile.

(ii) **Pressure Broadening:** Plasma particles are surrounded by ambient of neutrals, ions and electrons which interact continuously among each other. Ambient particles influence the emission process of radiators resulting in broadening and shift of their spectral lines. Both effects depend on particle density and velocity (i.e., temperature).

(iii) **Stark Broadening:** Broadening of spectral lines by charged particles (electrons and ions) usually dominates in plasmas and is termed Stark broadening. It naturally depends on the atomic structure of the emitting atom or ion and, since the atomic structure exhibits many regularities and similarities, one can expect this also for broadening and shift.

(iv) **Doppler Broadening:** Any motion of an emitter i.e. atoms/ions in a plasma will introduce shift in the observed wavelength due to Doppler effect. As the emitting particles in a plasma run in all possible directions, the emitters moving towards the observer will give a positive shift and the emitters moving away from the observer will give a negetive shift in frequency. This will contribute as a broadening in the observed wavelength. Plasma temperature are the average thermal motion of the plasma particles. Therefore, Doppler broadening increases with the increase in plasma temperature. In our study plasma temperature is only in the range of few eV. Therefore, Doppler broadening will be negligible.

2.3.2 Temperature Measurement

Plasma parameters like electron temperature and density have been estimated by optical emission spectroscopy (OES). Plasma electron temperature is measured by line emission ratio using Boltzmann equation as given below; [100]

$$\frac{I_{ij}}{I_{kl}} = \frac{\nu_{ij} A_{ij} g_i}{\nu_{kl} A_{kl} g_k} exp \frac{-(E_i - E_k)}{k_\beta T_e} \tag{2.1}$$

where I represents the line intensity of transition between two energy levels (i, j or k, l), ν is the spectral line frequency, A is Einstein coefficient, g represents the statistical weight of the energy level, E is energy, k_β is the Boltzmann constant, T_e is the electron temperature, and the subscripts i, j, k and l indicate the different energy levels. Normally non-resonant lines having large energy gap are chosen to avoid self-absorption and to decrease error in calculation. The other parameters such as Einstein coefficient, statistical weight etc., required for this calculation have been taken from NIST database. [135]

2.3.3 Density Measurement

Plasma is collection of charged particles. Therefore, Stark broadening effect is dominant in this type of ensemble. Electron density is measured by Stark broadening of line emission. The Stark broadening of emission line in plasma is attributed to the Coulomb interaction of electrons and ions. In general in laser produced plasma ionic contribution to the line broadening is ignored because it is very small. On neglecting the ionic contribution Stark broadening and electron density can be estimated by the equation, [105, 106]

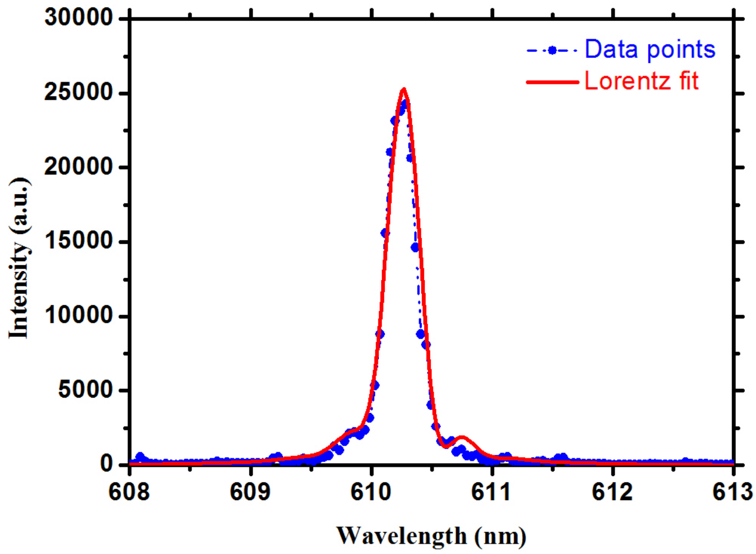

Figure 2.5: A typical diagram of Lorentzian fit

$$\Delta\lambda_{\frac{1}{2}} = 2\omega\frac{n_e}{10^{16}} \tag{2.2}$$

where, n_e is the electron density, $\Delta\lambda_{\frac{1}{2}}$ is the full width at half maxima (FWHM), ω is the electron-impact half width parameter which is weakly temperature dependent. The line has been fitted with Lorentzian. Instrumental width is rather small and hence not considered in fitting. Doppler and pressure broadening contributions can be neglected for the present conditions. We have used the value of ω from references [106, 129]

Here, the condition should be considered that this estimation for density calculation is valid in Local Thermal Equilibrium (LTE) conditions only. Local thermodynamic equilibrium for plasma has been verified in our case by using the McWhirter criteria which is generally used and states that the minimum value of electron density should follow the equation, [105]

$$n_e \geq 1.4 \times 10^{14} T_e^{\frac{1}{2}} (\Delta E)^3 \quad cm^{-3} \tag{2.3}$$

where, T_e (eV) is electron temperature and ΔE (eV) the energy gap for the transition corresponding to the shorter wavelength. McWhirter criteria is derived with the assumtion that plasma under consideration is homogeneous and stationary.

Therefore, McWhirter criteria is necessary but not a sufficient for LTE condition for transient plasma, such as laser produced plasma. If the expansion of the plasma is too fast, electrons and atoms don't get sufficient time to get in equilibrium. Therefore, in case of transient and inhomogeneous plasma the relaxation time τ_{rel} of the plasma should be smaller than the time of variation of thermodynamic parameters i.e. when the following eqn. 2.4 and 2.5 hold true. [101]

$$\frac{T(t+\tau_{rel}) - T(t)}{T(t)} << 1 \tag{2.4}$$

$$\frac{n_e(t+\tau_{rel}) - n_e(t)}{n_e(t)} << 1 \tag{2.5}$$

Equation 2.4 and 2.5 are the second criteria to be satisfied for the validity of LTE condition in a time-varying plasma. Relaxation time (τ_{rel}) is the time required for excitation and ionization to reach in equilibrium and described by eqn. 2.6. [83]

$$\tau_{rel} = \frac{6.3 \times 10^{14}}{N_e f_{mn} < g >} \Delta E_{nm} \left(kT_e\right)^{\frac{1}{2}} \left(\frac{\Delta E_m}{kT_e}\right) \tag{2.6}$$

Where T, f_{mn} and $< g >$ are plasma temperature in Kelvin, electron oscillator strength of the transition and effective Gaunt factor, respectively.

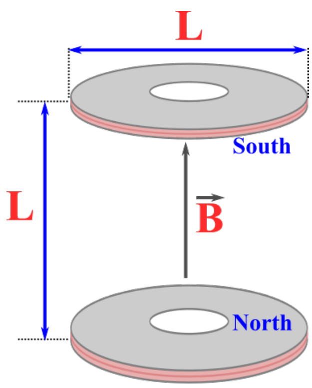

Figure 2.6: Schematic diagram of Helmholtz coil design used in our experiment.

2.4 External Magnetic Field Generation

Presence of external magnetic field affects the dynamics and properties of plasma plume significantly. To perform experiment under various conditions in the presence of an uniform external magnetic field, we have developed a Helmholtz coil which can generate magnetic field upto 7000 Gauss for a few mili-seconds time duration. The characteristics and dynamics of the plasma plume depends on the strength of magnetic field also. In this setup, magnetic field can be varied by changing the current passing through the Helmholtz coil which facilitates these experiments. It can be mentioned here that most of the published works have reported use of permanent magnet which can produce a constant field. Two pulsed power capacitor banks connected in parallel with fast ignitron based switch are used to supply the required current (upto 1.5 KA) to the Helmholtz coil. Proper calibration is done by mapping the temporal as well as spatial profiles of the produced magnetic field inside the Helmholtz coil. These profiles have been mapped using a high frequency Gauss meter (F W BELL, Model: 5180). All the components i.e. capacitor bank, ignitron switch, ICCD camera, laser, spectrograph etc. are synchronized through a synchronization setup having a function generator and delay generator.

2.4.1 Helmholtz coil parameters

Helmholtz coil is a combination of two circular coils having centre to centre separation along its axis equal to its radius. The current flow direction is same in both the coils and theoretically it produces uniform magnetic field in between the two coils. In the present case, it is made of non-magnetic stainless steel (1 mm thickness) with dimension 155 mm diameter which is smaller than the dimension of the vacuum chamber. It is placed inside the vacuum chamber and wires are connected from outside such that the vacuum does not get affected. A photograph of the Helmholtz coil is shown in Fig. 2.6. Twenty eight turns of teflon insulated copper wire having cross section of 2 mm are used in each coil of this assembly.

Magnetic field for different input voltage which is equivalent to current in Amp, is linear and it is shown in Fig. 2.7. Similarly, Figure 2.8 shows the spatial profile of magnetic field inside the coil for a particular voltage (i.e. 200 V). From this figure

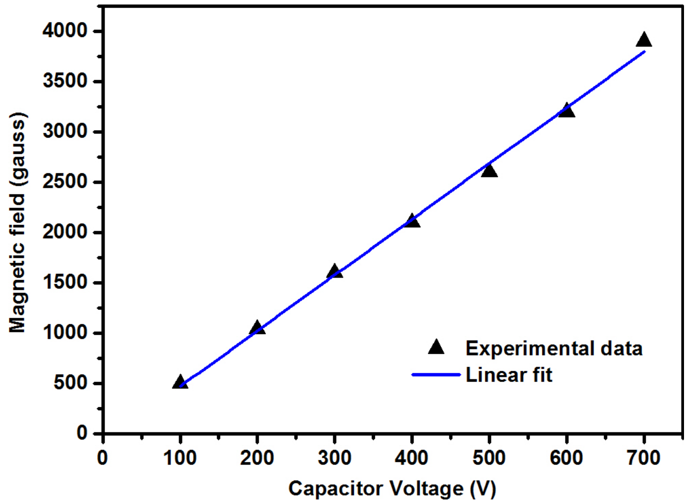

Figure 2.7: Magnetic field produced at the center of the Helmholtz coil for different input voltage.

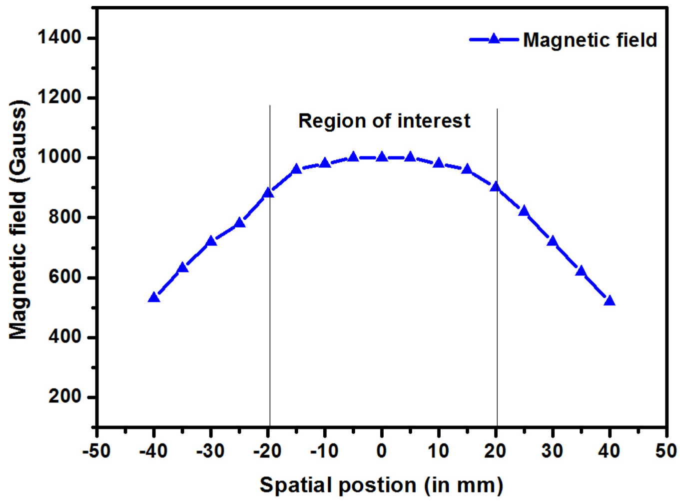

Figure 2.8: Spatial profile of magnetic field produced by Helmholtz coil for a particular voltage i.e. 200 V, considering the center as position zero (0).

it is confirmed that uniform magnetic field region which is around 40 mm and greater than the maximum expansion of the plasma plume in presence of magnetic field.

2.5 Summary

Briefly in this chapter, we have given detailed description of the experimental set-up, equipments used in the studies and diagnostic techniques such as fast imaging, optical emission spectroscopy, which have been adopted for our studies in this thesis work. The selected target is placed inside a non-magnetic stainless steel chamber at working pressure 2×10^{-6} mbar which is achieved by serially connected rotary and turbo molecular pumps. An Nd:YAG laser (wavelength = 1064 nm, full width at half maxima is 8 ns) has been focused through multiple optical arrangements on the targets. In case of study of colliding plasma under various conditions the laser beam is split into two having equal energy and focused by a plano-convex lens. An ICCD camera and spectrograph coupled with ICCD camera have been used for imaging and optical emission spectroscopy, respectively.

3

Effect of ablation geometry on the dynamics, composition and geometrical shape of thin film plasma

Ablation geometry of a target in laser produced plasma controls the shape, size, expansion dynamics and parameters of the plume to some significant extent. Effect of two different ablation geometries i.e. Front Ablation (FA) and Back Ablation (BA), on the expansion dynamics, geometrical aspects, compositions and characteristic parameters of laser produced plasma plume has been discussed in this chapter. Also. the effect of laser fluence, beam diameter (i.e. spot size) and ambient pressure has been highlighted for both the geometries. Fast imaging and spectroscopic techniques as described in chapter 2 have been used to diagnose the transient plasma phenomenon in the present case. Several important phenomena regarding shape, size, ion/neutral compositions, electron temperature and density of the plasma plume have been presented. A brief description of the target geometries is also given in the experimental scheme in section 3.2.

3.1 Introduction

Laser-matter interaction and the properties of the subsequently produced plasma plume have been studied extensively for a long time due to its importance in fundamental studies as well as application point of view. [1, 3, 4, 89, 95]. It has several applications in various disciplines such as laser processing of solid materials, laser induced mass spectrometry, elemental analysis, material science, thin film deposition, ion source generation, plasma diagnostics etc. [88, 91–94]

Apart from the conventional studies, laser induced plasma can be produced in two different geometries i.e. FA and BA of a thin film. This experiment is helpful for understanding a comparative study of plasma plume dynamics as well as characteristics for both the cases. Laser induced back ablation (BA), also known as laser blow-off, is a promising mechanism, where a laser beam penetrates through a transparent substrate and heats film-substrate interface resulting the expulsion of target material along the direction of laser beam [11, 48, 56]. Because of the specific nature of back ablated plasma plume, it has many applications in thin film deposition, reflectance study, material processing, micro fabrication, thermal to super-thermal neutral atomic beam generation and in tokamak edge diagnostics [10, 15, 97, 98]. It should be noted here that this type of study in back ablation geometry is only possible for a thin film target deposited on a highly transparent substrate. Along with this geometry, another important mechanism is front ablation (FA) of thin film. In such experiment, the incident laser heats the thin film deposited on a substrate and produce a very high temperature followed by rapid phase transition from solid into vapour. [111, 112]. Front ablation, particularly, of a thin film is less explored technique which can provide an atvantageous platform for a wide range of applications such as film removal, energetic particle generation and thin film study (e.g.,opacity, reflectance etc). [55, 96]

In view of above, a comparative study of plasma plume produced in FA and BA of a LiF-C thin film target has been carried out for different experimental conditions. LiF-C thin film has been chosen as target material in the present experiment because lithium has lower atomic mass, ionization potential and above all it has strong emission in the visible region which is highly suitable for tokamak edge plasma diagnostics.

3.2 Experimental scheme

The schematic diagram of the experimental set up is shown in Fig. 3.1. Nd:YAG laser (λ = 1064 nm, Δt $\approx$ 8 ns at full width half maxima) with parameters as described in chapter 2, is used to ablate LiF-C thin film in two different geometries

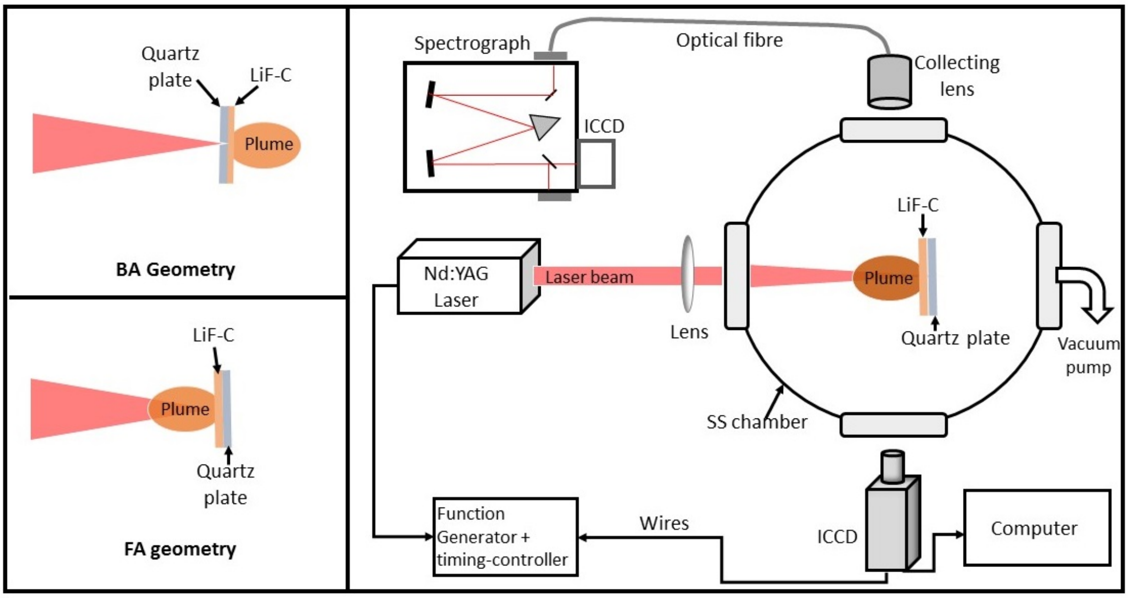

Figure 3.1: Schematic diagram of experimental set up.

i.e. front ablation and back ablation. LiF-C thin film (0.5 μm carbon and 0.05 μm LiF) is deposited on a transparent quartz substrate of 2 mm thickness and it is used as target in this experiment. The target plate (length $\times$ width $=$ 60 $\times$ 60 mm^2) is placed on a holding arrangement such that the focused laser beam is incident perpendicularly on the film coated surface of the target. The description of the target holding arrangement is given in section 2.1 of chapter 2. LiF-C thin film target is placed inside the vacuum chamber attached to the holder. Fine needle valve is used to vary the ambient pressure inside the chamber ranging from vacuum ($\sim 10^{-6}$ mbar) to 1 mbar of argon. The experiment is performed in single shot mode where operating parameters of laser are adjusted to set the desired laser fluence on the target surface. The ICCD camera (Intensified charge coupled device, 4 Picos, Stanford Computer Optics Inc) and is used for imaging of the plasma plume. Spectrometer (0.5 m, Acton Advanced SP2500A, Princeton Instruments) is used to estimate plasma electron temperature and density.

3.3 Results and discussion

3.3.1 Image analysis

Various features of laser induced plasma plume of LiF-C thin film produced by two different ablation geometries, i.e. front ablation (FA) and back ablation (BA) of thin film, have been presented. Effect of ablation geometry on the dynamics and geometrical shape of the expanding plasma plume is studied by analysing two dimensional images for both FA and BA plumes as a function of time delay and estimated the plasma parameters. Comparative study between FA and BA plumes in respect of its dependence on ambient pressure, laser fluence and spot size is presented in the following sections. Fig. 3.2 represents the sequence of images of FA and BA plumes, captured at different time delays, varying from 100 ns to 1000 ns in vacuum. Each image represents spectrally integrated emission intensity in the wavelength range 350 - 750 nm. Energy and spot size of the laser beam are set as 100 mJ and 1 mm respectively, which results in the laser fluence ~ 3.18 J/cm^2 at the target surface. Efforts have been made to ensure identical experimental conditions for the both front and back ablations.

A visual examination of the plume images reveals that in vacuum, plasma plume expands linearly and the emission intensity decreases gradually with time for the both ablation geometries. The plume expansion in vacuum is modelled as adiabatic expansion by Singh et. al., where the thermal energy of plasma species is converted into kinetic energy of the plasma plume. [7, 99] This process leads to decrease in electron temperature and density and hence decrease in emission intensity with increase in time delay. However, it is clearly observed that expansion velocity, plume emissivity, plume divergence and geometrical shape of FA plume are completely different in comparison to that observed in BA geometry. In case of FA, plasma plume expands with much higher velocity and it is highly divergent as compared to the scenario in BA plume. The calculated average expansion velocity of FA plume is 7.6×10^6 cm/sec, which is obtained by measuring the axial length of the plume front at its maximum for different time delays. In this geometry the axial velocity of the plume is almost comparable to the lateral velocity component (see Table I) and hence it attains nearly hemispherical shape. Due to the rapid expansion, emission intensity decreases quickly and after 1000 ns it is

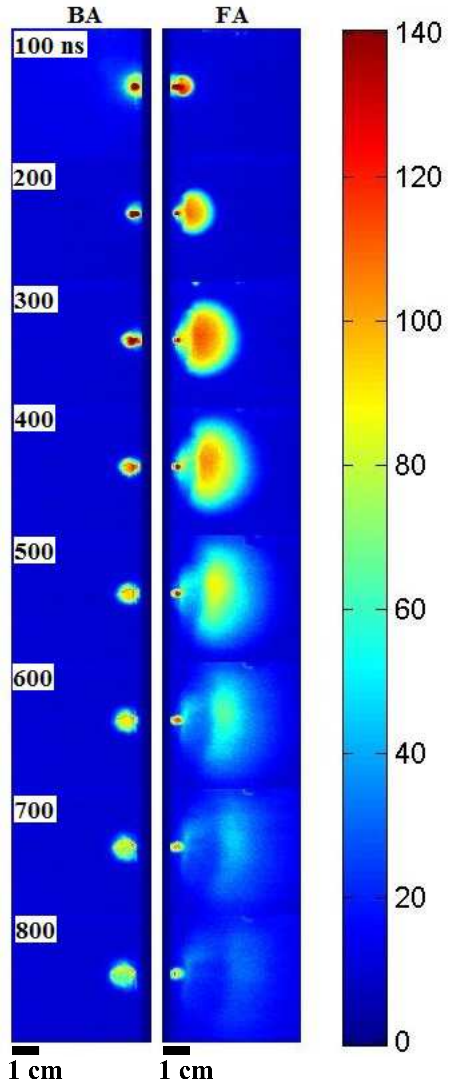

Figure 3.2: The sequence of images as a function of time delay (100 ns to 800 ns) of expanding plasma plume at 2×10^{-6} mbar for the both FA and BA geometry. Here integration time set as 5 and 10 ns for time delay up to 400 ns and >400 ns respectively. (Color bar represents the intensity in arbitrary unit)

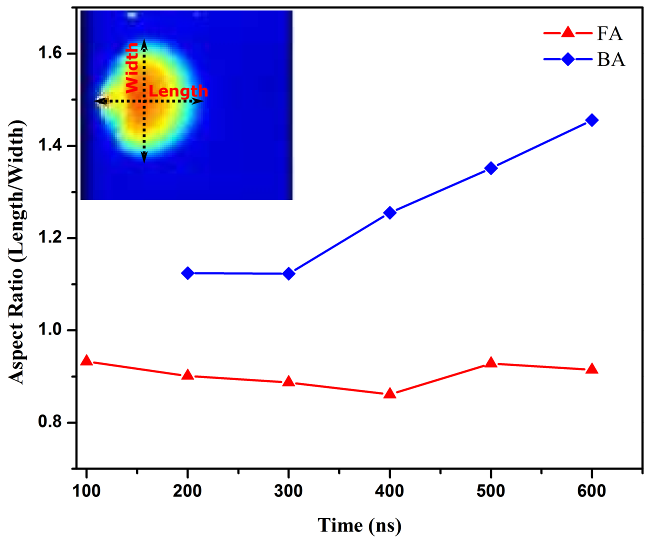

Figure 3.3: Aspect ratios (length/width) of FA and BA plumes as a function of time.

almost diffused and beyond the detection limit of the ICCD. It is also observed that the plasma plume gets split in FA geometry. Plume splitting in the absence of ambient gas can be explained as follows. The ablated species, mainly the ions, moving with high velocity form the leading edge of the expanding plasma plume. Collisional excitation of slow moving species (mainly the neutrals) represents the trailing portion of the plasma plume.

This scenario is completely different in case of BA plume where the expansion velocity and hence emissive dimensions of the plasma plume are much smaller than that observed in front ablation configuration (as seen in Fig. 3.2). The estimated expansion velocity of plasma plume in this geometry is $\sim 1.36 \times 10^6$ cm/sec, which is nearly 1 / 5^{th} of the observed velocity of plume in front ablation. Careful observation shows that the plume expansion in BA geometry is cylindrical in shape (upto $\sim$ 400 ns) and its expansion velocity along the axis is higher than its own lateral expansion velocity. The reason behind this phenomenon will be discussed latter. Also, due to slow expansion and low divergence, BA plume confines in small volume and hence its luminosity is higher and its emission sustains for longer times ($\sim$4 μs) in comparison to FA plume.

In order to present the time dependence of expanding plume geometry, aspect ratio (i.e. axial length/horizontal width of plume) of the plume is plotted as a function of time delay for both FA and BA geometries as shown in Fig. 3.3. Highly diverging and spherically symmetric nature of front ablation plume is clearly illustrated in this Fig. 3.3, where the aspect ratio is closer to unity and almost invariant with time. On the other hand, increasing trend in the aspect ratio indicates elongation of plume in back ablation geometry. Here, it should be noted that axial velocity of the plasma plume formed by front ablation of thin film is also much higher than the observed plume velocity ($\sim 3 \times 10^6$ cm/s) in bulk lithium ablation. [113] By comparing the plasma plume formed for different geometries i.e. FA and BA of thin film and bulk solid ablation, the present study suggests that FA plume is of particular importance and it can be used as a convenient method in energetic particle production. Also because of nearly uniform distribution of target material in a wide area, FA plume is ideal for large area thin film deposition.

Appearance of highly diverge and energetic FA plume and relatively slower and directed BA plume could be understood as follows. The thermal diffusion length can be estimated by the relation, $l = (Dt)^{1/2}$, where D and t are thermal diffusivity of the material and laser pulse width (8 ns), respectively. The estimated diffusion lengths are 1.8 and 0.17 μm for carbon and lithium fluoride films, respectively, which are larger than the thickness of both the films. Therefore, uniform heating of the target film by laser can be safely assumed. In case of front ablation and for the considered power density of the laser beam, the incident laser rapidly heats the irradiated area of the target film and its temperature reaches nearly its critical temperature. [97] This initiates phase explosion and hence the vaporized target film is ejected from the substrate surface in the form of energetic and diverge plasma plume as observed in Fig. 3.2. As we have discussed earlier, under similar experimental conditions, plasma plume produced by thin film deposited on quartz plate is expected to be more energetic in comparison to the bulk solid ablation because loss of energy through thermal diffusion is limited in the dielectric substrate.

TABLE I

Obtained parameters for FA and BA for (a) 1 mm spot and (b) 0.5 mm spot sizes.

Parameters	Values in FA	Values in BA
Axial velocity[a]	7.6×10^6 cm/s	1.36×10^6 cm/s
Axial velocity[b]	1.02×10^7 cm/s	1×10^6 cm/s
Transverse velocity	$4.1 \times 10^6 \quad cm/s$	$7.06 \times 10^5 \quad cm/s$
Kinetic energy of plume species[a]	~ 359 eV	~ 11.5 eV
Kinetic energy of plume species[a]	~ 646 eV	~ 6.2 eV
Axial velocity bulk Lithium target [113]	$3 \times 10^6 \quad cm/s$	—-
Electron temperature (300 ns)	$T_e \sim 2.83 \quad eV$	$T_e \sim 1.37 \quad eV$
Electron density (300 ns)	$n_e \sim 5.93 \times 10^{17}$ cm^{-3}	$n_e \sim 5.78 \times 10^{18}$ cm^{-3}

On the other hand, in case of back ablation the ablation mechanism is completely different from FA. In this case, laser beam initiates the melting at the interface of the thin film and the melting process propagates across the film and reaches at the front surface of the film [11]. The heating process by the laser beam continues until the vapour pressure at the interface of the film and quartz plate becomes large enough to propel the film material from the substrate. The melt through time i.e. time required to complete melting of the film across the film thickness is one of the important parameters which decides the dynamics and geometry of the ejected material. The melt through time depends on several factors e.g. laser fluence, pulse duration, spatial profile of the laser beam, film thickness and thermal properties of the film. For the present experimental parameters, melt through occurs before the termination of laser pulse and molten material is continuously heated by laser beam and increase the pressure at the film-substrate interface. However, Gaussian laser beam profile as in the present case, causes uneven melting of the irradiated surface area. Melt through occurs rapidly at the centre portion of the irradiated area where laser intensity is maximum and hence the target vapour gets released through a comparatively small opening (which coincides with Gaussian peak) in comparison to the beam size. This prevents further increase of vapour pressure by laser heating. As a consequence the target materials are ejected with comparatively small velocity and more directed as the present observation depicted in BA case.

Above argument is strongly supported by observed images for different laser spot sizes of ablating laser. Comparative illustration of laser spot size dependence on the FA and BA plume is depicted in Fig. 3.4. The sequence of images of

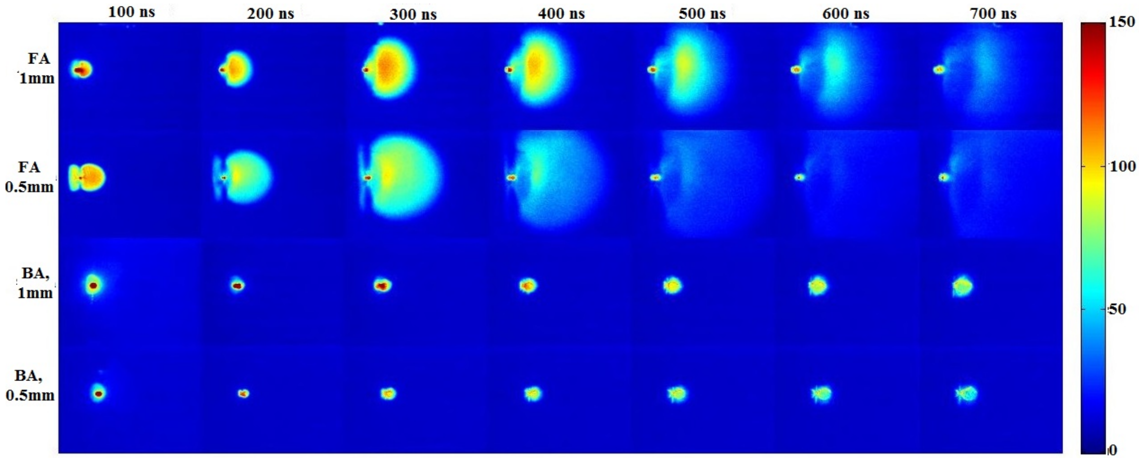

Figure 3.4: Time series of the FA and BA plasma plumes at two different laser spot sizes (i.e. 1 mm and 0.5 mm) at 2×10^{-6} mbar.

FA and BA plumes for 1 mm and 0.5 mm beam spot diameters are shown in this figure. Laser energy is fixed at 100 mJ for both the beam diameters and hence the corresponding laser fluence for 1 mm and 0.5 mm diameters are 3.18 and 12.7 J/cm^2 respectively. All other experimental parameters are identical for both the cases. As can be seen in Fig. 3.5, the plasma plume in FA geometry significantly depends on laser energy density. In this case, significant increase in axial as well as lateral velocities and hence increase in overall dimension of the FA plume is observed with smaller beam spot size (i.e. 0.5 mm diameter). Spot size dependence of plume expansion is more clear in plume dimension along axial direction vs time delay plot as shown in Fig. 3.5. The average axial velocity of the plume is estimated from the slope of the best linear fit of the data. The estimated average axial velocity for 0.5 mm diameter is $\sim 1.02 \times 10^7$ cm/sec, which is 1.3 times higher than the observed velocity in case of 1 mm beam diameter. Further, it appears that for smaller beam size plume becomes more symmetric spherically in comparison to that observed with 1 mm beam diameter. Also due to rapid expansion of plume (and hence faster adiabatic cooling) larger in size and less luminous plasma plume is observed in case of 0.5 mm beam diameter. These observations are in line with above mentioned explosive ablation in case of FA.

Laser spot size dependence on the BA plume is completely different to that observed in case of FA. We could not observe any significant change in dynamics

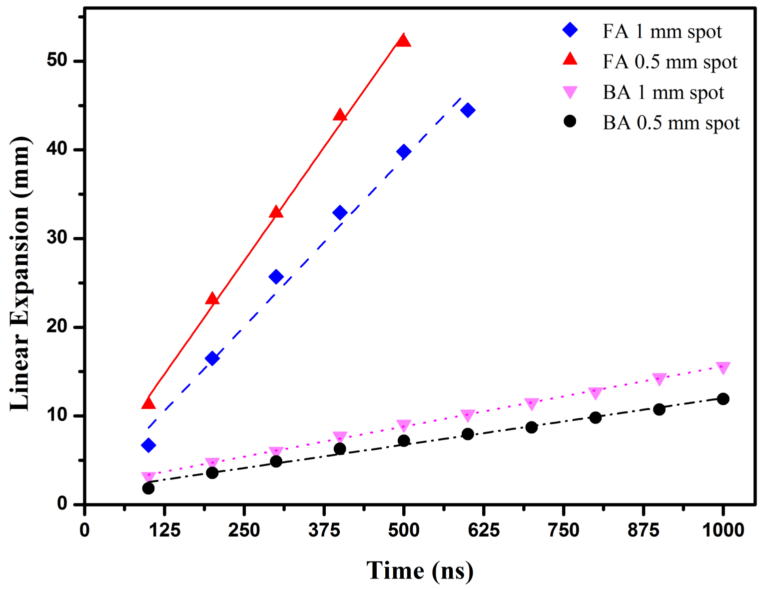

Figure 3.5: Plume length vs time plot for both the FA and BA geometry at 2×10^{-6} mbar for the laser spot size 0.5 and 1 mm.

and geometrical shape of the plume by reducing the laser beam diameter from 1 mm to 0.5 mm. It is interesting to see that even with the increase of laser fluence four times by reducing the spot size from 1 mm to 0.5 mm, the linear expansion velocity is comparatively smaller than the observed velocity with 1 mm diameter as shown in Fig. 3.5. The average expansion velocity of BA plume for 1 mm and 0.5 mm beam diameters are $\sim 1.36 \times 10^6$ cm/s and $\sim 1 \times 10^6$ cm/s respectively. This is again in agreement with above discussed correlation between melt through time and BA plume velocity. Higher power density in confined area facilitates fast melt trough which prevents the build-up of vapour pressure by laser heating. As a result material ejected with relatively lower stagnation pressure reflects in slow expansion of BA plume with 0.5 mm beam diameter.

As per above discussion related to the ablation mechanism of the FA and BA induced plasma plumes, one can expect that charge particles dominate in FA plume as compared to BA plume. This could be clearly visible in Fig. 3.6, where ratio of emission intensity of Li neutrals (integrated area of emission lines) recorded in FA and BA configurations are plotted as a function of time delay. It has been observed that ratios of Li I (BA) to Li I (FA) are always greater than one throughout the considered time delay range for the both ground state at Li I 670.8 nm as well as excited state at Li I 610.3 nm lines. It has been observed that up to 400 ns, for Li I 670.8 line emission intensity in the BA configuration is 9 times higher in comparison to that observed in the case of FA.

Further, we have also compared the plasma temperatures (electron temperature) of FA and BA plumes which contribute significantly in characteristic features of both the plumes. The electron temperature is estimated by emission intensity ratios of two neutral lithium lines (i.e. Li I 610.3 and Li I 670.8) using the Boltzmann relation [100],

$$\frac{I_{ij}}{I_{kl}} = \frac{\nu_{ij} A_{ij} g_i}{\nu_{kl} A_{kl} g_k} exp \frac{-(E_i - E_k)}{k_\beta T_e} \tag{3.1}$$

where I is the line intensity of the transition between two energy levels, ν is the frequency of the spectral line, A is Einstein's coefficient, g represents the statistical weight of the energy level, E is the energy, k is the Boltzmann constant, T_e is the electron temperature, and the subscripts i, j, k and l indicate the energy levels. As this relation is valid in LTE condition, we confirm the validity of the McWhirter criteria for the present plasma condition which states that the minimum density for LTE is given by [101],

$$n_e \geq 1.4 \times 10^{14} T_e^{\frac{1}{2}} (\Delta E)^3 \quad cm^{-3} \tag{3.2}$$

where T_e (eV) is the electron temperature and ΔE (eV) is the energy difference between the states. In our experiments for the maximum electron temperature of ~6.33 eV and for the largest energy gap (2.031 eV) of the selected transition (610.3 nm) this criteria predicts a lower limit of $n_e = 2.95 \times 10^{15} \quad cm^{-3}$. In the present case electron densities (n_e) are estimated by the Stark broadening of Li I 670 nm line using the relation, [105, 106]

$$\Delta\lambda_{\frac{1}{2}} = 2W \frac{n_e}{10^{16}} \tag{3.3}$$

The electron impact parameter (W) for Li I (670.8 nm) line is taken from Ref. 24. The lowest value of estimated spatially (3 mm away from the target surface) integrated electron density is 5×10^{16} cm^{-3} in this study. Therefore, the electron densities satisfy the LTE condition. Here the lower electron density in FA case could be correlated with rapid expansion of FA plume and acquire a much larger

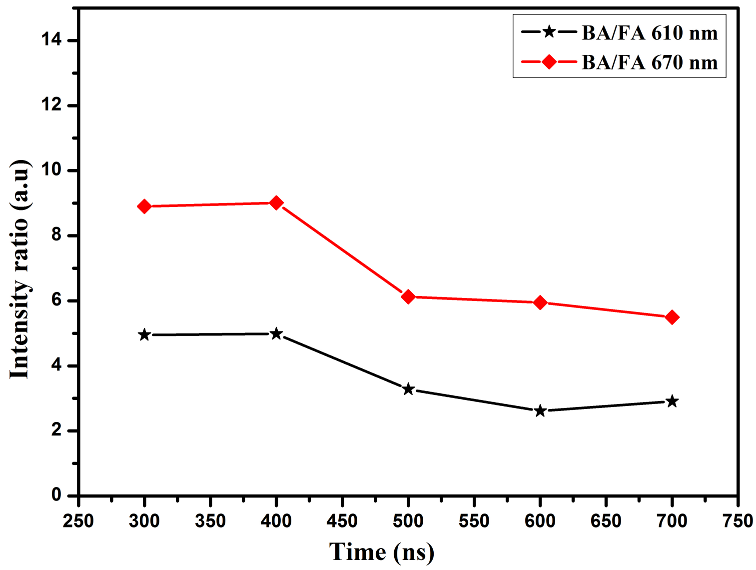

Figure 3.6: Intensity ratios of 670(BA)/670(FA) and 610(BA)/610(FA).

volume at the onset of time delay in comparison to BA plume.

Also, spatially integrated electron temperature (3 mm away from target surface) as a function of time delay obtained from FA and BA configurations is shown in Fig. 3.7. Here, the maximum shot to shot variation in integrated intensity is less than 2% and therefore, overall maximum uncertainty in electron temperature measurement is approximately $\sim 5\%$. At 2×10^{-6} mbar, the estimated electron temperature shows the increasing trend with time for both the cases (Fig.3.7(a)). This increasing trend in the electron temperature might be because of the contribution of the luminous plasma plume close to the target surface which persists over longer time delay. However, it is observed that the maximum electron temperature in case of FA is $\sim$ 2.5 times higher than the observed temperature in BA. This is in agreement with the present observation, that is plasma plume is more energetic and diverge in case of FA configuration. We have also estimated the electron temperature in presence of 2×10^{-1} mbar ambient argon pressure, where its trends is completely different in comparison to observed variation in case of vacuum (see, Fig.3.7(b)). At 2×10^{-1} mbar pressure, electron temperatures for both the cases (FA and BA) decrease with time where estimated temperature in FA is always lower than the observed temperature in BA configuration. It will be explained in the following paragraph.

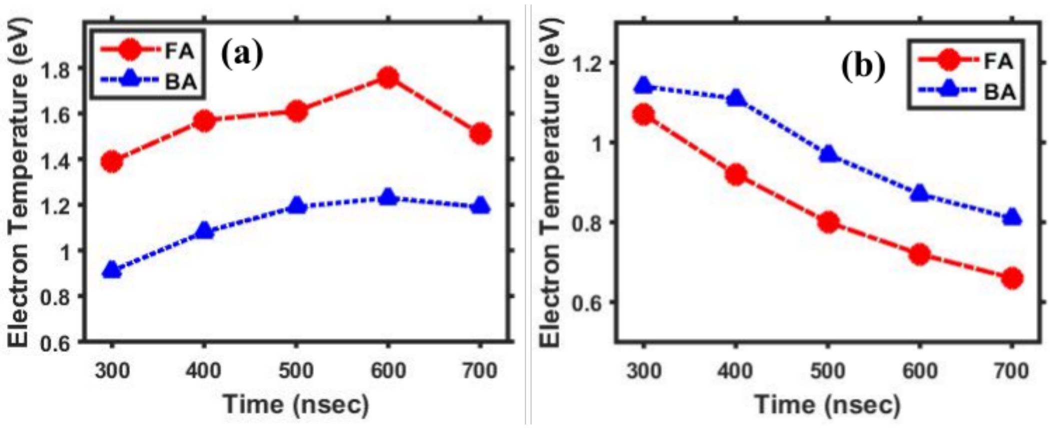

Figure 3.7: Temporal variation of electron temperature in FA and BA geometry at (a) 2×10^{-6} and (b) 2×10^{-1} mbar.

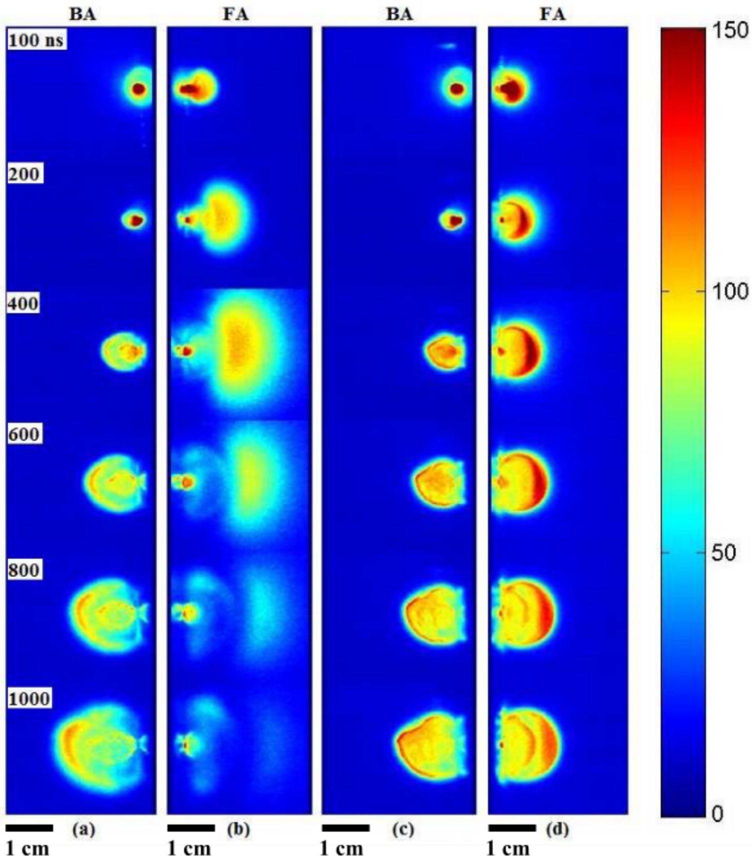

Figure 3.8: The sequence of images of FA and BA plasma plumes in 2×10^{-2} mbar (a,b) and 2×10^{-1} mbar (c,d).

Characteristic expansion of FA and BA plumes is compared in the presence of argon gas. Fig. 3.8 shows the time resolved images of FA and BA plume in presence of 10^{-2} mbar and 10^{-1} mbar Argon pressures. Laser energy and beam diameter were set at 100 mJ and 1 mm respectively. It can be seen from Fig. 3.8, plume dynamics, shape and its luminosity are changed significantly with the introduction of ambient gas. At 10^{-2} mbar ambient pressure and in case of FA, the plasma plumes are stratified into two components which are clearly separated after 400 ns, there after designated as fast and slow components. A bright portion associated with the target surface sustains for longer period. Initially the emission intensity of the fast component increases with time and starts decreasing with further increase in time. Stratification of plasma plume in the presence of ambient gas has been investigated by several workers in the past [4,103,104,107]. General interpretation of the plume splitting is that part of the plume species has little interaction with ambient atoms and hence its velocity is comparable to the observed velocity in vacuum. On the other hand, part of plume species suffer multiple collisions with ambient atoms and therefore expand with lower velocity as compared to faster counterpart. Above situation arises in the collisional regime where ambient atoms penetrate inside the expanding plasma plume [108, 109]. At a fixed background pressure, the collision between plume species and ambient gas can be justified when the mean free path of the ablated species are of the order of plume dimension. We have estimated the mean free path for the plume species in argon environment using the model based on sputtering of atoms by background atoms [110]. At 10^{-2} mbar argon pressure, the estimated mean free paths for Li and C atoms are 13 and 15 mm, respectively, which are comparable to the observed size of the plume at this pressure and hence FA plume expansion in a collisional regime for this pressure can be assumed.

At similar background pressure (2×10^{-2} mbar), scenario is completely different in the case of BA configuration. It can be clearly seen from Fig. 3.8 that a luminous and nearly semi-circular front ahead of the plasma plume starts to develop around 200 ns time delay. Since this front is clearly separated from the plume and hence it can be considered as a plasma plume induced shock front. Also, shock front expands with slightly higher velocity compared to the plume velocity and hence the shock front and plume get separated as the time progresses. The strong shock generation in case of BA plume can be understood as follows; relatively dense (less diverge) and directed BA plume compress the ambient gas in a localized region more efficiently in comparison to the highly diverge FA plasma plume. Therefore, in BA geometry, shock front is clearly visible. On the other hand, we could not observe any signature of shock formation in the case of FA at 10^{-2} mbar pressure.

With further increase in ambient pressure to 2×10^{-1} mbar, the interpenetration between the plume species and ambient is limited and a sharp contact boundary at the interface between the plume and ambient gas is formed as can be seen in Fig. 3.8. In this case plasma plume experiences the resistive force and hence is confined in a small volume. Sharp contact boundary and confinement effect is observed in both the cases (FA and BA). However, compression of plume species by the dense background gas is more visible in case of FA where significant density jump (bright patches in the image) is observed at the leading edge of the plume. Also, the intensity as well as life time of the plasma luminosity is increased significantly in comparison to the lower pressure regime. This is because of the increase in collision frequency in confined plasma and hence probability of excitation of plume species is also increased. Further, from the visible examination of plume images in vacuum and 10^{-1} mbar of argon pressure, it can be noticed that FA plume gets confined more efficiently (with respect to its size in vacuum for onset of time) as compared to BA plume. This is because of the presence of ambient gas, kinetic energy of plume species is transferred to the ambient atoms mainly through elastic collisions between them. As already seen FA plume is more energetic and hence rapid loss of expansion velocity thereby effective confinement is expected in this case. This is also supported by the observed electron temperature pattern in the case of FA and BA at 2×10^{-1} mbar pressure as shown in Fig.6.7(b). Unlike the case of vacuum, electron temperature is decreased with time for both the cases but temperature of FA plume is lower than the BA plume at a fixed time delay which indicates faster thermalization of FA plume. Here, it should be noted that the decrease in luminosity of the plasma plume due to decrease in electron temperature for high ambient pressure is compensated by increase in the density due to plume confinement as can be seen from the high luminosity sustained for a longer time.

The plume expansion in FA and BA geometry and in different pressure regimes can be presented in a better way by monitoring the plume length (distance covered by plume in axial direction) as a function of time. As discussed earlier, plume

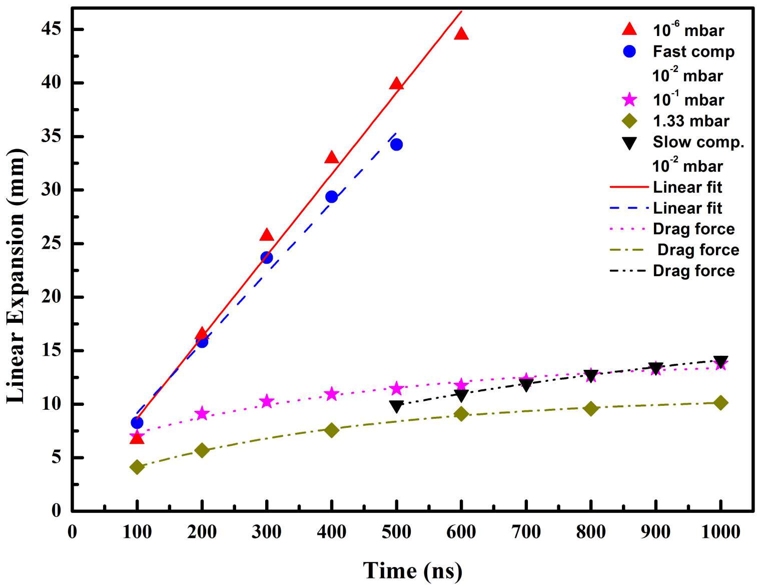

Figure 3.9: Axial position vs time plot in front ablation geometry at different pressures

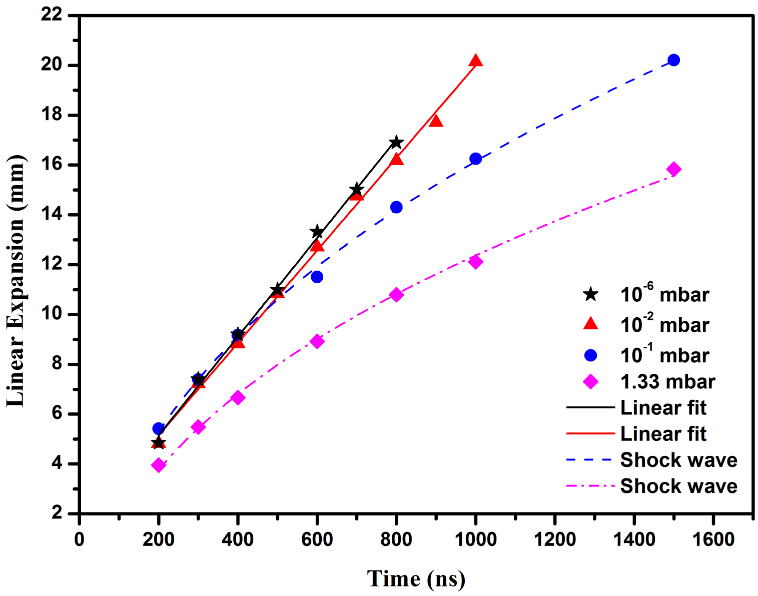

Figure 3.10: Axial position vs time plot in back ablation geometry at different pressures

expansion shows characteristic dependence with different pressure of ambient argon gas. The variation of plume length as a function of time at various Argon pressures, varying from 2×10^{-6} to 2×10^{-1} mbar in FA geometry is presented in Fig. 3.9. At 2×10^{-2} mbar ambient pressure, length vs time curves are plotted seperately for fast and slow components. Here it can be clearly seen that the expansion of the fast component is almost independent of ambient gas and it is similar to vacuum-like expansion. The slower part of the plume experiences the resistive force and its expansion is well fitted with the drag force model [30]. This is in agreement with the previous discussions of the plasma plume stratification by the introduction of ambient pressure. Also the plasma plume expansion at 2×10^{-1} and 1.33 mbar, respectively, follows drag-force model, which is given by the equation,

$$z = z_f[1 - exp(-\beta t)] \tag{3.4}$$

Here, β is the slowing coefficient and z_f is the stopping distance. The best fitted parameters results in the slowing coefficients $\beta = 2.3 \times 10^{-3}$, 2.5×10^{-3} and stopping distances 8.73 cm and 8.57 cm at $\sim 10^{-1}$ and $\sim$1.33 mbar, respectively.

On the other hand upto 2×10^{-2} mbar pressure ambient gas effect is not visible in BA geometry, where the plume dynamics follow the linear expansion as shown in Fig. 3.10. In contrast to front ablation, at 2×10^{-1} mbar and 1.33 mbar, BA plume follows shock-wave model as has been discussed previously. The shock-wave model is given by, [29]

$$z = \left(\frac{E_0}{\rho_b}\right)^{0.2} t^n \tag{3.5}$$

Where, E_0 is proportional to the laser energy density and ρ_b is the density of background gas. The best fitted curve shows the value of n as 0.4 for both pressures 2×10^{-1} and 1.33 mbar, respectively, which is in close agreement with shock-wave model.

3.4 Conclusion

To conclude this chapter, a detailed study on comparative analysis of laser produced plasma parameters in front and back ablation geometries has been discussed in this chapter. Also, the effect of ambient pressure, laser spot size and deposited laser energy on expansion dynamics and characteristic parameters of the plume has been demonstrated. It is observed that plume parameters, e.g. kinetic energy, shape, size, composition and plasma temperature are significantly different in these two geometries i.e. front and back ablations. The plasma plume expands in spherical shape with higher velocity ($\sim 7.6 \times 10^6$ cm/sec) in case of front ablation geometry compared to cylindrical plume expanding with a relatively lower velocity ($\sim 1.36 \times 10^6$ cm/sec) in back ablation geometry in vacuum. Highly energetic and spherically symmetric plasma plume which is observed in FA case, is in line with explosive ablation (phase explosion). On the other hand, the cylindrical shape and lower expansion velocity of plasma produced in BA geometry is due to the expulsion of material because of the vapour pressure built at the film substrate interface. Again, the observations of laser spot size dependency demonstrate the film removal through the small orifice resulting in generation of directed plume in case of back ablation. Also, differences in the dynamics of expanding plumes in these two geometries are correlated with their ablation mechanisms and observed plasma parameters. This study will have implication in developing experimental technique (ablation geometry) for controlling the characteristic parameters and dynamics of expanding plasma in different applications according to the requirement.

4

Compositional analysis of laser produced plasma

Composition analysis of plasma and its importance for various applications have been discussed in this chapter considering LiF-C thin film as a target for producing plasma by using laser ablation mechanism in two different geometries i.e. front and back ablation (FA and BA) and two ambient pressures (i.e. 2×10^{-6} and 2×10^{-1} mbar argon, respectively). A detailed description of the ablation geometries is given in chapter 3. Composition analysis i.e. ion to neutral ratio (i.e. n_i/n_a), neutral abundance for FA and BA ((n_{BA}/n_{FA})) and their temporal evolution in both geometries are important information for various applications. Two different approaches viz Atomic Data and Analysis Structure (ADAS) analysis as well as integrated intensity ratio of Li I 670.1 nm and Li I 610.3 nm lines assuming LTE conditions are explored and the outcome is described in this chapter. The present attempt will be interesting from the view point of understanding the evolution of plasma composition in various geometries/configurations of laser ablation which has important implications in various applications e.g. pulsed laser deposition and laser cleaning.

4.1 Introduction

The overview of laser produced plasma study and earlier works have been discussed in chapter 1. As mentioned before that laser produced plasma has tremendous applications viz. laser processing of materials, elemental analysis, thin film deposition, ion source generation and plasma diagnostics. [9, 94, 144, 145] Also, the dependence of plasma dynamics and parameters on different ablation geometries is discussed in chapter 3. It has been discussed in that chapter that, when a laser is incident from the rear side of a thin film target and produces plasma plume expanding along the laser direction, is called Back Ablation or BA plasma. This type of plasma has also been reported as Laser Blow-Off (LBO) plasma. [145, 146] Rear surface or back ablation of thin film (shown in Fig. 4.1) deposited on a transparent substrate using laser beam is promising from the application point of view as well as fundamental analysis of plasma parameters. Because of the specific nature of plasma plume generation and its properties, it has better prospects in the deposition of thin film, material science, micro fabrication, beam generation of energetic particles and diagnostics. [54, 145, 147]

Besides this, front ablation (FA) of thin film (Fig. 4.1) is another mechanism where the film deposited on a transparent substrate is ablated by an incident laser focused on the thin film in a conventional method i.e. the laser is incident from the front side and this arrangements can be seen in the upper image in Fig. 4.1. Front ablation of thin film can also facilitate range of applications such as removal of thin film, laser cleaning etc. [96, 145] In view of the above, a comparative study of LiF-C thin film in FA and BA geometries is an important aspect to be carried out under various experimental scenarios. Part of this study and the findings have been discussed in chapter 3 and in continuation of that composition analysis is presented in this current chapter.

Because, compositional analysis of the plume is an important aspect for controlling the plasma parameters through optimization of the conditions in case of pulsed laser deposition and laser cleaning. Recently, it has been reported that back ablation is favourable for better film deposition and cleaning of glassware. [148, 149] Some works were reported regarding the study of front and rear ablation in laser plasmas. [150] However, a proper compositional analysis was not attempted in the past. We have reported some salient features of plasma plume dynamics in different geometries. [151] In this chapter we describe the compositional analysis of the plasma plume.

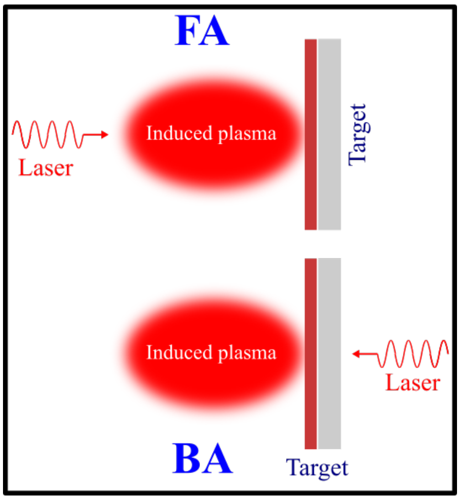

Figure 4.1: Schematic diagram of Front Ablation (FA) and Back Ablation (BA) geometries.

4.2 Experimental scheme

The experimental set up is shown in Fig. 2.3 in chapter 2. [151] Briefly, an Nd:YAG laser having fundamental wavelength of 1064 nm (pulse width ∼8 ns at FWHM) is used to create plasma plume of LiF-C thin film target in two different geometries i.e. FA and BA. LiF-C thin film (0.5 μm carbon and 0.05 μm LiF) deposited on a transparent quartz plate of 2 mm thick is used as target. The thin film coated target plate (60×60 mm^2) is placed in a holding arrangement normal to the laser beam. The whole arrangement is kept at the center of a cylindrical stainless steel vacuum chamber. The target holder is fixed with a base which is connected to a motor and a position micro-controller. The experiment has been done in single shot mode and the required laser fluence onto the target surface has been achieved by controlling the laser operating parameters.

Optical emission spectroscopy (OES) has been used to calculate the plasma electron temperature and density. A custom made collimator (Andor Collimator, model- ME-OPT-0007) connected to a spectrometer (0.5 m, Acton Advanced SP2500A, Princeton Instruments) through optical fibre collects the emission (up to 4 mm from target surface) of the transient plasma. The spectrometer output is coupled with an ICCD and it has ∼ 0.08 nm resolution. A micro-controller based timing generator having <1 ns timing jitter synchronises the spectrograph, ICCD camera and laser. Emission is collected from the same location of the plume at 2 mm distance from the target surface for both BA and FA geometries and experimental conditions are also maintained same. Moreover, the spectrometer detector response is uniform for the spectral lines taken in the study.

4.3 Results and discussions

4.3.1 Line spectra and plasma parameters:

A typical energy level diagram showing Li I 610.3 nm (non-resonance) and Li I 670.8 nm (resonance) lines is shown in Fig. 4.2. Figure 4.3 shows typical spectrum lines Li I 670.8 nm and 610.3 nm in front ablation geometry at 2×10^{-6} mbar ambient pressure which can be approximately considered as vacuum. Figure 4.3 presents that both the resonance (Li I 670.8 nm) and non-resonance (Li I 610.3 nm) lines have sufficient intensity under these conditions, which is suitable for spectral analysis of plasma.

The electron temperature has been calculated by using ratio of two neutral lithium line intensities i.e. Li I 610.3 and Li I 670.8 nm using the Boltzmann relation as it is given in equation 4.1 and it has been discussed in detail in chapter 2. [100] Here, we would like to mention that one of the factors that can affect line intensities is the optical thickness of the plasma. As Li I 670.3 nm line originates from the ground state, it is likely to be more prone to optical thickness. However, in the present experiment (as will be discussed latter) we rule out the contribution of optical thickness as neutral density is rather low as compared to electron/ion density and the plasma thickness is very small (few mm).

$$\frac{I_{ij}}{I_{kl}} = \frac{\nu_{ij} A_{ij} g_i}{\nu_{kl} A_{kl} g_k} exp \frac{-(E_i - E_k)}{k_\beta T_e} \tag{4.1}$$

Where, I is the line intensity of the transition between two energy levels, ν is the frequency of the spectral line, A is Einstein's coefficient, g represents the statistical weight of the energy level, E is the energy, k_β is the Boltzmann constant, T_e is the electron temperature, and the subscripts i, j, k and l represent the energy levels. The temporal evolution of the estimated electron temperature is shown in Fig.

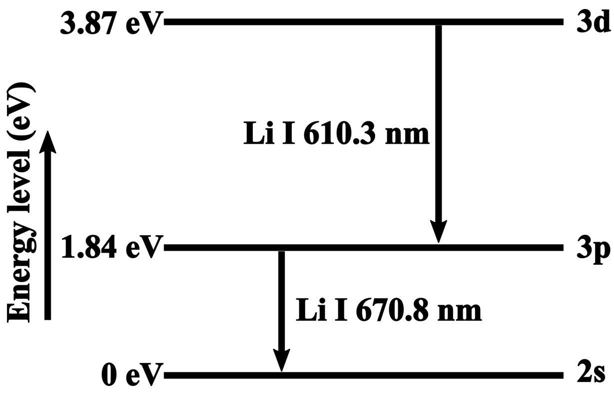

Figure 4.2: Schematic diagram of energy level showing Li I 610.3 nm (non-resonance) and Li I 670.8 (resonance) nm transitions.

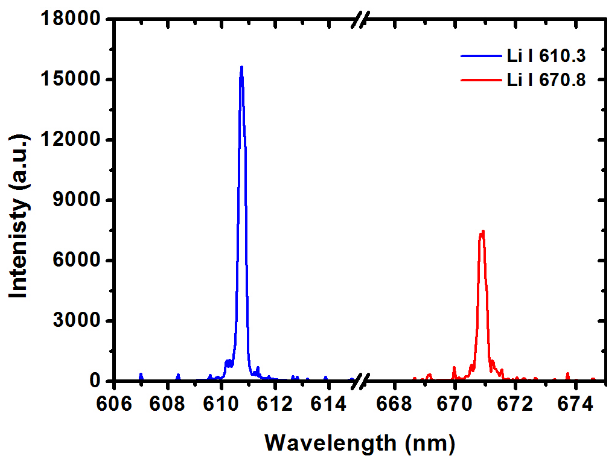

Figure 4.3: Emission profile in front ablation of Li I 610.3 nm and Li I 670.8 nm at 400 ns time delay in vacuum (2×10^{-6} mbar).

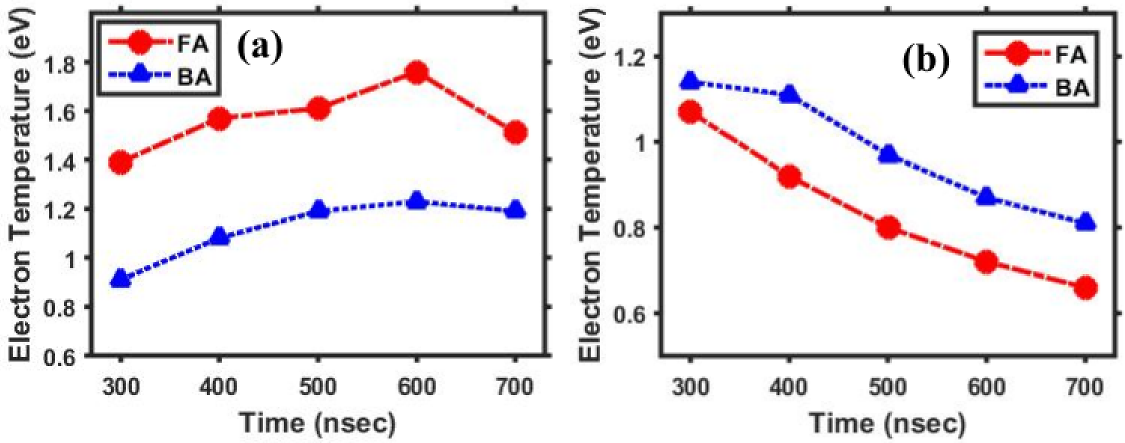

Figure 4.4: Temporal evolution of electron temperature in FA and BA geometries in vacuum (a) and at 2×10^{-1} mbar (b).

4.4. We would like to mention that obtained electron temperatures are less than the energy difference between the upper levels of these two transitions and hence the two line ratio method can be safely applied in this case. The uncertainty in temperature measurements is around ≈5 - 10%. As can be seen from Fig. 4.4 that under vacuum conditions electron temperature goes on increasing with time contrary to the case of 2×10^{-1} mbar where opposite trend is noticed. Probably, the increase in temperature with time in vacuum may be due to inverse bremsstrahlung absorption, whereas the decrease at higher pressures may be due to increased collisions with the ambient which results in decrease in electron temperature. [152]

Electron density is determined from the Stark broadening of 610.3 nm line by using equation 4.2 as given below. [105, 106]

$$\Delta\lambda_{\frac{1}{2}} = 2\omega\frac{n_e}{10^{16}} \tag{4.2}$$

Here, n_e is the electron density, $\Delta\lambda_{\frac{1}{2}}$ is the full width at half maxima (FWHM), ω is the electron-impact half width parameter which is weakly temperature dependent and it is taken from Ref. [106]. A typical Lorenzian fit for Li I 610.3 nm line is shown in Fig. 4.5. Other broadening parameters such as Doppler and pressure broadening are neglected in the present case because of their negligible contributions. Electron density shows slight increase in vacuum but shows decreasing trend at 2×10^{-1} mbar (shown in Fig. 4.6). This can be anticipated that under vacuum conditions

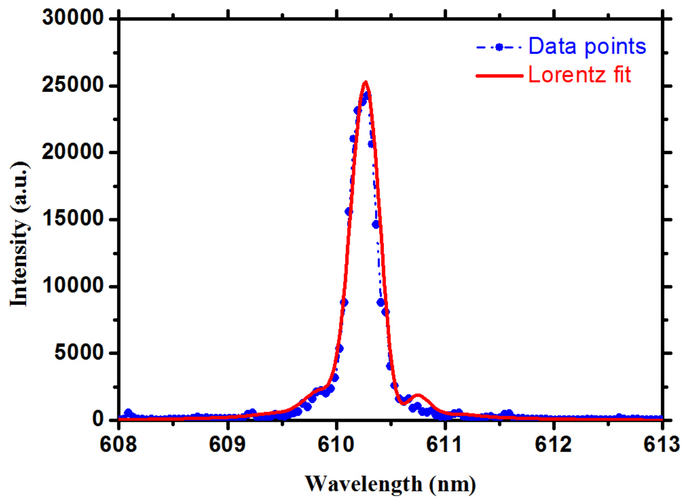

Figure 4.5: A typical Lorentzian fit at 300 ns in FA in vacuum.

increase in temperature may result in more ionization and therefore, increase in density is expected. [153] On the other hand recombination processes are likely to dominate at higher pressure and hence decrease in the density. [153]

As we have discussed in chapter 2 for applying this density calculation, plasma should be in local thermal equilibrium. To ensure, whether Local Thermal Equilibrium (LTE) condition is followed, we examined the validity of the McWhirter criteria defined by eqn. 4.3 for the present plasma condition. [105]

$$n_e \geq 1.4 \times 10^{14} T_e^{\frac{1}{2}} (\Delta E)^3 \quad cm^{-3} \tag{4.3}$$

Where, T_e (eV) is the electron temperature and ΔE (eV) is the energy gap between two states of the shorter wavelength i.e. Li I 610.3 nm of our discussion. In our experiments for the maximum electron temperature of ∼1.76 eV and for the largest energy gap (2.031 eV) of the selected transition (Li I 610.3 nm) this criteria predicts a lower limit of $n_e = 2.95 \times 10^{15}$ cm^{-3}. Estimated densities in the present case (Fig. 4.6) are always higher than this value and hence validate the LTE condition.

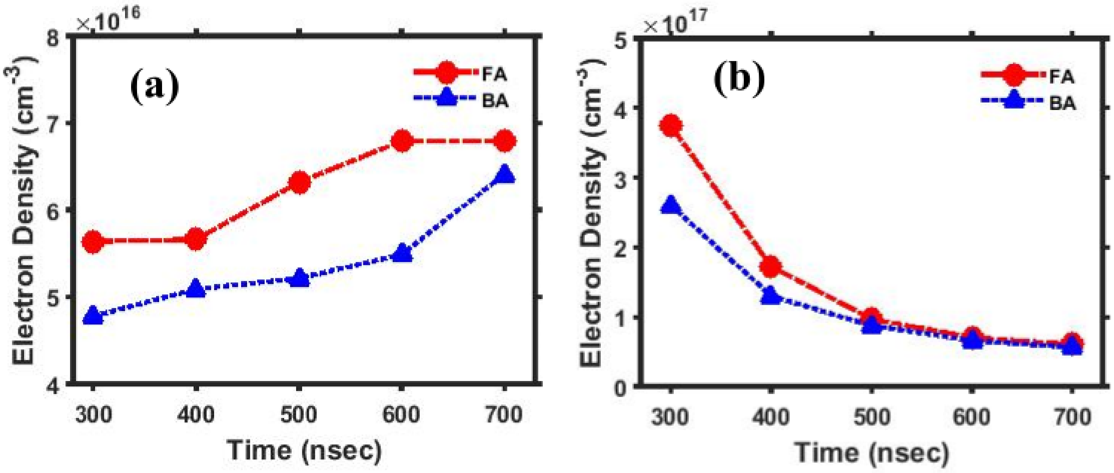

Figure 4.6: Electron densities in two geometries (i.e. FA and BA) and in (a) vacuum and (b) 2×10^{-1} mbar pressures.

4.3.2 Composition analysis

4.3.2.1 Ion/neutral (Ni/N):

Ion to neutral ratios for both FA and BA are estimated from NIST LIBS database. [135] From NIST LIBS the ion/neutral abundance can be estimated by entering electron temperature and density values. This calculation is based on Saha equation as given in Eq. 6.6.

$$\frac{n_i}{n_n} \approx 2.4 \times 10^{21} \frac{T^{3/2}}{n_i} e^{-U_i}/k_\beta T \tag{4.4}$$

Where, n_i and n_n are the density of ions and neutrals, respectively. T is the plasma gas temperature in kelvin, K_β is Boltzmann constant and U_i is ionization potential of the element (i.e. lithium in the present case).

Fig. 4.7 represents ion to neutral ratio in case of FA as well as and BA geometries in vacuum condition. In both the cases the ratio slightly increases with time and then deceases and has values always greater than one. This signifies that the population of ions is always higher in both the geometries as compared to neutrals. However, in case of front ablation this ratio is nearly about 2-4 times higher compared to the plasma plume produced in back ablation. This reveals the higher abundance of ions in FA as compared to BA plumes. This can be expected as the

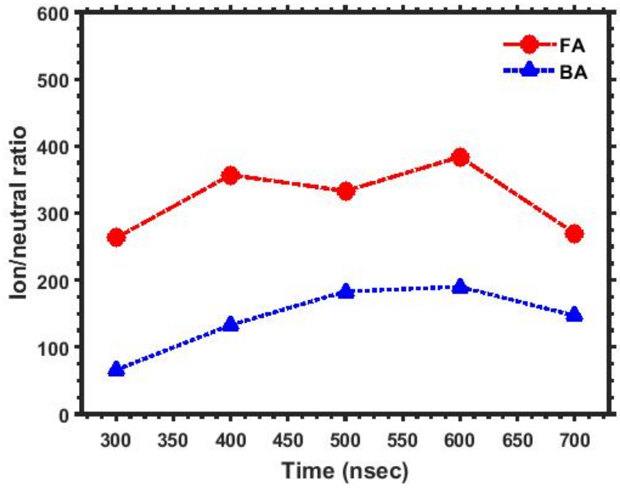

Figure 4.7: Temporal evolution of ion-neutral ratio in front and back ablation geometry in vacuum using NIST LIBS database. [135]

electron temperature is much higher in case of FA (Fig. 4.4) leading to increased ionization. [153]

For 2×10^{-1} mbar pressure again n_i/n_a is also always higher than one, which indicates that ions dominate in the plasma plume, at this pressure also. However, it decreases faster in case of FA as compared to BA. It can be noted that this decreasing trend with time is in confirmation with decrease in temperature, which again can be explained by the decrease in ionization. As mentioned earlier, the overall behaviour can be attributed to the combination of ionization and recombination processes.

4.3.2.2 Neutral abundance (N$_{FA}$/N$_{BA}$):

We have adopted two approaches to calculate neutral abundance in plasma produced in these two geometries. In the first case, we have used ADAS photon emissivity coefficients (PEC) to estimate the line intensity. [24] The intensity for a particular line can be given by the eqn. 4.5. [153]

$$I = F_{exp}(N_e N_a PEC_{excit} + N_e N_i PEC_{recom}) \tag{4.5}$$

Where PEC$_{excit}$ is photon emissivity coefficient (photon cm^{-3} s^{-1}) for electron

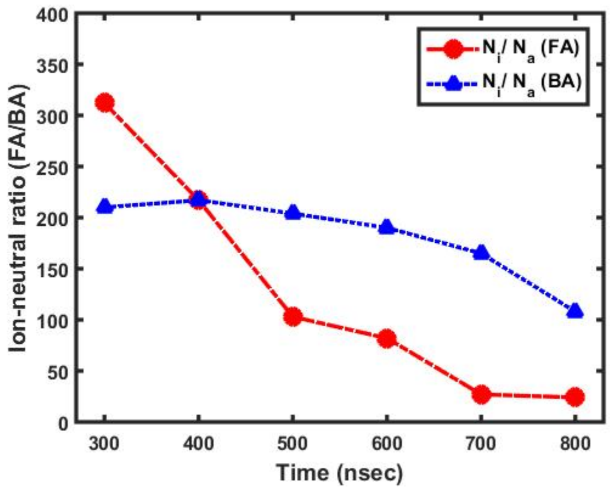

Figure 4.8: Temporal evolution of ion-neutral ratio in front and back ablation geometry at $2{\times}10^{-1}$ mbar using NIST LIBS database. [135]

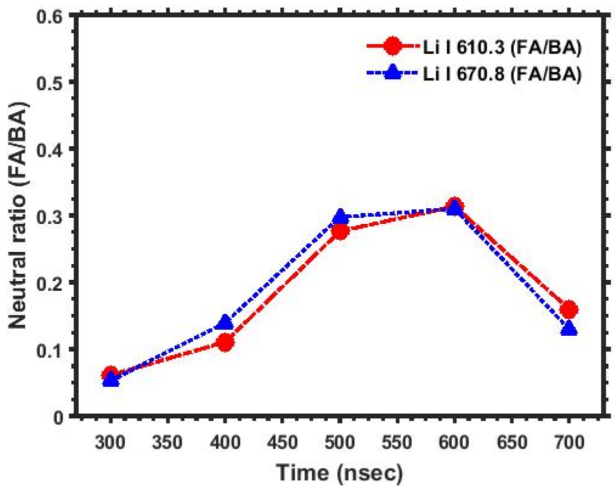

Figure 4.9: Temporal evolution of neutral ratios $(\frac{Na_{FA}}{Na_{BA}})$ in two geometries calculated from ADAS (Eq. 4.6) using two different lines Li I 610.3 nm and Li I 670.8 nm in vacuum.

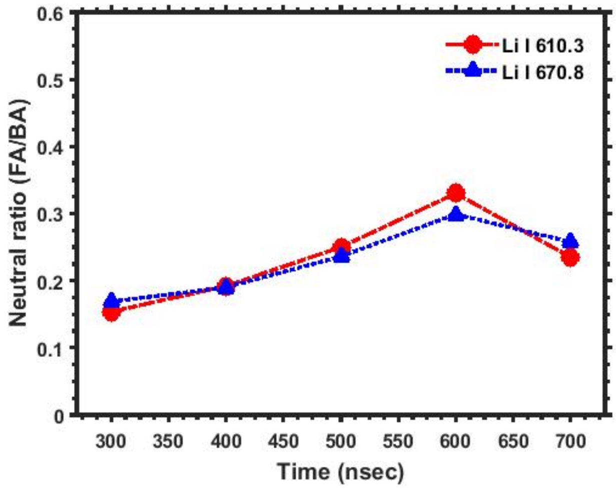

Figure 4.10: Temporal evolution of neutral ratio ($\frac{Na_{FA}}{Na_{BA}}$) in two geometries by considering LTE condition (Eq. 4.8) for two lines Li I 610.3 nm and Li I 670.8 nm in vacuum.

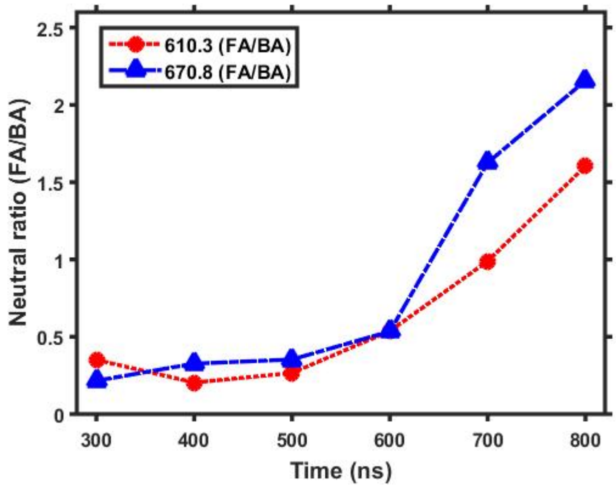

Figure 4.11: Neutral ratio ($\frac{Na_{FA}}{Na_{BA}}$) calculated in two different geometries (i.e. FA and BA) using ADAS (Eq. 4.6) for two lines Li I 610.3 nm and Li I 670.8 nm at $2{\times}10^{-1}$ mbar pressure.

impact excitation and PEC$_{recom}$ is photon emissivity coefficient for recombination (photon cm^{-3} s^{-1}). N_e, N_a and N_i are electron, neutral and ion densities respectively and F$_{exp}$ is the experimental factor.

As the experiments in both geometries are done in same environment and setup keeping all the experimental parameters identical, F$_{exp}$ has same value for both FA and BA case. Ratio of neutrals for forward to backward ablation (N_{FA}/N_{BA}) is estimated by using eqn. 4.6 which can be derived from eqn. 4.5.

$$\frac{I_{FA}}{I_{BA}} = \frac{N_e N_{FA} PEC_{excit} + N_e N_i PEC_{recom}}{N'_e N'_{BA} PEC'_{excit} + N'_e N'_i PEC'_{recom}} \tag{4.6}$$

Where N_e, N_{FA}, N_i, PEC$_{exc}$, PEC$_{recom}$, N'_e, N'_{BA}, N'_i, PEC'$_{excit}$ and PEC'$_{recom}$ represent electron density, neutral density, ion density, photon emissivity coefficients for excitation and photon emissivity coefficient for recombination in FA and BA geometries respectively. I_{FA} and I_{BA} represents the line intensity in FA and BA respectively. The values of (N_{FA}/N'_{BA}) for different times are shown in Fig. 4.9. It can be seen that the ratios calculated from both the lines match well within experimental uncertainties as well as ADAS limitations. As in ADAS, PECs are self-consistent and consider the particulars levels involved in the transitions, an estimate of neutral population appears reasonably well.

In the second approach considering local thermal equillibrium i.e. LTE conditions (as discussed earlier), the line intensity can be given by the eqn. 4.7 as given below. [154]

$$I = \frac{F_{exp} g_u h\nu A_{ul} N exp^{-E_u/k_\beta T}}{Z(T)} \tag{4.7}$$

In this equation, F_{exp} is experimental factor, g_u is statistical weight of upper level, h is Planck constant, ν is transition frequency, N is neutral density, A_{ul} is transition probabilities, E_u is upper level energy, k_β is Boltzmann constant, T is plasma temperature, Z is partition function. From this eqn. 4.7 the neutral abundance for FA and BA can be estimated by the following relationship as given in eqn. 4.8.

$$\frac{N_a}{N'_a} = \frac{\frac{I_{FA}}{I_{BA}} \times \frac{Z_{FA}}{Z_{BA}}}{exp[-\frac{E_u}{k_\beta T_{FA}} + \frac{E_u}{k_\beta T_{BA}}]} \tag{4.8}$$

Here, all the notations bear their standard meaning as mentioned earlier. We have calculated neutral ratios in FA and BA geometry using this relation and it is depicted in Fig. 4.10. It can be seen in this figure that more neutrals are produced in case of back ablation compared to front ablated plasma. To quantify neutral density for a comparative understanding, it is nearly 5 to 3 times than higher in BA than FA geometry.

Similar calculations, as mentioned above for 2×10^{-6} mbar, have also been done for 2×10^{-1} mbar pressure and are shown in the following Fig. 4.11 - 4.12. Figure 4.11 and 4.12 shows the neutral ratio calculated from eqn. 4.5 and 4.6, respectively. In this case the values obtained using Li I 610.3 and Li I 670.8 nm lines also match within experimental uncertainties. Further, both the calculations show consistency up to 800 ns within the experimental limit for these two lines (Li I 610.3 and Li I 670.8 nm). These two figures show the neutrals are less at initial time approximately up to 700 ns in FA plasma plume in comparison to BA one although at later times (i.e. $>$ 700 ns) the neutral density is higher in FA compared to BA case. Again, it can be attributed to the higher ionic contribution at initial stage in case of FA. However, with evolution of time neutral population increases probably because of overall increase in recombination processes at this pressure. It can be noted that under vacuum conditions neutral density is higher in case of BA as compared to FA within our observation time window. This can also be understood by the interplay of recombination/ionization processes.

Again we would like to emphasize that optically thin plasma conditions are met in the present experiment as neutral density is 1 - 2 orders smaller as compared to electron density. Further, this fact is also supported by the results where the neutral intensity ratios calculated from both Li I 610.3 nm and Li I 670.8 nm lines match well (Fig. 4.9 and 4.12) within experimental uncertainties.

Here, it can be mentioned that evolution of neutral abundance for BA and FA geometries depend on the respective ablation mechanisms as well as evolution of electron density and temperature which in turn will affect ionization recombination processes in the generation of neutrals.

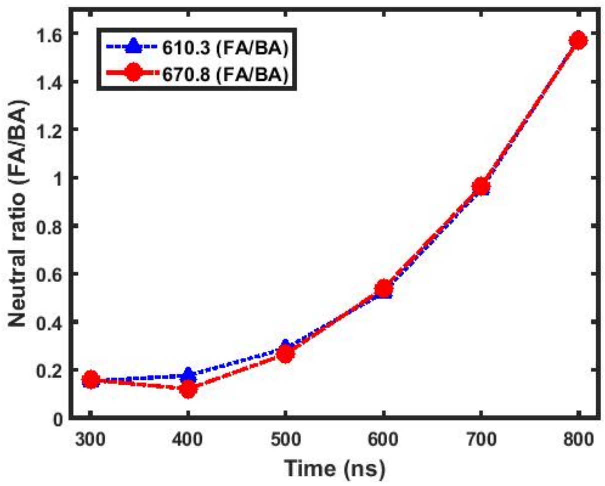

Figure 4.12: Neutral ratio in FA and BA by considering LTE condition (Eq. 4.8) at 2×10^{-1} mbar pressure.

4.4 Conclusion

In this chapter, compositional analysis of ions and neutrals in the evolving lithium plasma plume in FA and BA geometries in vacuum as well as at 2×10^{-1} mbar pressures has been attempted. Ion to neutral ratios are estimated from NIST (LIBS) and for estimating neutral abundance and ration in FA and BA geometries, two different approaches viz. Atomic Data and Analysis Structure (ADAS) analysis as well as integrated intensity ratio of Li I 670.1 nm and Li I 610.3 nm lines assuming LTE conditions are adopted. Two emission lines i.e. one resonance (Li I 670.1 nm) and other non-resonance (Li I 610.3 nm) are considered for estimating neutral abundance in these two cases. The findings of this study show that ions are dominant component in both geometries in terms of ion to neutral ratio and these can be seen in Fig. 4.7 and 4.8. But comparatively, the abundance of neutral particles are dominant in plasma plume produced in back ablation geometry as compared to front ablation. Analysis shows that neutrals gain with time in case of FA as time evolves at 2×10^{-1} mbar. In this work, an approach for the compositional analysis of evolving plasma in two different geometries has been attempted and described. We believe that present work will have interesting implications for future works regarding evolution of compositional analysis in various scenarios of laser induced plasma e.g. thin film deposition, neutral beam generation etc.

5

Spectroscopic investigation of stagnation region in laterally colliding plasmas

The properties of Laser Produced Plasma (LPP) depend on several parameters as has been discussed in the earlier chapters. In continuation of that, the effects of atomic mass of the target material on the formation, expansion dynamics and plasma parameters of colliding plasma have been discussed in this chapter. Special attention has been given to the characteristics of interaction zone which is formed, particularly, in case of colliding plasma. Depending on equally separated atomic mass difference carbon, aluminium and nickel have been chosen as target material for this investigation. Fast imaging and optical emission spectroscopy (OES) result show that dynamical, spectral and geometrical features of the induced interaction zone depend on the mass of the ablated species and spatial separation between the two interacting plumes. A sharp, intense and more directional interaction zone is formed by the interaction of heavier plume species (nickel) in comparison to that observed for lighter atomic mass (carbon) target.

5.1 Introduction

The importance of laser produced plasma and its application have been described in the previous chapters. Extensive theoretical and experimental studies related to this field have been reported under different experimental conditions. [114] Lateral collision of plasma plumes shows promising role in generation of energetic particles and formation of interaction region has attracted great interest in the recent years.

Two plasma plumes produced by spatially separated two laser beam having same parameters, propagate parallel to each other and they form an interaction zone in between them. Study of colliding plasma is interesting because of the unique features of induced interaction region and the underlying physics of colliding plasma. It has been investigated by several authors over a wide range of plasma parameters in the context of applications of laser ion source, thin film deposition, laser induced breakdown spectroscopy and inertial fusion confinement. [6, 8, 115, 117–120] Interaction between the plasma plumes produced by the ablation of solid targets, metal foils, thin films and laser-blow-off (LBO) of thin film has been studied over a wide range of laser intensities ($\sim 10^9 - 10^{14}$ W/cm^2) and for different collision geometries (e.g., head on, with angle and lateral collision etc.). [57, 58, 121, 123–126] Effects of spatial separations between two lasers, generation of plasma species with high kinetic energy, dynamics of cross beam polarization, space charge separation and dependence of atomic mass (Z) have been reported by several authors. [6,17,59,61–63] Target geometry as well as composition have been found to affect the stagnation region considerably. [64] Pulsed laser cross beam laser induced plasma was studied in case of two graphite targets and was found that collisional effects are responsible for the observed behaviour. [65] The formation and expansion of interaction zone in colliding plasmas is highly dependent on the geometrical shape, divergence of the interacting plume and energy of the ablating laser. However, in spite of these works on the formation and dynamics of interaction zone, not much attention has been given to the role of the atomic mass of the target material. Therefore, an experimental investigation of stagnation region in colliding plasma has been done by using fast imaging and spectroscopic technique and discussed in this chapter. Dependence of ablating target material and plasma plume separation has been considered also. Role of ionization and recombination processes has been evoked to explain salient temporal spectral features.

5.2 Experimental scheme

A complete description of the experimental schemes is given in chapter 2 and here it is discussed briefly. Figure 5.1 represents the schematic diagram of the experimental set up for this study. An Nd:YAG laser (λ = 1064 nm, pulse width

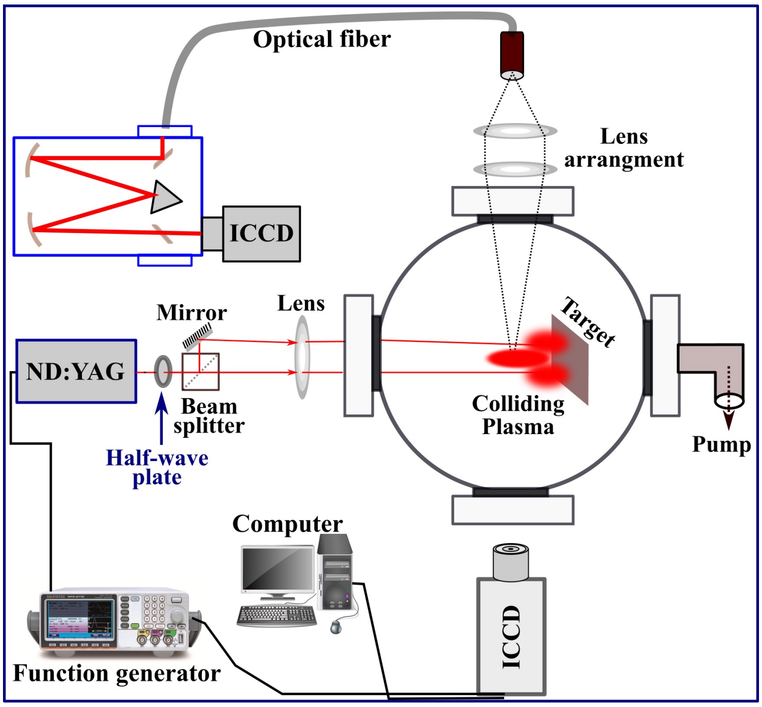

Figure 5.1: Schematic diagram of experimental set up.

$\sim$8 ns, full-width at half-maximum) has been used for producing plasma of solid target materials. Carbon, aluminium and nickel are considered, based on their mass difference, as target materials for this investigation. The incoming laser beam from the source is split into two using a bi-prism and focused by a plano-convex lens, having focal length of 35 cm, on the target surface. Experiment is done in vacuum (i.e. 5×10^{-7} mbar). Carbon, aluminium and nickel solid plates of dimension $60 \times 20 \times 1$ mm^3 have been used. The target plates are placed inside a stainless steel vacuum chamber by using a vacuum compatible feed-through holding arrangement. The target positions are changed by 2 mm to a fresh surface after each consecutive 5 shots by using the linear scale on the feed-through. The experiment is done with single mode and the desired fluence at the target surface is achieved by putting a half wave plate before the beam splitter. The separation between the two beams was adjusted by changing the reflecting angle of the mirror. The spot sizes of both the beams were set as 1 mm and beam separation was set as 2, 4 and 6 mm respectively.

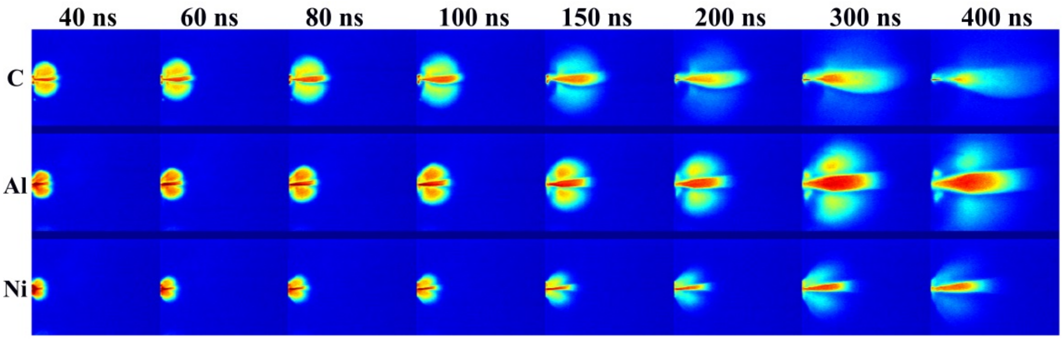

Figure 5.2: Sequence of laser produced colliding plasma plume images of solid carbon, aluminium and nickel target at 2 mm beam separation in vacuum (5×10^{-7} mbar).

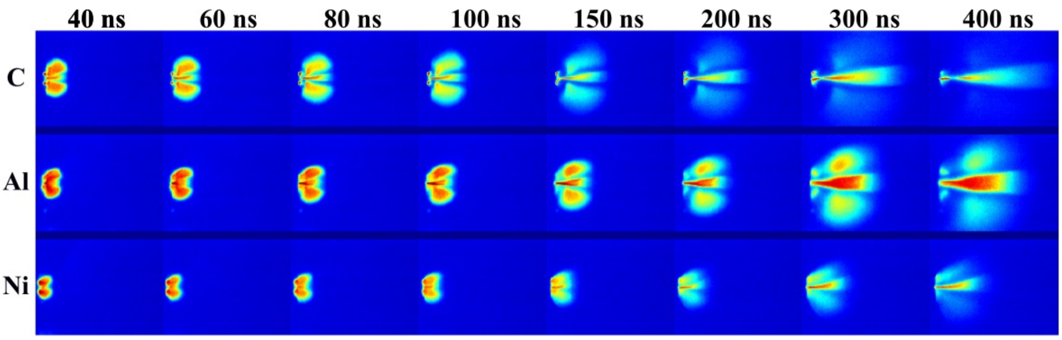

Figure 5.3: Sequence of laser produced colliding plasma plume images of solid carbon, aluminium and nickel target at 4 mm beam separation in vacuum.

5.3 Results and discussion

The evolution of two dimensional images of interacting plumes formed by carbon, aluminium and nickel targets are recorded by ICCD camera for three different spatial separations 2, 4 and 6 mm as shown in Fig. 5.2, 5.3 and 5.4, respectively. It shows the sequence of images of laterally colliding plasma plumes at different time delays varying from 40 to 400 ns and at 2×10^{-6} mbar ambient pressure. Each image shown in these figures represents the spectrally integrated emission intensity in the range of 350 - 750 nm emitted from different plume species. The spot size of 1 mm and laser fluence 12.7 J/cm^2, respectively, are set at the target surface for both the laser beams that produce seed plasma plume and identical experimental

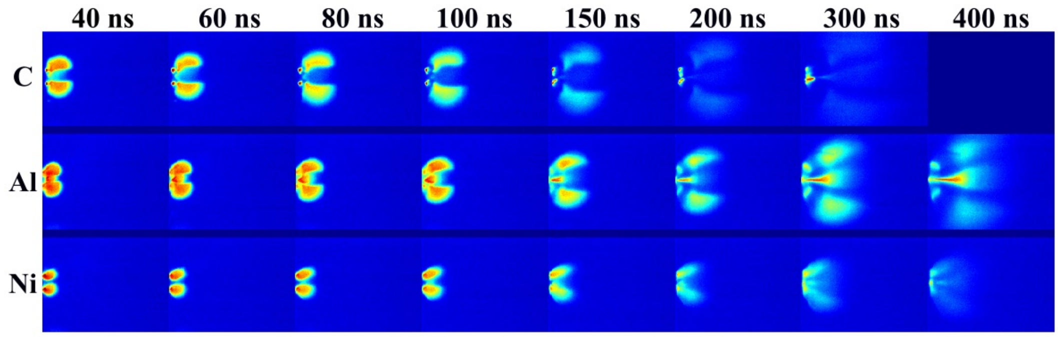

Figure 5.4: Sequence of laser produced colliding plasma plume images of solid carbon, aluminium and nicke target at 6 mm beam separation in vacuum.

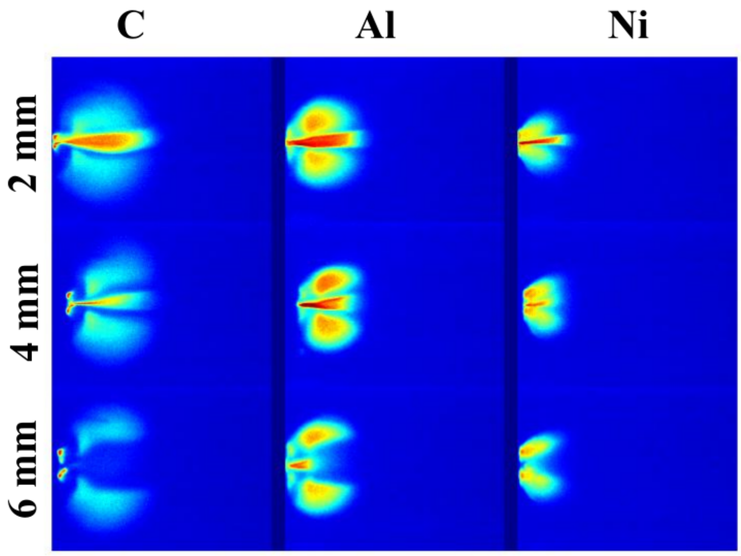

Figure 5.5: A comparative illustration of colliding plasma plume at 150 ns delay time of carbon, aluminium and nickel target at 2, 4 and 6 mm spot separation respectively in vacuum.

conditions are ensured for all the target materials. As is evident from Fig. 5.2, 5.3 and 5.4, the intensity of seed plasma plume decreases gradually with time for all the targets. In case of carbon, emission intensity is beyond the detection limit of the camera for t > 400 ns. However, emission of seeds plume formed by aluminium and nickel persists up to 800 ns. Plume expansion in vacuum can be treated as adiabatic expansion, where expansion occurs under the influence of pressure gradient and electron temperature and density decrease with time. [7,131]

A well defined stagnation layer in between the seed plumes is visible in all the cases but its geometry, intensity and expansion velocity are highly dependent on the properties of target material and separation between the two interacting plumes. Momentum transfer from the interacting seed species govern the formation and expansion of the stagnation region. General observation reveals that smaller separation between seed plumes lead to better formation of the interaction zone. On increasing the separation between the seed plumes, initiation time of interaction zone increases accordingly. At initial times, interaction zone is confined within the seed region. However, as the time evolves, interaction zone emerges out of the seed region. At plume separation of 2 mm, a fully developed stagnation region is visible from the lowest considered time delay (i.e. 40 ns) in all the target materials. In case of carbon, the stagnation region is broader in size and moves with higher velocity in comparison to aluminium and nickel where the stagnation regions are sharper and intense. Atomic mass dependence of target on the formation of stagnation region is clearly visible for larger spatial separations between the seed plumes. Figure 5.2 - 5.5 clearly show that smaller atomic mass target, which is expected to have larger expansion velocity initiates the stagnation region at earlier times of plume expansion in comparison to the case of higher atomic mass. For carbon at 4 mm spatial separation, a well developed stagnation region is visible at $\sim$ 40 ns, whereas in case of aluminium and nickel it appears at $\sim$ 60 ns and $\sim$ 80 ns respectively. With further increase in spatial separation to 6 mm, stagnation region in the case of carbon plasma is feeble in comparison to seed plasma and almost invisible for t > 150 ns. On the other hand in case of aluminium, a well separated stagnation region is observed at $\sim$ 150 ns whereas in case of nickel it appears at a significant delay time $\sim$ 300 ns. Another noticeable observation is that the stagnation region is sharper and intense closer to the target plate. Gradual broadening of stagnation region, with increasing the distance from the target, indicates decrease in stagnation strength. This effect is more prominent for higher spatial separations between the seed plumes. Further, at 2 and 4 mm spatial separations, expansion velocity of the stagnation region is higher in comparison to seed plasmas for all the targets, whereas at highest separation (i.e. 6 mm) the expansion rate of stagnation region and seed plasmas are almost comparable in the considered time range.

Effect of mass of the seed plume species and separation between the seed plume on the formation and expansion of the stagnation region is clearly depicted in Fig. 5.5, where the images for the C, Al and Ni at 150 ns are presented for all the three spatial separations. For a fixed time delay and spatial separation, broader interaction region is observed in case of carbon and it become sharper and intense with increasing the mass of the ablating targets. This could be understood as follows. The expanding plasma plume species have characteristic angular distributions. In a parallel propagating plasma plumes, energetic plume species are transported to the interaction zone with its own kinetic energy and interact with counter propagating species from the other plume. The strength of interaction and subsequent stagnation is defined in terms of the collisionality parameter as given in eqn. 5.1 and 5.2. [127]

$$\zeta = D/\lambda_{ii} \tag{5.1}$$

$$\lambda_{ii} = \frac{m_i^2 v_{12}^4}{4\pi e^4 Z^4 n_i ln\Lambda_{12}} \tag{5.2}$$

In this equation ζ represents the collisionality parameter, D denotes the separation between two plasma plumes, λ_{ii} is ion-ion collision frequency, n_i is ion density and Z is ionization level. In standard definition $\zeta < 1$ stands for interpenetration of plasma and $\zeta > 1$ is termed as collisional stagnation. With the present experimental parameters at 4 mm separation, the estimated collisionality parameters for carbon, aluminium and nickel come out to be 13.4, 18.3 and 24.4 respectively. The higher value of collisionality parameter suggests that the plume species suffer more collisions and stagnate in smaller region in comparison to the case of low collisionality parameter. This is in line with our experimental observation which shows that nickel has a sharp stagnation region in comparison to carbon and aluminium. It can be mentioned here that in Ref. [17] inter-penetration was observed

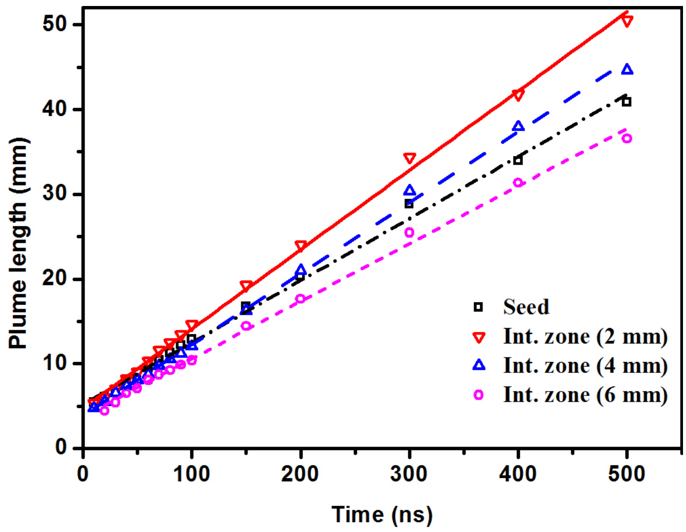

Figure 5.6: Axial length of plume expansion vs time delay of seed and interaction zones of aluminium plasma at 2, 4 and 6 mm separation and two laser beam of equal energy (100 mJ each) in vacuum.

for targets having higher Z which is in contradiction with present observation. They have tentatively explained that higher Z ions because of their heavier mass are slower and hence the collision frequency is less. [17] In their experiment two orthogonal laser beams are used whereas in our case the seed plumes are parallel to each other. Inter-penetration or stagnation not only depends on the mass but also the relative plume speeds, geometry of interaction as well as the separation between seed plumes. Hence, the difference can be anticipated in our case.

Further, it has also been observed that interaction zone is sharply pointed near the target surface and flattened towards the front edge (away from the target surface). This could be correlated with the angle of the ejected species from the seed region travelling to the interaction region. The interaction region closer to the target surface is formed mainly from the particles which have higher ejection angles (with respect to axial direction) and hence have better stagnation in comparison to the interaction between larger axial velocity components. In case of interaction between species having large axial velocity component, significant amount of momentum transfer can contribute towards the axial expansion of the stagnation region.

In order to see the dynamics of seed plume as well as stagnation region and its dependence on spatial separation and mass of the ejected species, we have analysed the axial dimensions of seed plume and stagnation region as a function of time delay. Here, aluminium target is selected to demonstrate the effect of separation between the seed plumes on the expansion velocity of stagnation region because aluminium stagnation is more clear and has longer persistence for all spatial separations. Figure 5.6 shows the axial dimension of the stagnation region observed with aluminium target as a function of time delay for 2, 4 and 6 mm separation between seed plumes. For the comparison of dynamics of stagnation region with seed plume, the axial dimension of seed plume is also included in Fig. 5.6. A linear dependence of the dimensions of both the stagnation region and seed plume with time suggests free expansion. The slope of the best fit to the experimental data gives the average expansion velocity of stagnation region and seed plume. The estimated axial velocities of stagnation region for 2 and 4 mm spatial separation are 9.36×10^6 cm/sec and 8.37×10^6 cm/sec, respectively, which are larger than the seed plume velocity (i.e. 7.3×10^6 cm/sec). As already discussed, for smaller spatial separations, the stagnation region is formed mainly by the interaction of species having higher axial velocity components and hence, resultant momentum transfer is responsible for the increase in axial velocity of stagnation region. On the other hand for higher spatial positions, the plume species have higher ejection angles with little momentum transfer along expansion (perpendicular to the target surface) direction. This is reflected in our result where at 6 mm separation, the estimated velocity of stagnation region is 6.7×10^6 cm/sec, which is lower than the velocity of seed plume.

Further, the target dependence of the velocity of stagnation region is clearly seen in the variation of axial dimensions of the stagnation region measured at 4 mm axial separation as a function of time delay for the case of carbon, aluminium and nickel as shown in Fig. 5.7. It has been observed that the expansion speed of stagnation layer is higher for lighter seed species. The estimated expansion speeds of stagnation region for the case of carbon, aluminium and nickel are 1.16×10^7, 8.37×10^6 and 4.7×10^6 cm/sec, respectively.

In order to get more insight into seed and interaction region, optical emission spectroscopy has been employed to record the line emission in the seed plasma and interaction zone for 4 mm spatial separation. Emission spectra of aluminium and carbon plumes have been recorded by using an optical fiber of diameter 400 μm

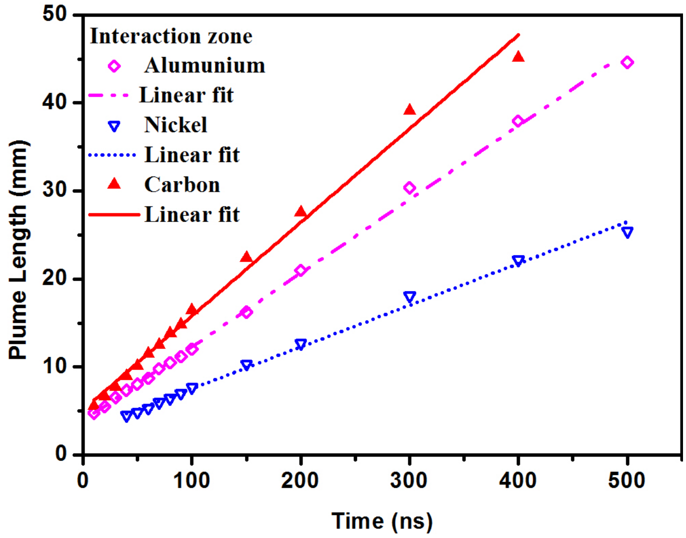

Figure 5.7: Axial length of interaction zone vs time delay of carbon, aluminium and nickel target at 4 mm separation and two beam of 100 mJ equal laser energy in vacuum.

at various time delays, up to 600 ns with respect to the ablating laser pulse. The tip of the fiber was positioned at 2 mm distance away from the ablating target surface for recording the spectra for both seed and stagnation regions. Prominent transitions from the ionic and neutral species i.e., Al I 394.4 nm ($3s^23p$ - $3s^24s$), Al II 466.3 nm ($1s^22s^22p^63s^23p^2$ - $1s^22s^22p^63s4p$), CII 426.7 nm ($1s^22s^23d$ - $1s^22s^24f$) and C I 657.8 nm ($2s^23p$ - $2s^23s$) are observed in aluminium and carbon plasmas, respectively. Temporal evolution of emission intensity profiles of Al II 466.3 nm and Al I 396.6 nm in both stagnation and seed regions is shown in Fig. 5.8. Similar plot for the carbon plasma i.e. variation of emission intensity profiles of C II 426.7 nm and C I 657.8 nm as a function of time is shown in Fig. 5.9.

The general trend of the temporal evolutions of emission intensity of various transitions in aluminium and carbon is almost similar. In the seed region, emission intensities of both ionic and neutral species are initially higher and decrease with time delay. However, in case of carbon, rate of decrease of emission intensity is much higher in comparison to aluminium plasma (Fig. 5.8 and Fig. 5.9). In contrast to this, at the interaction zone the emission intensity of ionic lines initially builds up and at later times goes on decreasing whereas the intensity of neutral

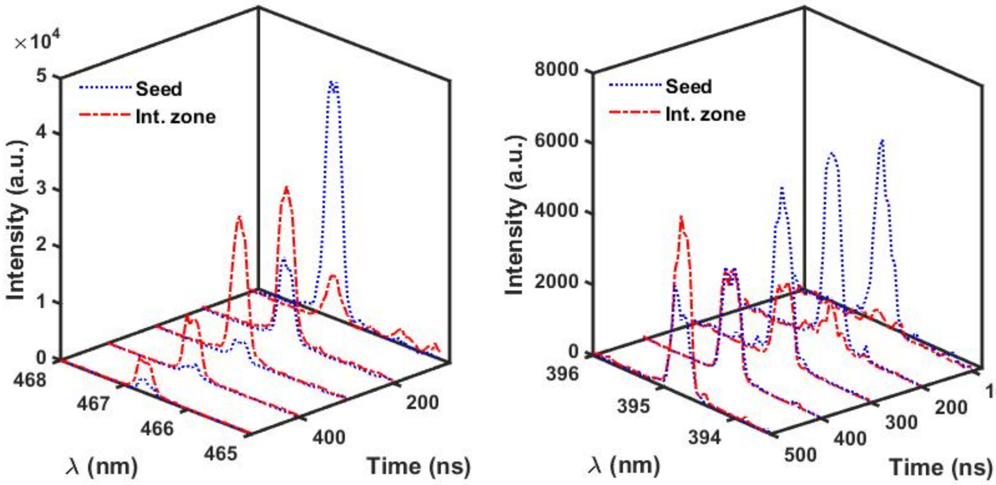

Figure 5.8: Temporal variation of Al II 466.3 (left) and Al I 394.4 nm (right) line emission intensity of both the seed and stagnation regions at 100 mJ energy in vacuum.

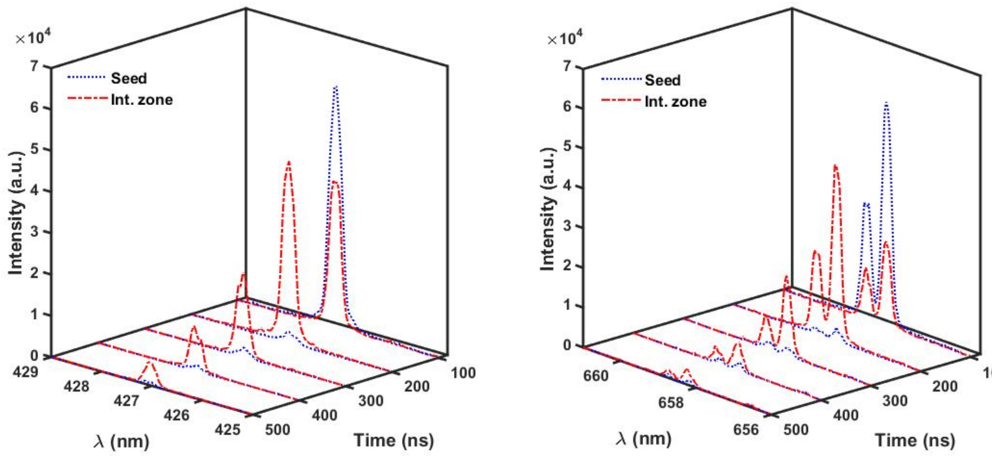

Figure 5.9: Temporal variation of C II 426.7 (left) and C I 657.8 nm (right) line emission intensity of both the seed and stagnation regions at 100 mJ energy in vacuum.

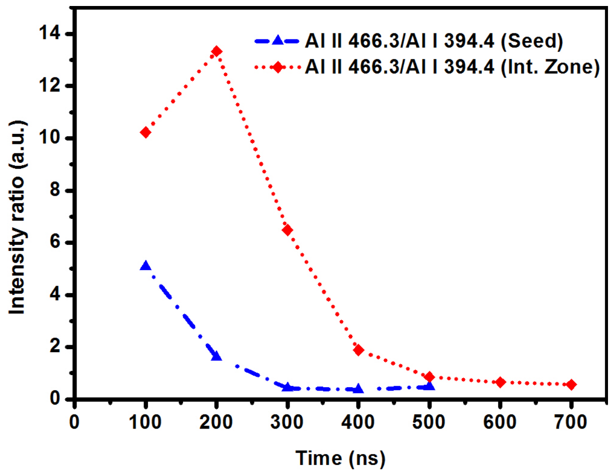

Figure 5.10: Ratio of ionic (Al II 466.3) to neutral (Al I 394.4) line emission intensity of aluminium for seed and interaction region in vacuum.

line grows up with the time. As will be discussed latter, this behaviour can be attributed to ionization/recombination processes in this case. The initial increase in the intensity of ionic lines can be attributed to increased ionization, whereas increase in neutral emission at later times can occur through recombination process.

It is interesting to see the temporal evolution of plume composition i.e. ionic to neutral ratio in both stagnation and seed regions. In order to avoid complexity, further analyses have been confined only for the case of aluminium targets. The representative ion to neutral emission can be seen by measuring the ratio of the integrated emission intensity of Al II 466.3 to Al I 394.4 nm. Figure 5.10 shows the ratio of Al II 466.3 nm to Al I 394.4 nm as a function of time delay for seed as well as stagnation region. It has been observed that for both the regions ionic to neutral emission ratio is always greater than one for the considered time range. This suggests that ionic species should be dominant in both the regions. In case of seed, ionic to neutral intensity ratio is highest at initial stages and decreases with increase of time delay. On the other hand, drastic enhancement in ionic intensity has been observed in stagnation region as compared to that observed for the seed region. However, specific ionic and neutral line ratio can not give the correct picture of plume composition in seed and interaction regions. Therefore, we have estimated ionic to neutral ratios theoretically for both the regions based on the NIST-LIBS data base. [135] Using the present plasma parameters the estimated

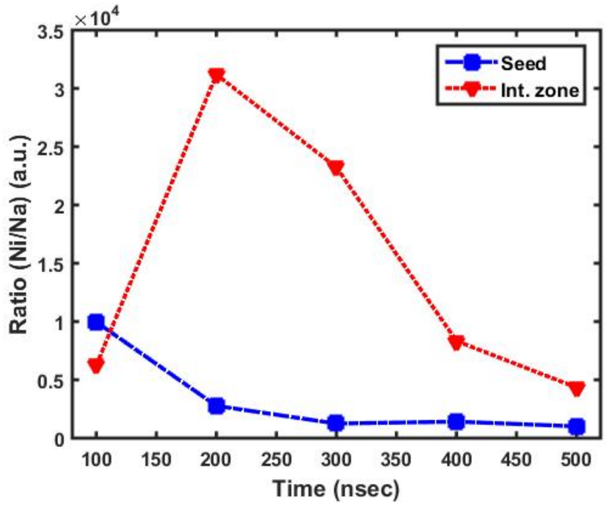

Figure 5.11: Ion neutral ratio of aluminium for both the seed and interaction regions using NIST data in vacuum.

Al II to Al I ratios are shown in the Fig. 5.11. It has been observed that estimated ionic to neutral ratios follow the similar trend as in the case of experimentally observed variation of Al II 466.3 to Al I 394.4 nm ratios. The atomic processes that are responsible for the observed spectral features will be discussed latter.

In view of the large enhancement of emission intensity of ionic species in stagnation layer, it is interesting to see the variation of plasma parameters in stagnation region with respect to seed plasma. Stark broadening of the emission lines has been used to estimate the plasma electron density (n_e), while Boltzmann relation (intensity ratio of two lines) has been used to estimate the electron temperature (T_e) for both the seed and interaction zones. Electron density and temperature calculation methods and related equations are given in eqn. 2.2 and 2.1 in chapter 2. The Stark broadening of emission line in plasma is attributed to the Coulomb interaction of electrons and ions. Here, ionic contribution to the line broadening is ignored because it is very small for the temperature of present experiments. We have used the value of ω which is required for this calculation from reference 26. The estimated electron densities for different delay times are shown in Fig. 5.13. [129] Local Thermal Equilibrium (LTE) conditions has been verified in this case also by using the McWhirter criteria which states that the minimum value of electron density should follow the equation, [105]

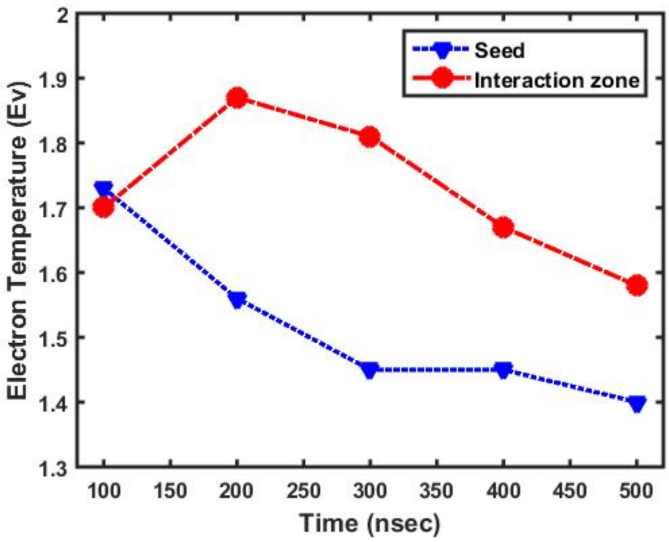

Figure 5.12: Temporal variation of electron temperature of aluminium seed and interaction zone in vacuum.

$$n_e \geq 1.4 \times 10^{14} T_e^{\frac{1}{2}} (\Delta E)^3 \quad cm^{-3} \tag{5.3}$$

Where, T_e (eV) is electron temperature and ΔE (eV) the the energy gap for the transition corresponding to the shorter wavelength line (466.3 nm). In this case electron densities are higher than the density 3.4×10^{15} cm^{-3} calculated from McWhirter criteria.

The electron temperature of plasma in LTE approximation is obtained by substituting emission intensities of Al II 466.3 and 559.3 nm of aluminium lines into the Boltzmann equation written in eqn. 2.1 of chapter 2. The difference between the higher energy levels of these two aluminium lines is 2.22 eV and the maximum electron temperature obtained in this case is 1.87 eV.

Figure 5.12 and Fig. 5.13 show the temporal variations of electron temperature (T_e) and electron density (n_e) for the representative aluminium target for both seed and interaction zones. It is clearly observed that the electron temperature in the seed region gradually decreases with time. The maximum electron temperature of seed region is $\sim$ 1.73 eV at 100 ns time delay. On the other hand in the interaction region, the temperature initially increases upto 200 ns (1.87 eV), which is slightly

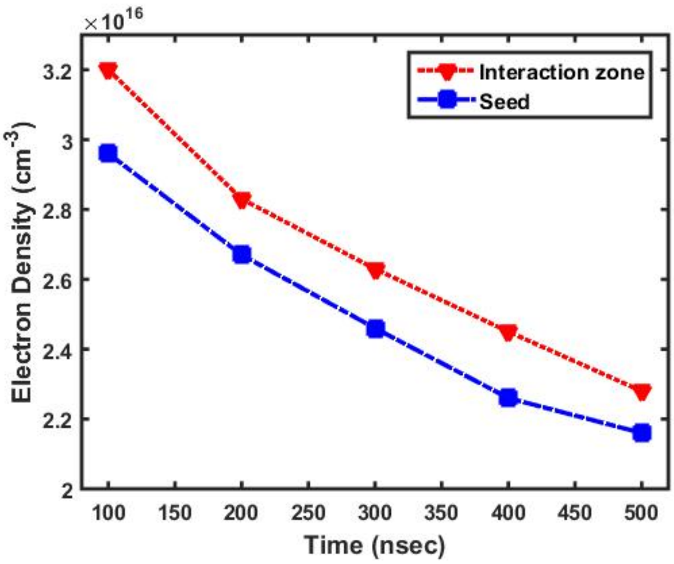

Figure 5.13: Temporal variation of electron density of aluminium seed and interaction zone in vacuum.

higher as compared to seed region and finally it also starts decreasing. It can be be possible due to increased collisions at the initial time that may heat the plasma in interaction zone. In case of electron density, decreasing trend has been observed for the both seed and interaction regions. However, the electron density is always higher in the interaction region for the considered time range. The increase of electron density in interaction zone is obvious because the ejected species from both the seed plasmas interact and are confined in small stagnation area.

In order to understand the temporal behaviour of intensities of neutral and ionic lines, we attempted to estimate rate coefficients/rates for ionization, radiative recombination and tree body recombination processes. Ionization rate coefficient has been adopted from [33] and is given by eqn. 5.4. [134]

$$\kappa_{pi} = \frac{9.56 \times 10^{-6}(kT_e)^{-1.5} exp(-\epsilon_{pi})}{\epsilon_{pi}^{2.33} + 4.38\epsilon_{pi} + 1.32\epsilon_{pi}} \quad cm^3 \quad s^{-1} \tag{5.4}$$

In this equation p and i are principal quantum numbers of initial and ground states and $\epsilon_{pi} = E_{pi}/kT_e$ where kT_e is electron temperature in eV and E_{pi} is ionization potential.

Radiative and three body recombination rates are estimated by using the rela-

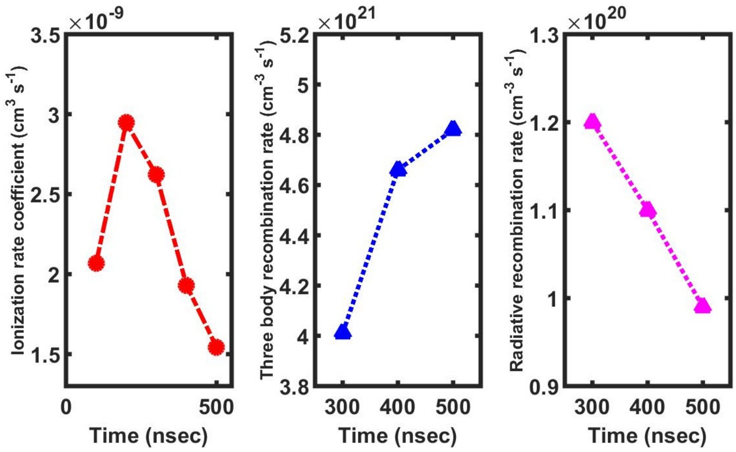

Figure 5.14: Ionization rate coefficient and three body and radiative recombination rate

tions given in eqn. 5.5 and 5.6. [133]

$$R_r = 2.7 \times 10^{-19} n_e n_i Z^2 T_e^{-3/4} \quad m^{-3}s^{-1} \tag{5.5}$$

$$R_{3b} = 9.2 \times 10^{-39} n_e^2 n_i Z^3 T_e^{-9/2} ln\sqrt{Z^2+1} \quad m^{-3}s^{-1} \tag{5.6}$$

The estimated values are shown in Fig. 5.14.

The ionization rate coefficient shows an increase initially, which decreases at later times. Three body recombination rate also shows an increase at later times, whereas radiative recombination does not exhibit increase. It can be inferred from the figure that the initial increase in the intensity of ionic Al (II) lines should be due to the increase in ionization process, whereas the decrease in Al (II) intensity coupled with increase in the intensity of neutral Al (I) lines at later times, which can be attributed to increased three body recombination process. In the present study we clearly found the evidence that ionization/recombination processes are responsible for the distinct emission features observed in the interaction zone. In short there were several studies on the formation of stagnation layer in colliding plasmas, however, most of them were concerned with plasma parameters in the interaction zone. Present study clearly brings out the mechanistic aspect of the enhanced emission in the interaction region.

5.4 Conclusion

In this chapter, a comparative study of dynamics and characteristics parameters of colliding plasma plumes and subsequently induced interaction region produced by laser ablation of carbon, aluminium, and nickel targets has been discussed. Time resolved two dimensional images reveal that the mass of the ablated species significantly affects the characteristics of interaction region in terms of their initiation time, expansion velocity, geometry, size and strength of stagnation. The formation of interaction region starts at earlier times for the target having lower atomic mass compared to the targets of higher atomic mass. It has been observed that interaction region is more luminous, confined, sharp and highly directional in the case of relatively high Z-material. Further, the axial velocities for smaller spatial separation are higher for the stagnation region than for the seed plume, while for largest considered separation (i.e. 6 mm in this case) it is lower than the velocity of seed plume. The spatial dependence of the velocity of interaction region is explained on the basis of angular distribution and resulting momentum transfer of the interacting plume species. Electron temperature and density are higher in the interaction region in comparison to seed region. Atomic analysis of emission lines is performed by estimating ionization rate coefficient, thee body and radiative recombination to understand the temporal variation of plasma parameters.

6

Interaction of laser produced plasma in the presence of external magnetic field

In this chapter, experimental investigation of laser produced colliding plasma in the presence of external magnetic field is presented. The strength of the magnetic field is varied from B = 0 to 4000 Gauss under vacuum, i.e. 5×10^{-7} mbar. Plasma temperature, density, ionization rate coefficient and line emission in the presence of magnetic field B are compared those with field free case. Laser produced plasma expands freely in vacuum, which is adiabatic by nature. The expansion dynamics and characteristic parameters of colliding plasma as well as interaction zone get modified significantly with the introduction of external magnetic field. In the presence of magnetic field emission from doubly ionized Al is significantly increased which is attributed to increased ionization due to Joule heating.

6.1 Introduction

Collision of plasma plumes is an important phenomenon in many laboratory plasma and applications such as plasma confinement, conversion of plume kinetic energy into thermal energy, LIBS, inertial confinement fusion (ICF), emission intensity enhancement, laboratory studies of plasma of astrophysical importance, Alfven wave study etc. [21, 67, 68, 79, 84, 85] Expansion of laser produced plasma in the presence of an external magnetic field is studied in many other experimental studies under different conditions. [21, 73, 80, 81, 86] Neogi et. al. studied laser produced carbon plasma expanding in vacuum, low pressure ambient gas and nonuniform magnetic field, and they observed oscillation of plume species which is attributed to edge instibility. [70, 71] Harilal et. al. reported slowing down of plasma expansion and enhancement of ionic emission with introduction of external magnetic field. [32] Behera et. al. observed oscillation of plasma plume in varying magnet with 2D fast photography and spectroscopic studies. [5] Joshi et. al. observed an initial increase in ion/neutral emission of lithium plasma in presence of a varying magnetic field. [74] Kumar et. al. reported the effect of transverse magnetic field on the dynamics of plasma plume and spectral emission of laser-blow-off plasma of a thin film in the presence of ambient gas. [75–77] More details has been given in literature survey in chapter 1. The important aspects of laser produced colliding plasma and the subsequent interaction zone has been discussed in chapter 5. Many novel features of colliding plasma with different target, laser parameters, ambient and ablation geometries have been reported by several authors. [6, 57, 61–65, 121, 123, 126] Al-Shboul et. al. studied the effect of different Z in cross-beam induced colliding plasma and found that high Z plasma interpenetrates where low Z stagnates. [17] Kumar et. al. reported colliding plasma of thin film target and observed neutral particles dominates in the interaction region. [58, 124, 125]

Plasma-plasma interaction in the presence of external magnetic field is an interesting phenomenon to study because of its implications from the understanding fundamental physics as well as applications. However, to the best of our knowledge, nobody has attempted a study regarding the colliding plasma in presence of an external magnetic field. It is important to understand the physics behind this type of collision and features of the subsequently produced interaction zone in presence of an external magnetic field. Therefore, in this work we tried to explore the colliding plasma phenomenon in the presence of an external varying magnetic field. The magnetic field is produced by a Helmholtz coil which is designed and fabricated, particularly for this purpose.

6.2 Experimental scheme

A schematic diagram of the experimental setup with an addition of a Helmholtz coil is shown in Fig. 6.1. Other part of this system is similar to the experimental setup shown in Fig. 5.1 and described in chapter 5. The Helmholtz coil can produce a

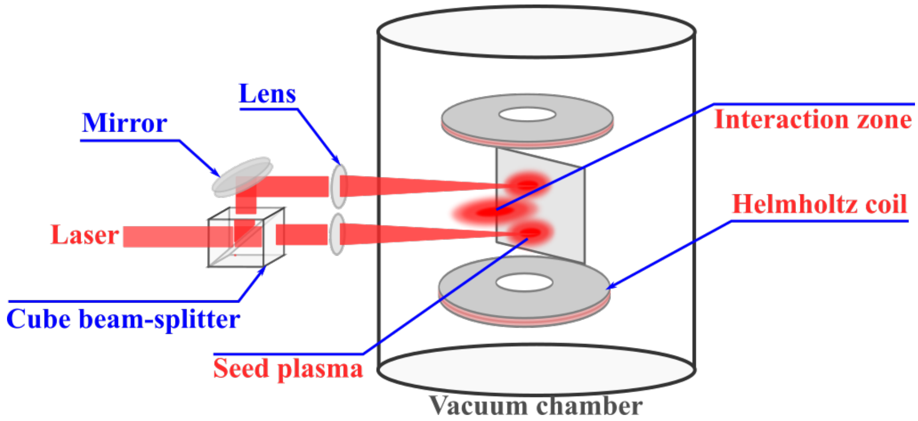

Figure 6.1: Schematic diagram of the colliding plasma in presence of magnetic field.

transverse magnetic field varying from 0 to 4000 Gauss. A detailed description of the Helmholtz coil is given in section 2.4 of chapter 2. The Helmholtz coil is placed inside the vacuum chamber and it is operated from outside without disturbing vacuum inside the chamber. Briefly, an Nd:YAG laser (λ = 1064 nm, pulse width $\sim$8 ns, full-width at half-maximum) has been used for producing plasma of solid aluminium target of dimension 6$\times$3$\times$1 cm^3. The incoming laser beam of 200 mJ energy from the source is split into two beam of 100 mJ each by using a cube beam splitter and focused by a plano-convex lens, having focal length of 35 cm, on the target surface. Experiment is done in vacuum i.e. 5×10^{-7} mbar. The target plate is placed inside a stainless steel vacuum chamber by using a vacuum compatible feed-through. The target positions are changed by 2 mm to a fresh surface after each consecutive 5 shots by using the linear scale on the feed-through. The experiment is done in single shot mode. The spot size and separation between the two beams were set as 1 mm and 4 mm, respectively. Magnetic field, ICCD camera, spectrograph and laser are synchronized by usage of a combination of function generator and delay generator.

6.3 Results and discussion

6.3.1 Fast imaging

An experimental investigation has been done on laser produced single plasma plume as well as colliding plasmas as described in the previous chapter, in two different ambient conditions. Expansion dynamics and characteristic parameters of both the single and colliding plasmas are studied in presence of an external magnetic field B ranging from 0 to 4000 Gauss. The results obtained from experimental studies in the presence of magnetic field are compared with field free case. All the studies are done with 100 mJ laser beam focused at 1 mm spot size on the target surface in vacuum i.e. 5×10^{-7} mbar ambient pressure. In case of colliding plasma two beams, each of 100 mJ, are focused at 4 mm spatial separation on the target surface with similar other conditions. Fast imaging and line emission spectroscopy data present interesting features, particularly in the presence of external field.

Figure 6.2 represents temporal evolution of laser produced single plasma plume in field free case and in the presence of magnetic field B = 1000 and 2600 Gauss. All the images in this figure and shown latter are line integrated image in wavelength range 350 to 700 nm. These are shown in matlab pseudo color jet(150), which is normalized to its maximum intensity. It can be seen from the figure that the expansion of plasma without external magnetic field is free and adiabatic. However, the introduction of magnetic field changes the normal behaviour of plasma expansion dynamics as well as characteristic parameters to a significant extent. Second and third row of Fig. 6.2 represent the temporal evolution of single plasma in 1000 and 2600 Gauss magnetic field, respectively. The major differences observed in this scenario are as follows. At initial delay time i.e. from 100 to 300 ns the axial expansion velocity i.e. velocity perpendicular to the target surface, increases and then decreases at later time delays. This phenomenon can be attributed to plasma oscillations due to diamagnetic effect. [21, 87] After 300 ns free expansion of the plasma plume in axial direction as observed in vacuum, is slowed down by the resistive force induced by external magnetic field, although all the other experimental parameters remain same including vacuum. On the other hand plasma plume doesn't experience any resistive force along the field direction and hence its expansion velocity component in transverse direction remains unaffected with

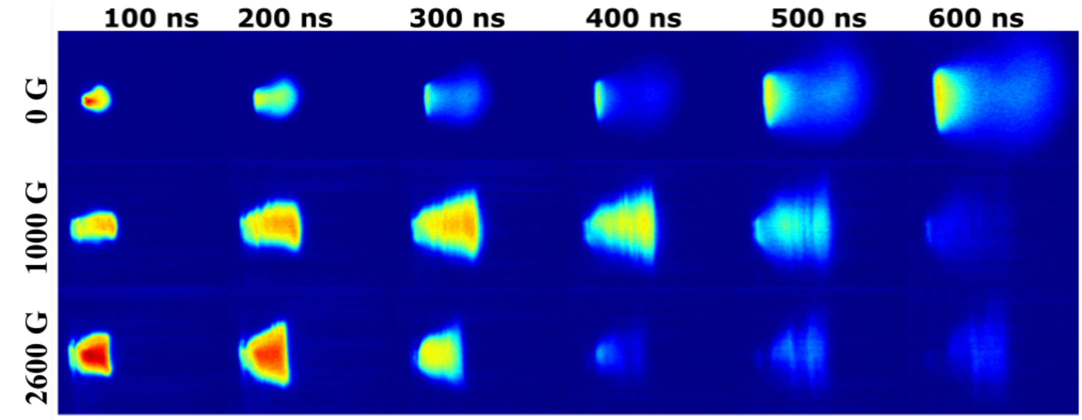

Figure 6.2: Temporal evolution of single plasma plume with and without presence of external magnetic field.

time. The shape of the plume, which is conical with a flat front, is significantly different from above images in field free case. Along with these, a well resolved striation can be seen in these images. This striation phenomenon is also reported phenomenon by many authors. [5, 21] Another important feature observed in this case is the increase of luminosity i.e. emission from the plasma plume in presence of magnetic field. This is also observed by line emission intensity enhancement of ionic lines which will be discussed latter. All the phenomena described above i.e. slowing down of axial expansion of plasma plume, increase in luminosity and confinement in the presence of magnetic field can be seen at bottom row of Fig. 6.2. The main objective of this chapter is to present dynamical and characteristic study of colliding plasma in the present of an external magnetic field. The results of single plasma plume are presented here to support the discussion in following paragraphs.

Figure 6.3 represents the time integrated images of colliding plasma with and without external magnetic field for time delay 100 to 1000 ns. The first, second and third row of this figure shows the snap shots of plasma plume at different delay times with B = 0, 1000 and 2600 Gauss, respectively. A well formed interaction zone can be seen without magnetic field in vacuum. Study of dynamical and characteristic parameters, and mechanism of interaction zone formation in different conditions are reported in several articles and we have given detailed discussion in the previous chapter 5. The shape, size, geometry of the colliding plasma and the subsequent interaction zone exhibit drastic changes with the introduction of magnetic field. However, no clear interaction zone is evident in the presence of magnetic field unlike the field free case. This can be understood in terms of collisionality parameter ζ given in eqn. 6.1. [127]

$$\zeta = D/\lambda_{ii} \tag{6.1}$$

Where, D is separation of two laser beams and

$$\lambda_{ii} = \frac{m_i^2 v_{12}^2}{4\pi e^4 Z^4 n_i ln\Lambda_{12}} \tag{6.2}$$

Here, m_i, v_{12}, Z, n_i and Λ_{12} are the ion mass, relative velocity of two plumes, ionization level, plasma density and Coulomb logarithm of the plasma. The value of ζ determines the nature of formation of interaction zone. The estimated collisionality parameters are $\zeta = 5$ and 10 for B = 0 and 1000 Gauss, respectively. These values predict soft stagnation for both the cases. However, in presence of magnetic field no clear stagnation is observed (Fig. 6.3). Collisionality parameter ζ given in eqn. 6.1 is derived for field free case. Therefore, this discrepancy may be due to the modified ion-ion mean free path (due to ion gyration) in the presence of magnetic field, which affects the value of collisionality parameter and it may not represent true picture of stagnation in this scenario. Expansion of the plasma plume in axial direction also slows down in presence of field and it increases in higher field which can be seen by comparing images at B = 1000 and 2600 Gauss. Normally the axial velocity of interaction zone becomes higher than the seed plasma. However, in presence of magnetic field axial velocity of the interaction zone is comparable with the seed expansion. Visual examination shows that optical emission from the plasma plume increases in the presence of field upto 800 ns delay time in both field (i.e. 1000 and 2600 Gauss) as compared to field free case. This is also confirmed by the spectral emission and electron temperature estimation in latter discussion. Though at higher field i.e. B = 2600 Gauss, it gradually decreases from 100 ns to 1000 ns delay time.

Figure 6.4 represents the images of colliding plasma at 400 and 800 ns for different B values, which shows dynamics of the colliding plasma and produced interaction zone with variation of B field. Images in this figure clearly show that the shape, size, emission and expansion dynamics are highly dependent on change

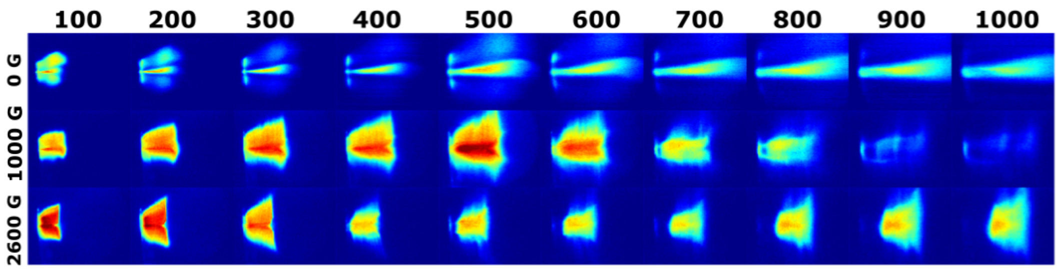

Figure 6.3: Temporal evolution of colliding plasma with and without presence of external magnetic field.

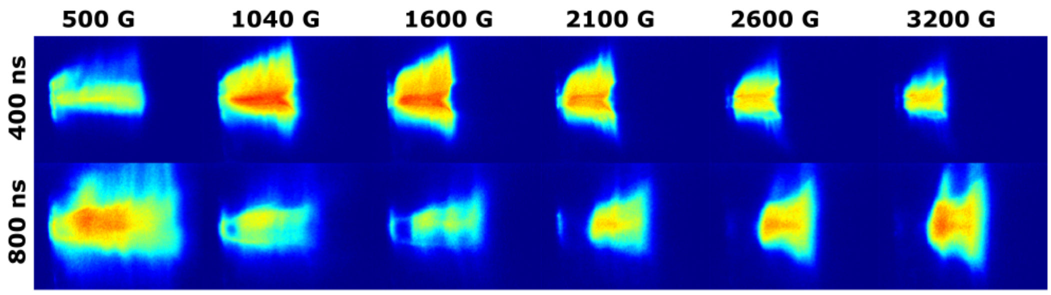

Figure 6.4: Images of colliding plasma plume at 400 and 800 ns with varying magnetic field from 500 to 3200 Gauss.

in B value as well as time.

6.3.2 Spectroscopy

Optical emission spectroscopy is used to investigate different plasma parameters such as, electron temperature and density, different atomic transitions occur in the plasma plume in different ambient. Figure 6.5 shows the intensity of characteristic lines Al II 466.3 and 559.3 nm with field B = 1000 Gauss and without field. A strong enhancement in intensity is observed for both the lines in presence of field as compared to the field free case. In field free case, intensity of Al^{+} lines start decreasing from its maximum value at 100 ns delay time. In contrast to this, intensity of Al^{2+} lines increases up to certain value at 300 ns delay time, as seen in Al II 466.3 nm and then starts decreasing with further time delays. The enhancement in the intensity of Al^{+} ions are probably because of the increased temperature due to Joule heating in external field. This is supported by increase

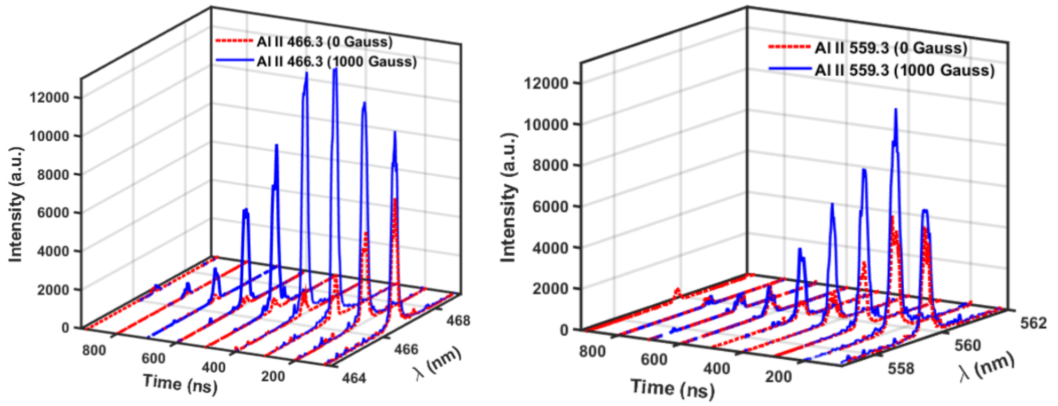

Figure 6.5: Temporal evolution of Al II 466.3 and Al II 559.3 nm with B = 0 and 1000 Gauss.

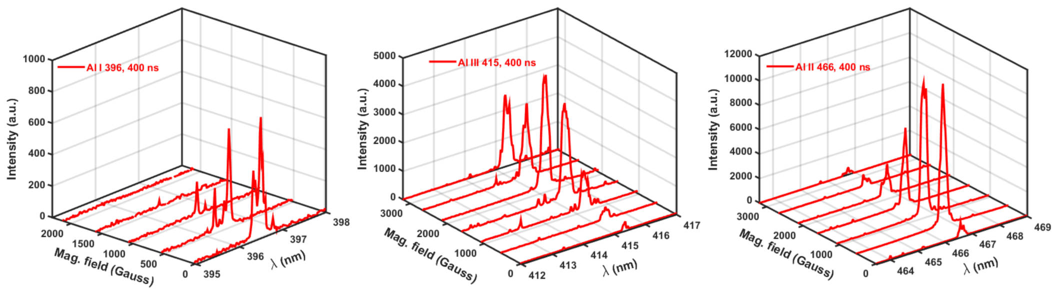

Figure 6.6: Evolution of Al I 396, Al II 466.3 and Al III 415 nm with varying magnetic field from B = 0 to 3200 Gauss in vacuum.

in ionization rate coefficient with introduction of magnetic field, which will be discussed latter. In the coming sections, we shall observe that the electron density is also increased after the introduction of magnetic field, which are in line with our explanation.

In similar way, Al I 396.15, Al II 466.3 and Al III 414.99 nm are shown with varying magnetic field ranging from B = 0 to 3200 Gauss at 400 ns delay time in vacuum. It is clear from the figure that the intensity of neutral line is very low and decreases rapidly with increase in magnetic field. Though, the intensity of Al^{+} line (i.e. 466.3 nm) initially enhances with the increase of field strength and it also decreases with further increase of field beyond 1000 Gauss. However, Al^{2+}

shows very interesting result, where it has the lowest intensity at B = 0 Gauss and increases continuously up to B ≈ 2500 Gauss. After that, it sustains with later time delays but having a slightly lower value as compared to its peak intensity within our observation limit. These can be attributed to the increase in plasma electron temperature because of Joule heating in the presence of magnetic field. Electron temperature has been estimated by using Boltzmann relation, as described in eqn. 6.3. [100] Discussion on Boltzmann relation can be found in chapter 2 in more detail. Boltzmann relation is as follows,

$$\frac{I_{ij}}{I_{kl}} = \frac{\nu_{ij} A_{ij} g_i}{\nu_{kl} A_{kl} g_k} exp \frac{-(E_i - E_k)}{k_\beta T_e} \tag{6.3}$$

In this relation, I is the line intensity of the transition between two energy levels, ν is the frequency of the line, A is Einstein's coefficient, g and E is statistical weight and energy of the particular energy level, k_β is Boltzmann constant, T_e is electron temperature, and the subscripts i, j, k and l denote different energy levels.

Temporal evolution of electron temperature of colliding plasma with and without B have been shown in Fig. 6.7. It can be seen that electron temperature increases initially up to 200 ns time delay. After that it decreases with further delay time in field free case. This type of phenomenon of colliding plasma has been discussed in the previous work described in chapter 5. However, the temporal evolution in presence of the external magnetic field, is of particular interest. The temporal profile of electron temperature (shown in Fig. 6.7) in presence of magnetic field can be divided in three steps. After increasing at initial time, it decreases rapidly and is nearly unchanged within the range of 300 to 500 ns delay time. Again, it decreases from 500 to 600 ns and repeat the previous equilibrium like condition. However, throughout this temporal evolution, the electron temperature is always higher in presence of magnetic field B as compared to it without field.

Furhter, the plasma electron density is determined from the Stark broadening of Al 466.3 nm line by using the eqn. 6.4 described below. [105, 106]

$$\Delta\lambda_{\frac{1}{2}} = 2\omega \frac{n_e}{10^{16}} \tag{6.4}$$

In this relation, $\Delta\lambda_{\frac{1}{2}}$, ω and n_e denote half wavelength at full maxima, electron impact parameter and electron density of the plasma. Local thermodynamic equi-

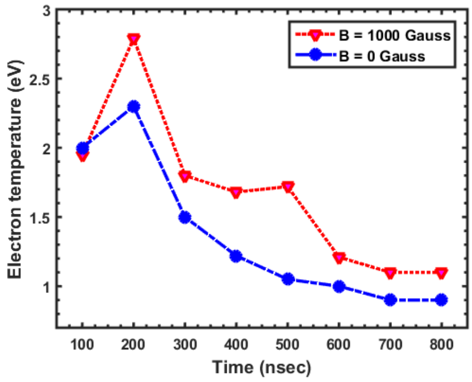

Figure 6.7: Temporal evolution of electron temperature of colliding plasma with field B = 1000 Gauss and without field.

librium (LTE) condition is also varified to validate this calculation by using the McWhirter criteria for the present plasma conditions. To fulfil minimum necessary criterion for LTE condition, plasma density should follow McWhirter relation as described below. [105]

$$n_e \geq 1.4 \times 10^{14} T_e^{\frac{1}{2}} (\Delta E)^3 \quad cm^{-3} \tag{6.5}$$

Here, n_e, T_e and ΔE represent plasma electron density, temperature and energy gap between two states of Al II 466.3 nm. Figure 6.8 shows that plasma electron density gradually decreases with time from its maximum value at 100 ns delay time without magnetic field. Density is higher in presence of magnetic field as compared to field free case for all the temporal delays. It has been discussed before that the plasma temperature increases with the introduction of magnetic field which will enhance the electron density as well. The decreasing rate of density is lower in presence of field as compared to the other case in our consideration, which can be understood by increased ionization.

To confirm the increase in ionic line intensity, electron temperature and density, we have calculated the ratio of Al^{2+} and Al^{+} lines and ionization rate coefficient. Ratio of Al^{2+} and Al^{+} ions has been calculated by using Saha relation described in eqn. 6.6 and it is shown in Fig. 6.9 for both the cases i.e. with and without field. The Saha equation is

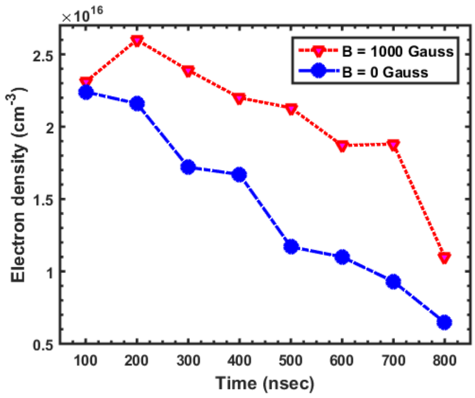

Figure 6.8: Density with B = 0 and 1000 Gauss.

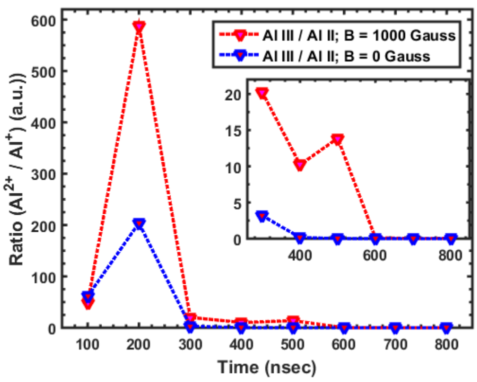

Figure 6.9: Temporal evolution of Al^{2+} and Al^{+} ratio calculated from Saha equation with B = 1000 Gauss and field free case.

$$\frac{n_i}{n_n} \approx 2.4 \times 10^{21} \frac{T^{3/2}}{n_i} e^{U_i/k_\beta T} \tag{6.6}$$

Here, n_i, n_n, T, U_i, k_β represents ion density, neutral density, plasma temperature in Kelvin, ionization potential of atoms and Boltzmann constant, respectively. Figure 6.9 shows and drastic increase in Al^{2+}. We will see that the ionization rate coefficient discussed latter also agrees with this.

Ionization rate coefficient of both Al^{+} and Al^{2+} lines with and without presence of the external field has been estimated from the eqn. 6.7 given below. [134]

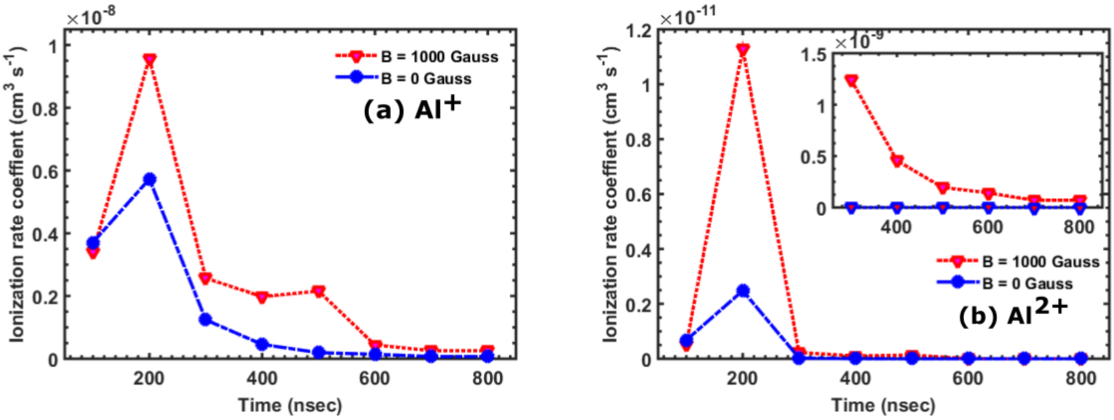

Figure 6.10: Temporal evolution of ionization rate coefficient for (a) Al^+ and (b) Al^{2+}.

$$\kappa_{pi} = \frac{9.56 \times 10^{-6}(kT_e)^{-1.5} exp(-\epsilon_{pi})}{\epsilon_{pi}^{2.33} + 4.38\epsilon_{pi} + 1.32\epsilon_{pi}} \quad cm^3 \quad s^{-1} \tag{6.7}$$

Here, $\epsilon_{pi} = E_{pi}/kT_e$ and T_e, E_{pi}, p, i represents electron temperature, ionization potential, principal quantum numbers of initial and ground state, respectively. Figure 6.10 shows the temporal evolution of ionization rate coefficient of colliding plasma at B = 0 and 1000 Gauss in vacuum. This figure shows initial increase in ionization rate coefficient for both Al^+ and Al^{2+} lines and then decreases with time. Further, it shows decrease from 200 to 300 ns delay time. After that, it decreases at slower rate with further delay time. However, the difference in this rate is clearly visible for both the lines and in ambient with B = 0 and 1000 Gauss.

To understand the behaviour of plasma dynamics in the presence of magnetic field, few parameters such as Larmor radii of electron and ion, plasma β, bubble radius (R_b) and magnetic field diffusion time (t_d) need to be estimated. Larmor radius is calculated from $mv_\perp/qB$, where m, $v_\perp$, q and B are the mass of the charged particle, particle velocity perpendicular to the magnetic field, charge of the particle and magnetic field, respectively. Estimated values for electron, Al^+ and Al^{2+} Larmor radii are 3 μm, 7 cm and 14 cm, respectively. The maximum plume length observed in image is roughly equal to 2 cm. This indicates that electrons are only magnetized species in this study and ions are not affected by field. In presence of magnetic field, plasma β governs the expansion dynamics of the plume. Different type of plasma β are discussed in chapter 1 in detail. Thermal beta (i.e. β_t = thermal pressure/magnetic pressure) of plasma is given by eqn. 6.8.

$$\beta_t = \frac{n_e T_e}{B^2/2\mu_o} \tag{6.8}$$

The expansion of the plasma plume transverse to the magnetic field will stop, when thermal beta will be equal to one i.e. thermal pressure of plasma will be equal to magnetic pressure. However, after β_t becomes ≈ 1, plasma does not stop and rather is slowed down. This is because, thermal beta is not the only governing parameter but the conversion of thermal energy into directed energy becomes important parameter. Directed beta (β_d) is given by eqn. 6.9.

$$\beta_d = \frac{m n_e v^2/2}{B^2/2\mu_o} \tag{6.9}$$

All terms used in eqn. 6.8 and 6.9 represents same meaning as discussed in chapter 2. The estimated value of thermal beta is around unity at 500 ns delay time in this study. However, slower expansion is observed even after this time delay, which can be attributed to the directed beta of the plasma. Another important parameter is bubble radius (R_b) which is described in eqn. 6.10 for a spherical plasma plume expanding in magnetic field.

$$R_b = \left(\frac{3\mu_o E_{lpp}}{2\pi B^2}\right)^{1/3} \tag{6.10}$$

Where, $\mu_o = 4\pi \times 10^7$ H/m, E_{lpp} is laser energy and B is the external magnetic field. The bubble radius, estimated from this equation, is 1.77 cm for B = 1000 Gauss, which is comparable to our plume dimension 2 cm as observed in images. The small difference observed in this case can be attributed to the assumption of spherical plasma plume, which is true for single plasma. In this study of colliding plasma the shape has been modified, which is observed from the images, slightly due to the interaction between two plumes. In diamagnetic limit magnetic field diffusion time (t_d) is described in eqn. 6.11

$$t_d = \frac{4\pi\sigma R_b^2}{c^2} \tag{6.11}$$

Where, σ is plasma conductivity which can be estimated from Spitzer formula.

[35] The diffusion time estimated for $R_b = 1.77$ cm and 2 eV temperature is 537 ns for Z = 2. After this time magnetic field fully penetrates into plasma. This fact is reflected in the increased emission of ionic lines (Fig. 6.5 and 6.6) at later times.

The results that have been discussed above are the preliminary findings of the experiments and the analysis presented here is qualitative in nature. Due to the presence of two plasma plumes and their interaction with the magnetic field a lot of different phenomena are involved and we expect many interesting results to follow once the thorough analyses are carried out.

6.4 Conclusion

The experimental investigation of dynamical expansion and characteristic parameters of colliding plasma in the presence of an external magnetic field is an important aspect in laser produced plasma studies, as any systematic study was not attempted before. It can be mentioned that the present study is an initiative in laser produced colliding plasma interaction in presence of an external magnetic field. Further, it can reveal several interesting phenomena in terms of physics as well as is important from application point of view in varying conditions. In this study, we found that geometry, expansion velocity and interaction between two laser produced plasma plume demonstrate different features in terms of expansion dynamics, geometry, ion/neutral composition, electron temperature, density etc. The conical shape, uniform and wider front surface area of colliding plasma in presence of B can be useful in laser deposition technique and other applications. Also an increase of Al^{2+} emission has been observed in the presence of the magnetic field as compared to field free case, which is attributed to Joule heating and subsequent increase in ionization.

7
Conclusions and future scopes

In this chapter, summary of the research work done in this thesis is mentioned in brief. The work done in this thesis leads to some new problems which can be attempted in future to advance the knowledge. The future scopes of this study is also discussed in this chapter.

7.1 Conclusion

In this thesis, experimental investigation of laser produced plasma in various configurations is reported. Different types of target materials, geometries and ambient are chosen to study the expansion dynamics and characteristics parameters of laser produced plasma plume. Focused beam of Nd:YAG laser (1064 nm, 8 ns pulse width, 850 mJ maximum energy) is used to ablate thin film (LiF-C) as well as solid targets (carbon, aluminium and nickel). The target is attached to a holding arrangement for changing target position, which is placed inside a vacuum chamber. Fast imaging and optical emission spectroscopy have been used as diagnostic tools to study the expansion dynamics, shape, size, geometry, characteristic emission, electron temperature and density of plasma plume produced by laser ablation.

In the first problem, dependency of laser produced plasma on different ablation geometries has been investigated. LiF-C thin film deposited on a quartz substrate which is transparent for the laser wavelength 1064 nm, is used to produce plasma in front ablation (FA) and back ablation (BA) geometries (discussed in chapter 2). Also, the effect of ambient pressure, laser spot size and deposited laser energy on expansion dynamics and characteristic parameters of the plume has been demonstrated. The comparative analysis of thin film plasma in two different geometries shows that plume parameters, e.g. kinetic energy, shape, size, composition and plasma temperature are significantly different in these two geometries. The plasma plume expands in spherical shape with higher velocity ($\sim 7.6 \times 10^6$ cm/sec) in case of front ablation geometry compared to cylindrical plume expanding with a relatively lower velocity ($\sim 1.36 \times 10^6$ cm/sec) in back ablation geometry in vacuum. Spot size affects the expansion velocity and shape of the plasma plume differently for front and back ablation geometries. In case of front ablation, expansion velocity of the spherical plume increases with smaller focal spot having same laser energy, whereas plasma plume is cylindrical in shape and expands with lower speed in back ablation geometry with similar conditions. This study will have implication in developing experimental technique (ablation geometry) for controlling the characteristic parameters and dynamics of expanding plasma in different applications according to the requirement.

Further, analysis of ion and neutral composition in the evolving lithium plasma plume in FA and BA geometries in vacuum as well as at 2×10^{-1} mbar pressures has been attempted. Ion to neutral ratios are estimated from NIST (LIBS) and for estimating neutral abundance and ration in FA and BA geometries, two different approaches viz. Atomic Data and Analysis Structure (ADAS) analysis as well as integrated intensity ratio of Li I 670.1 nm and Li I 610.3 nm lines assuming LTE conditions are adopted. Two emission lines i.e. one resonance (Li I 670.1 nm) and other non-resonance (Li I 610.3 nm) are considered for estimating neutral abundance in these two cases. The findings of this study show that ions are dominant in both the geometries in terms of ion to neutral ratio. Comparatively, neutral particles are dominant in plasma plume produced in back ablation geometry as compared to front ablation. Analysis shows that neutrals gain with time in case of FA as time evolves at 2×10^{-1} mbar. In this work, an approach for the compositional analysis of evolving plasma in two different geometries has been attempted and described. We believe that present work will have interesting implications for future works regarding evolution of compositional analysis in various scenarios of laser induced plasma e.g. thin film deposition, neutral beam generation etc.

The experimental investigation has been extended to the study of interaction between two plasma plumes, which is also called as colliding plasma, and the subsequent interaction zone. Effect of target atomic mass (Z) on the dynamics and characteristic plasma parameters of the interacting plasma plumes and subsequently induced interaction zone has been studied and compared for carbon, aluminium and nickel targets. Time resolved two dimensional images reveal that the mass of the ablated species significantly affects the characteristics of interaction zone in terms of their initiation time, expansion velocity, geometry, size and strength of stagnation. The formation of interaction region starts at earlier times for the target having lower atomic mass compared to the targets of higher atomic mass. It has been observed that interaction region is more luminous, confined, sharp and highly directional in the case of relatively high Z-material. Further, the axial velocities for smaller spatial separation are higher for the stagnation region than for the seed plume, while for largest considered separation (i.e. 6 mm in this study) it is lower than the velocity of seed plume. Electron temperature and density are also higher in the interaction region in comparison to seed region.

The experimental investigation of dynamical expansion and characteristic parameters of colliding plasma in presence of an external magnetic field is important addition to the knowledge of laser produced plasma, as it was not attempted before by anyone for a systematic study. It can reveal many other interesting phenomenon in terms of physics as well as application point of view in varying conditions. In this study, we found that geometry, characteristic parameters and expansion velocity plasma plume as well as interaction between two laser produced plasma demonstrate some interesting and different features when compared to field free case. The conical shape, uniform and wider front surface area of colliding plasma in presence of B can be useful in laser deposition technique and other applications. Also an increase in Al^{2+} has been observed in the presence magnetic field as compared to field free case.

7.2 Future scopes

The experimental investigations done in this thesis work brought out some interesting observations which lead to the open ended physics problems for future directions. Few of them are as follows.

1. There are large number of articles reporting expansion dynamics of the laser produced plasma plume in the presence of external transverse magnetic field.

However, limited articles reported on the laser produced plasma in axial magnetic field with its limitations. This will be a very interesting physics problem if one can attempt this.

2. Similarly, interaction of between plasma plumes can be a potential problem to study in presence of external magnetic field in axial direction.

3. Systematic study of the effect of ambient pressure in presence of magneitc field is another issues which needs to be explored.

4. Study of magnetic field effect on various aspects of colliding plasma will be another interesting theme of future work.

Bibliography

[1] Salvatore Amoruso, Riccardo Bruzzese, Nicola Spinelli, and R Velotta. *Journal of Physics B: Atomic, Molecular and Optical Physics*, 32(14):R131, 1999.

[2] S S Harilal, C V Bindhu, M S Tillack, F Najmabadi, and A C Gaeris. *Journal of Physics D: Applied Physics*, 35(22):2935, 2002.

[3] David B Geohegan and Alexander A Puretzky. *Applied Physics Letters*, 67(2):197–199, 1995.

[4] Salvatore Amoruso, Riccardo Bruzzese, Nicola Spinelli, Raffaele Velotta, Marco Vitiello, and Xuan Wang. *Physical Review B*, 67(22):224503, 2003.

[5] Narayan Behera, R K Singh, V Chaudhari, and Ajai Kumar. *Physics of Plasmas*, 24(3):033511, 2017.

[6] E Camps, L Escobar-Alarcón, E Haro-Poniatowski, and M Fernández-Guasti. *Applied surface science*, 197:239–245, 2002.

[7] Rajiv K Singh, O W Holland, and J Narayan. *Journal of applied physics*, 68(1):233–247, 1990.

[8] H Luna, Kevin D Kavanagh, and John T Costello. *Journal of applied physics*, 101(3):033302, 2007.

[9] Matthew Zepf, E L Clark, K Krushelnick, F N Beg, C Escoda, A E Dangor, M I K Santala, M Tatarakis, I F Watts, P A Norreys, et al. *Physics of Plasmas*, 8(5):2323–2330, 2001.

[10] A Pospieszczyk, F Aumayr, HL Bay, E Hintz, P Leismann, YT Lit, GG Ross, D Rusbüldt, RP Schorn, B Schweer, et al. *Journal of Nuclear Materials*, 162:574–581, 1989.

[11] F J Adrian, J Bohandy, B F Kim, An N Jette, and P Thompson. *Journal of Vacuum Science & Technology B: Microelectronics Processing and Phenomena*, 5(5):1490–1494, 1987.

[12] O Yavas, E L Maddocks, M R Papantonakis, and R F Haglund Jr. *Applied physics letters*, 71(10):1287–1289, 1997.

[13] V Schultze and M Wagner. *Applied Physics A*, 53(3):241–248, 1991.

[14] D Autrique, G Clair, D l'Hermite, V Alexiades, A Bogaerts, and B Rethfeld. *Journal of Applied Physics*, 114(2):023301, 2013.

[15] G C Tisone, K W Bieg, and P L Dreike. *Review of Scientific Instruments*, 61(1):562–564, 1990.

[16] O Rancu, P Renaudin, C Chenais-Popovics, H Kawagashi, JC Gauthier, M Dirksmöller, T Missalla, I Uschmann, E Förster, O Larroche, et al. *Physical review letters*, 75(21):3854, 1995.

[17] K F Al-Shboul, S S Harilal, S M Hassan, A Hassanein, J T Costello, T Yabuuchi, K A Tanaka, and Y Hirooka. *Physics of Plasmas*, 21(1):013502, 2014.

[18] Pramod K Pandey, Raj K Thareja, and John T Costello. *Physics of Plasmas*, 23(10):103516, 2016.

[19] J Dardis and J T Costello. *Spectrochimica Acta Part B: Atomic Spectroscopy*, 65(8):627–635, 2010.

[20] P W Rambo and J Denavit. *Physics of Plasmas*, 1(12):4050–4060, 1994.

[21] Narayan Behera, R K Singh, and Ajai Kumar. *Physics Letters A*, 379(37):2215–2220, 2015.

[22] Shigefumi Okada, Kohnosuke Sato, and Tadashi Sekiguchi. *Japanese Journal of Applied Physics*, 20(1):157, 1981.

[23] D K Bhadra. *The Physics of Fluids*, 11(1):234–239, 1968.

[24] H P Summer. Atomic data and analysis structure (version 2.6). *ADAS User Manual*, 204.

[25] Rajiv K Singh and J Narayan. *Physical review B*, 41(13):8843, 1990.

[26] Annemie Bogaerts, Zhaoyang Chen, Renaat Gijbels, and Akos Vertes. *Spectrochimica Acta Part B: Atomic Spectroscopy*, 58(11):1867–1893, 2003.

[27] Jagdish P Singh and Surya Narayan Thakur. *Laser-induced breakdown spectroscopy.* Elsevier, 2007.

[28] Yu P Raizer et al. *Physics of shock waves and high-temperature hydrodynamic phenomena*. Courier Corporation, 2002.

[29] Wanniarachchi K A Kumuduni, Yasushi Nakayama, Yoshiki Nakata, Tatsuo Okada, and Mitsuo Maeda. *Journal of applied physics*, 74(12):7510–7516, 1993.

[30] JCS Kools. *Journal of applied physics*, 74(10):6401–6406, 1993.

[31] Francis F Chen. *Introduction to plasma physics and controlled fusion*, volume 1. Springer, 1984.

[32] S S Harilal, M S Tillack, B OâĂŹshay, C V Bindhu, and F Najmabadi. *Physical Review E*, 69(2):026413, 2004.

[33] Guy Dimonte and L G Wiley. *Physical review letters*, 67(13):1755, 1991.

[34] M VanZeeland and W Gekelman. *Physics of Plasmas*, 11(1):320–323, 2004.

[35] David Book and J D Huba. Nrl plasma formulary. Technical report, NAVAL RESEARCH LAB WASHINGTON DC PLASMA PHYSICS DIV, 2002.

[36] R F Wood, K R Chen, J N Leboeuf, A A Puretzky, and D B Geohegan. *Physical Review Letters*, 79(8):1571, 1997.

[37] S S Harilal, C V Bindhu, M S Tillack, F Najmabadi, and A C Gaeris. *Journal of Physics D: Applied Physics*, 35(22):2935, 2002.

[38] Roger Kelly and Antonio Miotello. *Applied Surface Science*, 96:205–215, 1996.

[39] X Wang, S Amoruso, R Bruzzese, N Spinelli, A Tortora, R Velotta, C Ferdeghini, G Grassano, and W Ramadan. *Chemical physics letters*, 353(1-2):1–6, 2002.

[40] Hiroaki Nishikawa, Masaki Kanai, Gabor Szabo, and Tomoji Kawai. *Physical Review B*, 61(2):967, 2000.

[41] Howard M Smith and A F Turner. *Applied Optics*, 4(1):147–148, 1965.

[42] Salvatore Amoruso, Riccardo Bruzzese, and Xuan Wang. *Applied Physics Letters*, 95(25):251501, 2009.

[43] S Amoruso. *Applied Physics A*, 69(3):323–332, 1999.

[44] David B Geohegan and Alexander A Puretzky. *Applied surface science*, 96:131–138, 1996.

[45] David B Geohegan. *Applied physics letters*, 60(22):2732–2734, 1992.

[46] Douglas H Lowndes, DB Geohegan, AA Puretzky, DP Norton, and CM Rouleau. *Science*, 273(5277):898–903, 1996.

[47] RF Wood, JN Leboeuf, DB Geohegan, AA Puretzky, and Kuan-Ren Chen. *Physical Review B*, 58(3):1533, 1998.

[48] Sivanandan S Harilal, Nicole L LaHaye, and Mark C Phillips. *Optics Express*, 25(3):2312–2326, 2017.

[49] S S Harilal, C V Bindhu, M S Tillack, F Najmabadi, and A C Gaeris. *Journal of Applied Physics*, 93(5):2380–2388, 2003.

[50] Sivanandan S Harilal, Brian E Brumfield, and Mark C Phillips. An evaluation of equilibrium conditions and temperature-dependent speciation in a laser-produced air plasma. *Physics of Plasmas*, 25(8):083303, 2018.

[51] Sony George, Ajai Kumar, R K Singh, and V P N Nampoori. *Applied Physics Letters*, 94(14):141501, 2009.

[52] Sony George, Ajai Kumar, R K Singh, and V P N Nampoori. *Applied Physics A*, 98(4):901–908, 2010.

[53] Sony George, R K Singh, V P N Nampoori, and Ajai Kumar. *Physics Letters A*, 377(5):391–398, 2013.

[54] Th Wegner, B Geiger, F Kunkel, R Burhenn, T Schröder, C Biedermann, B Buttenschön, G Cseh, P Drews, O Grulke, et al. *Review of Scientific Instruments*, 89(7):073505, 2018.

[55] J Bohandy, B F Kim, and F J Adrian. *Journal of Applied Physics*, 60(4):1538–1539, 1986.

[56] Bhupesh Kumar, R K Singh, Sudip Sengupta, P K Kaw, and Ajai Kumar. *Physics of Plasmas*, 21(8):083510, 2014.

[57] Bhupesh Kumar, R K Singh, and Ajai Kumar. *Physics of Plasmas*, 20(8):083511, 2013.

[58] Bhupesh Kumar, R K Singh, Sudip Sengupta, P K Kaw, and Ajai Kumar. *Physics of Plasmas*, 21(8):083510, 2014.

[59] Po T Rumsby, J W M Paul, and M M Masoud. *Plasma Physics*, 16(10):969, 1974.

[60] P Yeates, C Fallon, E T Kennedy, and J T Costello. *Physics of Plasmas*, 20(9):093106, 2013.

[61] C Sánchez Aké, R Sanginés de Castro, H Sobral, and M Villagrán-Muniz. *Journal of applied physics*, 100(5):053305, 2006.

[62] Pádraig Hough, Conor McLoughlin, Sivanandan S Harilal, Jean-Paul Mosnier, and John T Costello. *Journal of Applied Physics*, 107(2):024904, 2010.

[63] Xingwen Li, Zefeng Yang, Jian Wu, Jiaxun Han, Wenfu Wei, Shenli Jia, and Aici Qiu. *Journal of Applied Physics*, 119(13):133301, 2016.

[64] J Dardis and J T Costello. *Spectrochimica Acta Part B: Atomic Spectroscopy*, 65(8):627–635, 2010.

[65] R Sanginés, C Sánchez Aké, H Sobral, and M Villagrán-Muniz. *Physics Letters A*, 367(4-5):351–355, 2007.

[66] R G Tuckfield and F Schwirzke. *Plasma physics*, 11(1):11, 1969.

[67] B H Ripin, E A McLean, C K Manka, C Pawley, J A Stamper, T A Peyser, A N Mostovych, J Grun, A B Hassam, and J Huba. *Physical review letters*, 59(20):2299, 1987.

[68] A N Mostovych, B H Ripin, and J A Stamper. *Physical review letters*, 62(24):2837, 1989.

[69] T A Peyser, C K Manka, B H Ripin, and G Ganguli. *Physics of Fluids B: Plasma Physics*, 4(8):2448–2458, 1992.

[70] A Neogi and R K Thareja. *Physics of Plasmas*, 6(1):365–371, 1999.

[71] A Neogi and R K Thareja. *Journal of applied physics*, 85(2):1131–1136, 1999.

[72] Virendra N Rai, Awadhesh K Rai, Fang-Yu Yueh, and Jagdish P Singh. *Applied optics*, 42(12):2085–2093, 2003.

[73] S S Harilal, B OâĂŹshay, Y Tao, and M S Tillack. *Applied Physics B*, 86(3):547–553, 2007.

[74] H C Joshi, Ajai Kumar, R K Singh, and V Prahlad. *Spectrochimica Acta Part B: Atomic Spectroscopy*, 65(5):415–419, 2010.

[75] Ajai Kumar, R K Singh, V Prahlad, and H C Joshi. *Laser and Particle Beams*, 28(1):121–127, 2010.

[76] Ajai Kumar, H C Joshi, V Prahlad, and R K Singh. *Physics Letters A*, 374(25):2555–2560, 2010.

[77] Ajai Kumar, R K Singh, and Hem Joshi. *Spectrochimica Acta Part B: Atomic Spectroscopy*, 66(6):444–450, 2011.

[78] Ajai Kumar, Sony George, R K Singh, Hem Joshi, and V P N Nampoori. *Laser and Particle Beams*, 29(2):241–247, 2011.

[79] H Iftikhar, Shazia Bashir, A Dawood, M Akram, A Hayat, K Mahmood, A Zaheer, S Amin, and F Murtaza. *Laser and Particle Beams*, 35(1):159–169, 2017.

[80] K S Singh, A Khare, and A K Sharma. *Laser and Particle Beams*, 35(2):352–361, 2017.

[81] Asadullah Dawood, Shazia Bashir, Naveed Ahmed Chishti, Muhammad Asad Khan, and Asma Hayat. *Laser and Particle Beams*, 36(2):261–275, 2018.

[82] PW Rambo and J Denavit. *Physics of Plasmas*, 1(12):4050–4060, 1994.

[83] J M Gomba, C D'Angelo, D Bertuccelli, and G Bertuccelli. *Spectrochimica Acta Part B: Atomic Spectroscopy*, 56(6):695–705, 2001.

[84] W Gekelman, M Van Zeeland, S Vincena, and P Pribyl. *Journal of Geophysical Research: Space Physics*, 108(A7), 2003.

[85] Yu Li, Changhong Hu, Hanzhuang Zhang, Zhankui Jiang, and Zhongshan Li. *Applied optics*, 48(4):B105–B110, 2009.

[86] L Dirnberger, PE Dyer, SR Farrar, and PH Key. *Applied Physics A*, 59(3):311–316, 1994.

[87] D K Bhadra. *The Physics of Fluids*, 11(1):234–239, 1968.

[88] S Amoruso, G Ausanio, A C Barone, R Bruzzese, L Gragnaniello, M Vitiello, and X Wang. *Journal of Physics B: Atomic, Molecular and Optical Physics*, 38(20):L329, 2005.

[89] R. Eason. *Pulsed Laser Deposition of Thin Films*. John Wiley & Sons, 2007.

[90] Ajai Kumar, R K Singh, Jinto Thomas, and S Sunil. *Journal of Applied Physics*, 106(4):043306, 2009.

[91] D. Bauerle. *Laser Processing and Chemistry, 3rd ed.* Springer, Berlin, 2000.

[92] R. Gijbels A. Vertes and F. Adams. *Laser Processing and Chemistry, 3rd ed.* Springer, Berlin, 2000.

[93] M. von Allen and A. Blatter. *Laser-Beam Interactions with Materials: Physical Principles and Applications*. Springer, Berlin, 1995.

[94] D. B. Chrisey and G. K. Hubler. *Pulsed Laser Deposition of Thin Films*. Wiley, New York, 1994.

[95] J. F. Ready. *Effect of High-Power Laser Radiation.* Acad. Press, Orlando, 1971.

[96] F J Mayer and Gar E Busch. *Journal of applied physics*, 57(3):827–829, 1985.

[97] Roger Kelly, Antonio Miotello, Bodil Braren, Arunava Gupta, and Kelly Casey. *Nuclear Instruments and Methods in Physics Research Section B: Beam Interactions with Materials and Atoms*, 65(1-4):187–199, 1992.

[98] A Huber, U Samm, B Schweer, and Ph Mertens. *Plasma physics and controlled fusion*, 47(3):409, 2005.

[99] S I Anisimov, D Bäuerle, and B S LukâĂŹYanchuk. *Physical Review B*, 48(16):12076, 1993.

[100] Shinobu Mukasa, Shinfuku Nomura, Hiromichi Toyota, Tsunehiro Maehara, Fumiaki Abe, and Ayato Kawashima. *Journal of Applied Physics*, 106(11):113302, 2009.

[101] Gabriele Cristoforetti, Alessandro De Giacomo, M Dell'Aglio, Stefano Legnaioli, Elisabetta Tognoni, Vincenzo Palleschi, and Nicolo Omenetto. *Spectrochimica Acta Part B: Atomic Spectroscopy*, 65(1):86–95, 2010.

[102] Antonio Miotello and Roger Kelly. *Applied Physics Letters*, 67(24):3535–3537, 1995.

[103] Ajai Kumar, R K Singh, V Prahlad, and H C Joshi. *Journal of Applied Physics*, 104(9):093302, 2008.

[104] S S Harilal, C V Bindhu, M S Tillack, F Najmabadi, and A C Gaeris. *Journal of Physics D: Applied Physics*, 35(22):2935, 2002.

[105] George Bekefi. Principles of laser plasmas. *New York, Wiley-Interscience, 1976. 712 p*, 1976.

[106] H. R. Griem. *Spectral Line Broadening in Plasmas.* Acad. Press, New York, 1974.

[107] J Gonzalo, F Vega, and Carmen N Afonso. *Journal of applied physics*, 77(12):6588–6593, 1995.

[108] S Amoruso, B Toftmann, Jørgen Schou, R Velotta, and X Wang. *Thin solid films*, 453:562–572, 2004.

[109] R K Singh, Ajai Kumar, B G Patel, and K P Subramanian. *Journal of applied physics*, 101(10):103301, 2007.

[110] W D Westwood. *Journal of Vacuum Science and Technology*, 15(1):1–9, 1978.

[111] O Yavas, E L Maddocks, M R Papantonakis, and R F Haglund Jr. *Applied physics letters*, 71(10):1287–1289, 1997.

[112] J Krishnaswamy, A Rengan, J Narayan, K Vedam, and CJ McHargue. *Applied Physics Letters*, 54(24):2455–2457, 1989.

[113] H C Joshi, V Prahlad, R K Singh, and Ajai Kumar. *Physics Letters A*, 373(37):3350–3353, 2009.

[114] P W Rambo and J Denavit. *Physics of Plasmas*, 1(12):4050–4060, 1994.

[115] G Cristoforetti, S Legnaioli, V Palleschi, A Salvetti, and E Tognoni. *Applied Physics B*, 80(4-5):559–568, 2005.

[116] C Sánchez-Aké, D Mustri-Trejo, T García-Fernández, and M Villagrán-Muniz. *Spectrochimica Acta Part B: Atomic Spectroscopy*, 65(5):401–408, 2010.

[117] A Tselev, A Gorbunov, and W Pompe. *Applied Physics A*, 69(3):353–358, 1999.

[118] R A Bosch, R L Berger, B H Failor, N D Delamater, G Charatis, and R L Kauffman. *Physics of Fluids B: Plasma Physics*, 4(4):979–988, 1992.

[119] O Rancu, P Renaudin, C Chenais-Popovics, H Kawagashi, J C Gauthier, M Dirksmöller, T Missalla, I Uschmann, E Förster, O Larroche, et al. *Physical review letters*, 75(21):3854, 1995.

[120] A S Wan, T W Barbee, R Cauble, P Celliers, L B Da Silva, J C Moreno, P W Rambo, G F Stone, J E Trebes, and F Weber. *Physical Review E*, 55(5):6293, 1997.

[121] A De Giacomo, M Dell'Aglio, A Santagata, and R Teghil. *Spectrochimica Acta Part B: Atomic Spectroscopy*, 60(7-8):935–947, 2005.

[122] Bhupesh Kumar, Dheerendra Yadav, and Raj K Thareja. *Journal of Applied Physics*, 110(7):074903, 2011.

[123] S S Harilal, C V Bindhu, V P Shevelko, and H J Kunze. *Laser and Particle Beams*, 19(1):99–103, 2001.

[124] Bhupesh Kumar, R K Singh, Sudip Sengupta, P K Kaw, and Ajai Kumar. *Physics of Plasmas*, 22(6):063505, 2015.

[125] Bhupesh Kumar, R K Singh, and Ajai Kumar. *Physics of Plasmas*, 23(4):043517, 2016.

[126] Shyam L Gupta, Pramod K Pandey, and Raj K Thareja. *Physics of Plasmas*, 20(1):013511, 2013.

[127] C Chenais-Popovics, P Renaudin, O Rancu, F Gilleron, J-C Gauthier, O Larroche, O Peyrusse, M Dirksmöller, P Sondhauss, T Missalla, et al. *Physics of Plasmas*, 4(1):190–208, 1997.

[128] Alamgir Mondal, R K Singh, and Ajai Kumar. *Physics of Plasmas*, 25(1):013517, 2018.

[129] A W Allen, M Blaha, W W Jones, A Sanchez, and Hans R Griem. *Physical Review A*, 11(2):477, 1975.

[130] V Narayanan, V Singh, Pramod K Pandey, Neeraj Shukla, and R K Thareja. *Journal of applied physics*, 101(7):073301, 2007.

[131] S I Anisimov, D Bäuerle, and B S LukâĂŹYanchuk. *Physical Review B*, 48(16):12076, 1993.

[132] Tatyana Sizyuk, John Oliver, and Prasoon K Diwakar. *Journal of Applied Physics*, 122(2):023303, 2017.

[133] P T Rumsby and J W M Paul. *Plasma physics*, 16(3):247, 1974.

[134] L Vriens and A H M Smeets. *Physical Review A*, 22(3):940, 1980.

[135] A Kramida, Yuri Ralchenko, Joseph Reader, and NIST ASD Team. Nist atomic spectra database (version 5.5.6). *National Institute of Standards and Technology, Gaithersburg, MD*, 2018.

[136] E G Zweibel and C Heiles. *Nature*, 385:131, 1997.

[137] Dongsu Ryu, Hyesung Kang, Jungyeon Cho, and Santabrata Das. *Science*, 320(5878):909–912, 2008.

[138] S Wu and X Lu. *Physics of Plasmas*, 21(2):023501, 2014.

[139] Sivanandan S Harilal, Mathew P Polek, and Ahmed Hassanein. *IEEE Transactions on Plasma Science*, 39(11):2780–2781, 2011.

[140] J Dardis and J T Costello. *Spectrochimica Acta Part B: Atomic Spectroscopy*, 65(8):627–635, 2010.

[141] Hiromichi Sato, Y Hirooka, K A Tanaka, and K Ishihara. *Journal of Plasma and Fusion Research SERIES (JPFR SERIES)*, 9:432–435, 2010.

[142] Shyam L Gupta, Pramod K Pandey, and Raj K Thareja. *Physics of Plasmas*, 20(1):013511, 2013.

[143] Ravi Pratap Singh, Shyam L Gupta, and R K Thareja. *Spectrochimica Acta Part B: Atomic Spectroscopy*, 88:54–62, 2013.

[144] G Cristoforetti, S Legnaioli, V Palleschi, A Salvetti, and E Tognoni. Characterization of a collinear double pulse laser-induced plasma at several ambient gas pressures by spectrally-and time-resolved imaging. *Applied Physics B*, 80(4-5):559–568, 2005.

[145] J Bohandy, B F Kim, and F J Adrian. Metal deposition from a supported metal film using an excimer laser. *Journal of Applied Physics*, 60(4):1538–1539, 1986.

[146] Bhupesh Kumar, R K Singh, Sudip Sengupta, P K Kaw, and Ajai Kumar. Propagation dynamics of laterally colliding plasma plumes in laser-blow-off of thin film. *Physics of Plasmas*, 21(8):083510, 2014.

[147] J M Fernández-Pradas, P Sopeña, S González-Torres, J Arrese, A Cirera, and P Serra. Laser-induced forward transfer for printed electronics applications. *Applied Physics A*, 124(2):214, 2018.

[148] Gabriel M Bilmes, Josué Vallejo, César Costa Vera, and Martin E Garcia. High efficiencies for laser cleaning of glassware irradiated from the back: application to glassware historical objects. *Applied Physics A*, 124(4):347, 2018.

[149] Linda Pabst, Frank Ullmann, Robby Ebert, and Horst Exner. Selective rear side ablation of thin nickel–chromium-alloy films using ultrashort laser pulses. *Applied Physics A*, 124(3):241, 2018.

[150] L Escobar-Alarcón, E Camps, E Haro-Poniatowski, M Villagran, and C Sanchez. Characterization of rear-and front-side laser ablation plasmas for thin-film deposition. *Applied surface science*, 197:192–196, 2002.

[151] Alamgir Mondal, R K Singh, and Ajai Kumar. Effect of ablation geometry on the dynamics, composition, and geometrical shape of thin film plasma. *Physics of Plasmas*, 25(1):013517, 2018.

[152] V Sivakumaran, H C Joshi, R K Singh, and Ajai Kumar. Optical time of flight studies of lithium plasma in double pulse laser ablation: Evidence of inverse bremsstrahlung absorption. *Physics of Plasmas*, 21(6):063110, 2014.

[153] H C Joshi, Ajai Kumar, R K Singh, and V Prahlad. Effect of a transverse magnetic field on the plume emission in laser-produced plasma: An atomic analysis. *Spectrochimica Acta Part B: Atomic Spectroscopy*, 65(5):415–419, 2010.

[154] Christoph M Ahamer and Johannes D Pedarnig. Femtosecond double pulse laser-induced breakdown spectroscopy: Investigation of the intensity enhancement. *Spectrochimica Acta Part B: Atomic Spectroscopy*, 2018.